

OBSERVATION OF THE TRANSVERSE STERN-GERLACH EFFECT IN NEUTRAL  
POTASSIUM AND AN ANALYSIS OF A CHARGED PARTICLE  
STERN-GERLACH EXPERIMENT

BY

ERIC ENGA

B.A.Sc., University of British Columbia, 1962  
M.A.Sc., University of British Columbia, 1966

A THESIS SUBMITTED IN PARTIAL FULFILMENT OF  
THE REQUIREMENTS FOR THE DEGREE OF  
DOCTOR OF PHILOSOPHY  
in the Department of  
PHYSICS

We accept this thesis as conforming to the  
required standard

THE UNIVERSITY OF BRITISH COLUMBIA

December, 1969

In presenting this thesis in partial fulfilment of the requirements for an advanced degree at the University of British Columbia, I agree that the Library shall make it freely available for reference and study. I further agree that permission for extensive copying of this thesis for scholarly purposes may be granted by the Head of my Department or by his representatives. It is understood that copying or publication of this thesis for financial gain shall not be allowed without my written permission.

Department of Physics

The University of British Columbia  
Vancouver 8, Canada

Date Dec 18/69

ABSTRACT

Two experiments are described. One is the successful observation of the resonant deflection of a beam of neutral potassium atoms at a frequency of 7.2 MHz, in agreement with the predictions of the theory of the Transverse Stern-Gerlach (TGS) experiment. The other is a proposal for a charged particle Stern-Gerlach experiment, which is based on an extension of the TSG experiment to time independent, inhomogeneous magnetic fields having the form

$$\vec{B}(\vec{r}, z) = B_0 \hat{k} + \vec{B}_1(\vec{r}) e^{i\omega z}$$

If the field  $\vec{B}_1(\vec{r})$  is well chosen, the charged particle trajectories are confined in a stable beam by the resulting Lorentz forces for motion generally along the z axis. This is, in fact, the principle of strong focusing which is now widely used in accelerator design. But in such a system it is also possible to satisfy the criterion for a TSG experiment, since in a frame of reference moving with a particle in the z direction, the field  $\vec{B}_1(\vec{r})$  is rotating in time.

TABLE OF CONTENTS

	Page
ABSTRACT .....	ii
LIST OF FIGURES .....	iv
ACKNOWLEDGEMENTS .....	vii
CHAPTER	
1 Introduction .....	1
2 Classical Theory of the Neutral Particle Transverse Stern-Gerlach Experiment .....	4
3 Experimental Procedure .....	14
4 Experimental Results .....	21
5 A Proposal for a Charged Particle TSG Experiment...	31
6 The Trajectories of an Ion with Zero Magnetic Moment in a DC Helical Quadrupole .....	44
7 The Trajectories of an Ion with Non-Zero Magnetic Moment in a DC Helical Quadrupole for Weak Lorentz Forces .....	53
8 The Influence of the Solenoid Field on the Trajectories, and the Stern-Gerlach Effect for Large Lorentz Forces in a DC Helical Quadrupole ...	67
9 Experimental Considerations .....	87
10 Concluding Remarks .....	97
BIBLIOGRAPHY .....	99
APPENDIX	
A The Helical Quadrupole Magnetic Field .....	101
B The Derivation of the Trajectories of an Ion in a Helical Quadrupole Field Consisting of Orthogonal Electric and Magnetic Fields Superimposed on a Homogeneous Field and on which an Additional Radial Force is Introduced .....	105
C An Ion Gun Design Suitable for Producing Small Diameter, Well Collimated Ion Beams .....	112

LIST OF FIGURES

Figure		Page
2-1	Schematic plot of a component of the Stern-Gerlach force versus time in the impulse approximation ....	6
2-2	Representation of the r-f field in the rotating co-ordinate system ( $\bar{x}$ , $\bar{y}$ , $\bar{z}$ ). It has been assumed that $\bar{B}_1(\bar{r})$ is in the x-y plane and makes an angle $-\phi$ with respect to the x-axis. $J_3$ is the component of $\bar{J}$ along the effective field <sup>3</sup> at $t = 0$ .....	6
2-3	Illustration of the orientation of $\bar{B}_1(\bar{r}) = G(x-iy)$ at a position $\bar{r} = x+iy$ .....	11
3-1	Schematic diagram of the overall system (not to scale) .....	15
3-2	Drawing of the deflection system with construction details omitted .....	18
3-3	Electrical circuit of the quadrupole wires showing details of the parallel resonant circuit used .....	19
4-1	(a) Plot of the percentage increase in beam intensity at the detector as a function of position in the x-y plane due to the focusing effect of the deflection system in a large, uniform-intensity beam .....	26
	(b) Contour map of the focused "pip", as constructed from Fig. 4-1a. The numbers on the contours are percentage increases in beam intensity due to the rotating quadrupole field (ordinate of Fig. 4-1a). The dotted lines are interpolated contours between widely separated points .....	27
4-2	Beam intensity profile for undeflected narrow beam.	28
4-3	Relative change of the beam intensity pattern for a narrow beam at resonance. The undeflected beam profile is shown in Figure 4-2 .....	29
4-4	Plot of the beam intensity near the beam center as a function of field $B_0$ for fixed frequency and different amplitude of the r-f field and its gradient .....	30
5-1	(a) A helical quadrupole wire system .....	33

Figure	Page
(b) A quadrupole wire system showing the electrodes necessary to produce an electric field orthogonal to the magnetic field .....	33
5-2 An iron core quadrupole, showing the electrodes necessary to produce an electric field orthogonal to the magnetic field .....	36
5-3 (a) Illustration of the frequency vectors in the rotating co-ordinate system $(\tilde{x}, \tilde{y}, \tilde{z})$ . $\vec{B}_1(\vec{r})$ is in the $\tilde{x}, \tilde{y}$ plane and makes an angle $-\phi_1$ with respect to the $\tilde{x}$ axis. $J_3$ is the component of $\vec{J}$ along the effective field .....	40
(b) An illustration of the vector $J_3 \sin \theta$ in the $(x, y, z)$ co-ordinate system at the time $t$ ...	40
7-1 A plot of trajectories from equation (7-6). The dotted trajectories are those obtained when the adiabatic condition is satisfied as the particle crosses the axis. The solid trajectories are those obtained when the sign of $J_3$ changes as the particle crosses the axis.....	63
7-2 Trajectories similar to those of Fig. 7-1 .....	63
7-3 Trajectories similar to those of Fig. 7-1 .....	64
7-4 Trajectories similar to those of Fig. 7-1 .....	65
7-5 An illustration of a system of stops which would give 100% polarization of the emerging beam .....	66
7-6 A somewhat simpler system to that illustrated in Fig. 7-5 which would give partial polarization of the inner beam .....	66
8-1 A chart of the regions where the roots $R_1'$ and $R_2'$ are real or complex. The light regions indicate that both are real, and the shaded regions indicate that one or both are complex.....	71
9-1 Illustration of the dimensions of a helical line and a helical strip .....	88
9-2 Illustration of the dimensions of a rectangular wire helical winding .....	88
9-3 Plot of minimum power versus wire radius for a rectangular copper wire helical winding at room temperature, from equation (9-11) .....	91

Figure		Page
A-1	Illustration of the orientation of the field $\vec{B}_0(\vec{r}) = -G(y+ix)$ at the point $\vec{r} = x+iy$ .....	102
A-2	Plot of the factor $C(q)$ defined by equation (a-8)..	104
C-1	Diagram of the ion gun described in appendix C.....	118
C-2	Typical performance of the ion gun described in appendix C. $V$ is the potential of the ionizing chamber .....	119

ACKNOWLEDGEMENT

It is a pleasure to acknowledge the very great assistance and enthusiasm of Professor Myer Bloom, who has guided this project to its present stage. Special thanks are due him for his help during the writing of this dissertation.

I sincerely thank Dr. Hin Lew, who contributed much of the design for the neutral particle experiment, and who was most helpful with advice on many experimental matters.

The experimental work received essential support from the Physics machine shop, especially from Doug Stonebridge.

I wish to thank Peter Flainek for his technical assistance, and the members of the Division of Pure Physics, National Research Council, for their help with the portion of the experiment which was performed there.

Special thanks are due my wife, Sylvia, for her support during this work.

This research was supported by grants from the National Research Council of Canada.

## CHAPTER 1

### Introduction

In the conventional Stern-Gerlach experiment a beam of atoms having magnetic moment  $\bar{\mu}$  is passed through a time-independent inhomogeneous magnetic field  $\bar{B}(\bar{r})$ . For simplicity, suppose that  $\bar{\mu} = \gamma\hbar\bar{J}$ , where  $\bar{J}\hbar$  is the angular momentum and  $\gamma$  is the gyromagnetic ratio, and that  $\bar{B}(\bar{r})$  consists of a large homogeneous part  $\bar{B}_0$  oriented along the  $z$  axis and an inhomogeneous part  $\bar{B}_1(\bar{r})$  with  $|\bar{B}_1(\bar{r})| \ll |\bar{B}_0|$ . The atoms acquire momentum while in the region of the inhomogeneous field because of the Stern-Gerlach force  $\bar{F} = (\bar{\mu} \cdot \nabla)\bar{B}(\bar{r})$ . Since  $\bar{J}$  precesses about the  $z$  axis at the Larmor frequency  $\omega_0 = -\gamma H_0$ , the only time-independent contribution to  $\bar{F}$  arises from  $J_z$ . Therefore, the net change in momentum for  $t \gg \omega_0^{-1}$  is proportional to  $J_z$ . One of the most important and best-known results in modern physics is that  $J_z$  is found experimentally to take on only the discrete values  $M = -J, -J + 1, \dots, +J$ . We can say that the Stern-Gerlach experiment provides us with a method for preparing a spin system in any one of the discrete quantum states  $M$ .

A few years ago it was shown theoretically (Bloom and Erdman 1962) that a more general form of the Stern-Gerlach experiment may be defined, using time-dependent inhomogeneous magnetic fields, i.e.

$$\bar{\mathbf{B}}(\bar{\mathbf{r}}, t) = \bar{\mathbf{B}}_0 + \bar{\mathbf{B}}_1(\bar{\mathbf{r}}) \cos \omega t \quad (1-1)$$

This generalized form of the Stern-Gerlach experiment was named the "Transverse Stern-Gerlach" experiment (TSG) because it was predicted that for  $\omega = \omega_0, 2J + 1$  deflected beams should also be observed, the quantum number  $M' = -J, -J + 1, \dots + J$  associated with each of these deflected beams in the TSG experiment being associated with  $J_z$ , the projection of  $\bar{\mathbf{J}}$  along the x axis of a coordinate system rotating with angular velocity  $\omega_0$  about the z axis. This arises from the fact that, if the oscillating inhomogeneous magnetic field at a given position is split into two rotating fields, one of them is synchronous with the precessing  $\bar{\mathbf{J}}$  vector at resonance. Thus, the cumulative changes in momentum are proportional to  $J_z$ .

In this thesis we describe two experiments. One is the successful observation of the resonant deflection of a beam of neutral potassium atoms at a frequency of 7.2 Mhz, in agreement with the predictions of the theory of the TSG experiment. The results of this experiment have already been published (Bloom, Enga, Lew 1967). The other is a proposal for a charged particle Stern-Gerlach experiment, which is based on an extension of the TSG experiment to time-independent, inhomogeneous fields have the form

$$\bar{\mathbf{B}}(\bar{\mathbf{r}}, z) = B_0 \hat{\mathbf{k}} + \bar{\mathbf{B}}_1(\bar{\mathbf{r}}) e^{i\omega z} \quad (1-2)$$

If the field  $\bar{\mathbf{B}}_1(\bar{\mathbf{r}})$  is well chosen, the charged particle trajectories

will be confined in a stable beam by the resulting Lorentz forces for motion generally along the  $z$  axis. This is, in fact, the principle of strong focusing which is now widely used in accelerator design. But in such a system it is also possible to satisfy the criterion for a TSG experiment, since in a frame of reference moving with the particle in the  $z$  direction, the field  $\vec{B}_1(\vec{r})$  is rotating in time. In analogy to the TSG experiment, it appears now to be possible to observe the  $2J + 1$  beams in such an experiment.

The classical theory of the neutral particle TSG experiment is presented in Chapter 2. The experimental procedure and the apparatus are described in Chapter 3, while the experimental measurements and their interpretation are given in Chapter 4.

We develop the extension of the TSG experiment to time independent, space varying fields in Chapter 5 and propose a Stern-Gerlach experiment for charged particles which is developed in Chapters 6 through 9. In Chapter 6 we consider the beam behavior for the Lorentz forces only. In Chapter 7 we introduce the Stern-Gerlach force in the limit that the Lorentz force is comparable to, or weaker than, the Stern-Gerlach force, and examine the beam trajectories. The case when the Lorentz force is larger than the Stern-Gerlach force is treated in Chapter 8. In Chapter 9 the experimental problems of this experiment are examined and the results of some preliminary experimental work developing a suitable ion beam are presented.

## CHAPTER 2

### Classical Theory of the Neutral Particle Transverse

#### Stern-Gerlach Experiment

A neutral atom of mass  $m$  and magnetic moment  $\bar{\mu}$  having initial position  $\bar{r}(0)$  and momentum  $\bar{p}(0)$  is assumed to interact with the magnetic field  $\bar{B}(\bar{r}, t)$  given by equation (1-1). The position and momentum of the atom at any time  $t$  are given by

$$\bar{r}(t) = \bar{r}(0) + \frac{1}{m} \int_0^t \bar{p}(t') dt' \quad (2-1)$$

$$\bar{p}(t) = \bar{p}(0) + \int_0^t \bar{F}(t') dt' \quad (2-2)$$

where the instantaneous Stern-Gerlach force  $\bar{F}(t)$  is given by

$$\bar{F}(t) = \gamma \bar{H} (\bar{J}(t) \cdot \bar{\nabla}) \bar{B}(\bar{r}(t), t) \quad (2-3)$$

while the time dependence of  $\bar{J}(t)$  is governed by the equations

$$d\bar{J}/dt = \gamma \bar{J} \times \bar{B}(\bar{r}(t), t) \quad (2-4)$$

Solution of equations (1-1), (2-1)-(2-4) gives  $\bar{r}(t)$ ,  $\bar{p}(t)$ , and  $\bar{J}(t)$  as a function of  $\bar{r}(0)$ ,  $\bar{p}(0)$ ,  $t$  and  $\bar{J}(0)$ . In many cases, if  $t$  is

made sufficiently large, there is a correlation between  $\vec{r}(t)$  and  $\vec{J}(t)$ , so that measurement of the intensity distribution in the beam enables one to draw conclusions about the allowed values of  $\vec{J}$ . It is difficult to solve equations (1-1), (2-1)-(2-4) for a general  $B(\vec{r},t)$ . The essential features of the Stern-Gerlach experiment can be found by using the "impulse approximation", which, in fact, is a very good approximation for the experimental arrangement used here and described in the next chapter.

Impulse Approximation  $\vec{r}(t)=\vec{r}(0)=\vec{r}=\text{constant}$  in the region  $B_1(\vec{r})\neq 0$

In this approximation the change in momentum  $\Delta\vec{p}$  due to the Stern-Gerlach force is calculated, assuming that the displacement of the atom in the region of the inhomogeneous field is negligible. This change in momentum can be measured by allowing the atoms to undergo free flight for a time  $\tau$  between the inhomogeneous field region and the detector, so that the displacement due to the Stern-Gerlach force is related to the momentum change by

$$\Delta\vec{r} = (\tau/m) \Delta\vec{p} \quad (2-5)$$

Now, if one calculates any component  $F_1(t)$  of the Stern-Gerlach force, using equations (1-1), (2-3) and (2-4) one obtains a plot such as that shown in Fig. 2-1 in which  $F_1(t)$  is made up of a constant term plus other terms which oscillate sinusoidally with time. For times that are long compared with the period of oscillation  $\tau_0$  of  $F_1(t)$ ,  $\Delta p_1(t)$  is proportional to the time-averaged value of  $F_1$ , which is the constant term, i.e.

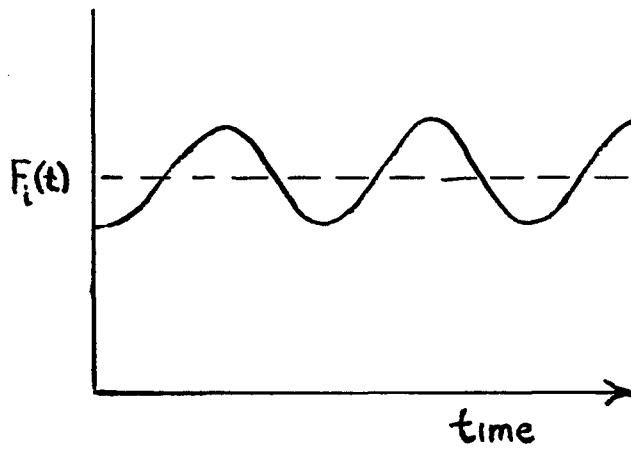


Figure 2-1. Schematic plot of a component of the Stern-Gerlach force versus time in the impulse approximation.

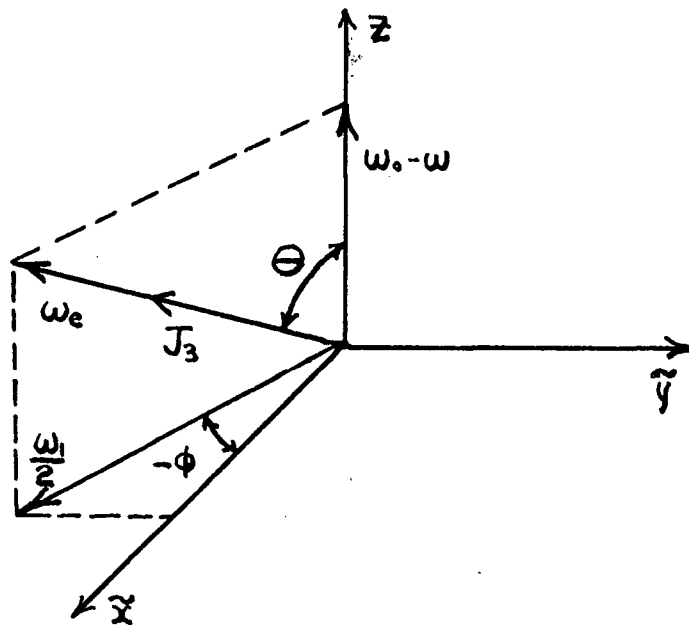


Figure 2-2. Representation of the rf field in the rotating coordinate system  $(\tilde{x}, \tilde{y}, z)$ . It has been assumed that  $\vec{B}_1(\vec{r})$  is in the  $x, y$  plane and makes an angle  $-\phi$  with respect to the  $x$ -axis.  $J_3$  is the component of  $\vec{J}$  along the effective field at  $t = 0$ .

$$(\Delta\bar{p}(t))_{t \gg \tau_0} \approx t \langle \bar{F}(t) \rangle \quad (2-6)$$

The component of  $\bar{J}$  which is quantized in each of the  $2J + 1$  deflected beams is found by examining the dependence of  $\langle \bar{F}(t) \rangle$  on  $\bar{J}$ . For the conventional Stern-Gerlach experiment,  $\omega = 0$  and it is obvious from equations (1-1), (2-3), and (2-4) that

$$(\Delta\bar{p}(t))_{t \gg \tau_0} \approx t \gamma \hbar J_z \frac{\partial \bar{B}_1(\bar{r})}{\partial z} \quad (2-7)$$

so that  $J_z$  is quantized. For  $\omega \neq 0$ , this is no longer true, as will be seen below.

We first write down equation (2-4) in the impulse approximation after making the transformation

$$J_{\pm} = J_x \pm iJ_y = \tilde{J}_{\pm} e^{\pm i\omega t} \quad (2-8)$$

$J_x$ ,  $J_y$ , and  $J_z$  are the components of  $\bar{J}$  in a coordinate system rotating with angular velocity  $\omega$  about the z axis.

$$d\tilde{J}_{\pm}/dt = \mp i(\Delta\omega\tilde{J}_{\pm} + 1/2\omega_{1\pm}J_z) \pm i(\omega_{1z} \cos \omega t \tilde{J}_{\pm} - 1/2\omega_{1\pm} e^{\pm 2i\omega t}) \quad (2-9)$$

$$dJ_z/dt = -1/4i(\tilde{J}_{+\omega_1} - \tilde{J}_{-\omega_1+}) - 1/4i(\tilde{J}_{+\omega_1-} e^{2i\omega t} - \tilde{J}_{-\omega_1+} e^{-2i\omega t}) \quad (2-10)$$

where

$$\Delta\omega = \omega - \omega_0, \quad \omega_0 = -\gamma B_0 \quad (2-11)$$

$$\omega_1 = -\gamma B_1(\vec{r}), \quad \omega_{1\pm} = \omega_{1x} \pm i\omega_{1y} \quad (2-12)$$

It is well known (Winter 1955) that the term involving  $\omega_{1z} \cos \omega t$  gives rise to resonance effects at  $\omega = \omega_0/2n$ , while the terms in  $\omega_{1\pm} e^{\pm 2i\omega t}$  give resonances at  $\omega_0/(2n+1)$ , where  $n$  is an integer. These multiple quantum effects are important when the inequality  $B_1 \ll B_0$  is not satisfied. As we shall demonstrate in Chapter 4, a large resonance is indeed observed in the TSG experiment near  $\omega = \omega_0/2$  for large values of  $B_1$ .

#### Replacement of the Linear Oscillating Field by a Rotating Field

We now assume that the value of  $B_1$  is sufficiently small that the influence of the terms which are explicitly time dependent in equations (2-9) and (2-10) is negligible, so that these terms may be dropped. This corresponds to assuming that  $B_{1z} = 0$  and to replacing the magnetic field  $\vec{B}_1(\vec{r}) \cos \omega t$  by  $(1/2)\vec{B}_1(\vec{r})e^{i\omega t}$ , i.e., one of amplitude  $(1/2)B_1(\vec{r})$  and rotating with angular velocity  $\omega$  about the  $z$  axis. Of course, a linear oscillating field is decomposed into two oppositely rotating fields, but only the one that rotates in the same sense as the spin precession is effective near resonance for small  $B_1$  (see, for example, Ramsey 1963, p. 146). It is well known that under these conditions the vector  $\vec{J} = (J_x, J_y, J_z)$  precesses about the effective field at an angular frequency

$$\omega_e = [(\Delta\omega)^2 + 1/4 \omega_1^2]^{1/2} \quad (2-13)$$

$\vec{\omega}_e$  is oriented at an angle  $\theta$  with respect to the z axis, as illustrated in Fig. 2-2 for an r-f. field oriented in the x-y plane in the laboratory frame at an angle  $-\phi$  with respect to the x axis at the position r. Representing this by a complex number,

$$\begin{aligned}\vec{B}_1(r) &= B_{1x}(\vec{r}) + iB_{1y}(\vec{r}) . \\ &= B_1(\vec{r})e^{-i\phi}\end{aligned}\tag{2-14}$$

the angle  $\theta$  is given by

$$\tan \theta = 1/2 \frac{\omega_1}{\omega_0 - \omega} = - \frac{\omega_1}{2\Delta\omega}\tag{2-15}$$

We specify the initial conditions for  $\vec{J}$  in terms of a coordinate system fixed in the rotating frame.  $J_3$  is the component of  $\vec{J}$  at  $t = 0$  along the effective field, which has polar angles  $(\theta, -\phi)$  as shown in Fig. 2-2.  $J_1$  and  $J_2$  are the components along the axes having polar angles  $(1/2\pi + \theta, -\phi)$  and  $(1/2\pi, 1/2\pi - \phi)$ , respectively. In terms of these initial conditions, the solutions to equations (2-8), (2-9), and (2-10) are as follows:

$$\begin{aligned}J_+(t) = J_-^*(t) &= \{1/2(1+\cos\theta)(J_1+iJ_2)\exp[i(\omega+\omega_e)t]+1/2(1-\cos\theta) \\ &(J_1-iJ_2)\exp[i(\omega-\omega_e)t]+J_3\sin\theta\exp(i\omega t)\} \exp(-i\phi),\end{aligned}\tag{2-16}$$

$$J_z(t) = -1/2\sin\theta[(J_1+iJ_2)\exp(i\omega_e t)+(J_1-iJ_2)\exp(-i\omega_e t)]+J_3\cos\theta\tag{2-17}$$

Using equations (2-3) and (1-1), the Stern-Gerlach force may be written

$$\bar{F}(t) = \gamma \hbar [J_x(t) \frac{\partial \bar{B}_1(\bar{r})}{\partial x} + J_y(t) \frac{\partial \bar{B}_1(\bar{r})}{\partial y} + J_z(t) \frac{\partial \bar{B}_1(\bar{r})}{\partial z}] \cos \omega t \quad (2-18)$$

### Special Case

In the experiment to be described in the next two chapters the oscillating field was produced by a four-wire system, as shown in Fig. 2-3. Near the center of symmetry of the four wires ( $r \ll R_0$ ), the field is well approximated by

$$\bar{B}_1(\bar{r}) = G(x-iy) = G\bar{r}^* \quad (2-19)$$

where  $G$  is the gradient of the field having dimensions gauss/cm and is given by

$$G = 0.8 \frac{I}{R_0^2} \quad (2-20)$$

where  $I$  is the current in each wire in amperes and  $R_0$  is the distance in centimeters from the center of symmetry to the center of each wire. The orientation of this field for a position  $\bar{r} = x+iy$  is shown in Fig. 2-3. Using eqs. (2-18) and (2-19), it is seen that

$$\bar{F}(t) = \gamma \hbar G J(t) \cos \omega t \quad (2-21)$$

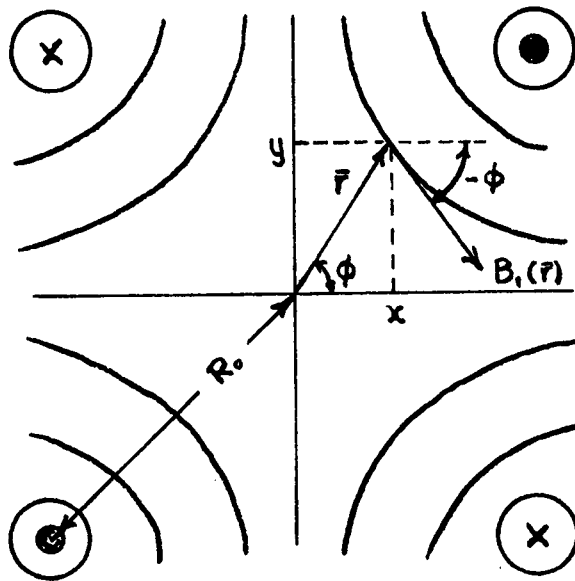


Figure 2-3. Illustration of the orientation of  $\vec{B}_1(\vec{r}) = G(x-iy)$  at a position  $\vec{r} = x+iy$ .

From equations (2-16) and (2-21), we see that  $\bar{F}(t)$  consists of terms which oscillate at frequencies  $\omega_e$ ,  $2\omega$ , and  $2\omega \pm \omega_e$ . In addition, there is one time-independent term which gives the time-averaged force to be

$$\langle \bar{F}(t) \rangle = 1/2 \gamma \hbar G J_3 \sin\theta e^{i\phi} \quad (2-22)$$

This expression contains the following information.

(a) The time-averaged force is proportional to the value of the component of  $\bar{J}$  along the effective field in the rotating frame. It is this component of  $\bar{J}$  which is quantized in the generalized Stern-Gerlach experiment on neutral atoms. It may be noted that this component of  $\bar{J}$  is independent of time in the inhomogeneous field region.

(b) The change of momentum  $\Delta\bar{p}$  is in the radial direction in the x-y plane. Since  $J_3$  is quantized, a circular beam is decomposed into  $2J + 1$  rings. The same effect is obtained for the conventional Stern-Gerlach experiment for this geometry (Beenewitz and Paul 1954).

(c) The dependence of  $\Delta\bar{p}$  on frequency is contained in the factor

$$\sin\theta = \frac{\omega_1}{2[(\Delta\omega)^2 + \omega_1^2/4]^{1/2}}$$

Therefore, when the rotating field approximation is valid, the change in momentum is maximum at the Larmor frequency and is an even function of  $\Delta\omega$ . It may be noted that the conventional Stern-Gerlach experiment for this geometry ( $B_0 = 0 = \omega$ ) is also described by the theory.

In addition, one can say from the argument presented in going from equation (2-21) to equation (2-22) that, in order to establish

quantization of  $\bar{J}$  along the effective field, the time spent by the atoms in the inhomogeneous field region must be much greater than the period of precession in the effective field, i.e.,  $t \gg \omega_1^{-1}$ .

Finally, the results given here may be compared with the quantum mechanical calculation of Bloom and Erdman (1962) for  $J = 1/2$ . A potassium atom having the average velocity in a typical beam experiment has a de Broglie wavelength much less than  $10^{-8}$  cm, while the collimation system used in this experiment (and other typical beam experiments) localizes the atoms to not less than  $5 \times 10^{-3}$  cm. Thus, quantum mechanics is only needed to describe the angular momentum properties of atoms. When the spin functions associated with different localized wave packets (in momentum space) in the quantum mechanical calculation (Bloom and Erdman 1962, equations (28)-(36)) are examined for arbitrary  $\omega$ , it is seen that they correspond to spins quantized along the effective field. For  $J = 1/2$ , there are only two such spin states. However, at the low fields at which the present experiment was done, the nuclear spin,  $I = 3/2$  is strongly coupled to the electron spin  $\bar{J}$  to form a total angular momentum  $F = 1, 2$ . In weak external fields, these split into eight Zeeman components with five distinct effective magnetic moments  $M_F g_J \mu_0 / 4$ ,  $M_F = 2, 1, 0, -1, -2$ , where  $\mu_0$  is the Bohr magneton and  $g_J$  is the Landé  $g$  factor of the  $^2S_{1/2}$  ground state of potassium.

## CHAPTER 3

### Experimental Procedure

The main aim of this experiment was to detect the predicted transverse Stern-Gerlach resonance and to check the theory of chapter 2. Since measurement of the resonance frequency to an accuracy of a few percent was sufficient for this purpose, it was possible to keep the design of the equipment relatively simple. A schematic diagram of the overall system is shown in Fig. 3-1.

A potassium beam was chosen since potassium atoms are easy both to produce and to detect. The beam was produced by heating potassium metal to 300°C in an iron oven, with a hole of diameter 0.005 cm to form the beam. This temperature corresponds to a vapor pressure for potassium of about 1 Torr. A single filling of the oven was sufficient to last for 60 hours of continuous operation. Micrometer adjustments were provided to position the oven in the plane transverse to the beam.

The collimation was done with a hole placed 31.4 cm from the oven. Any one of three different sized holes of diameter 0.17 cm, 0.0125 cm, 0.005 cm, respectively, could be brought into position by adjustment of a single micrometer.

The center of the deflection system, which was 10 cm in length, was placed 15.6 cm from the collimating hole, and the detector opening was 196 cm from the collimating hole. The long free-flight region of

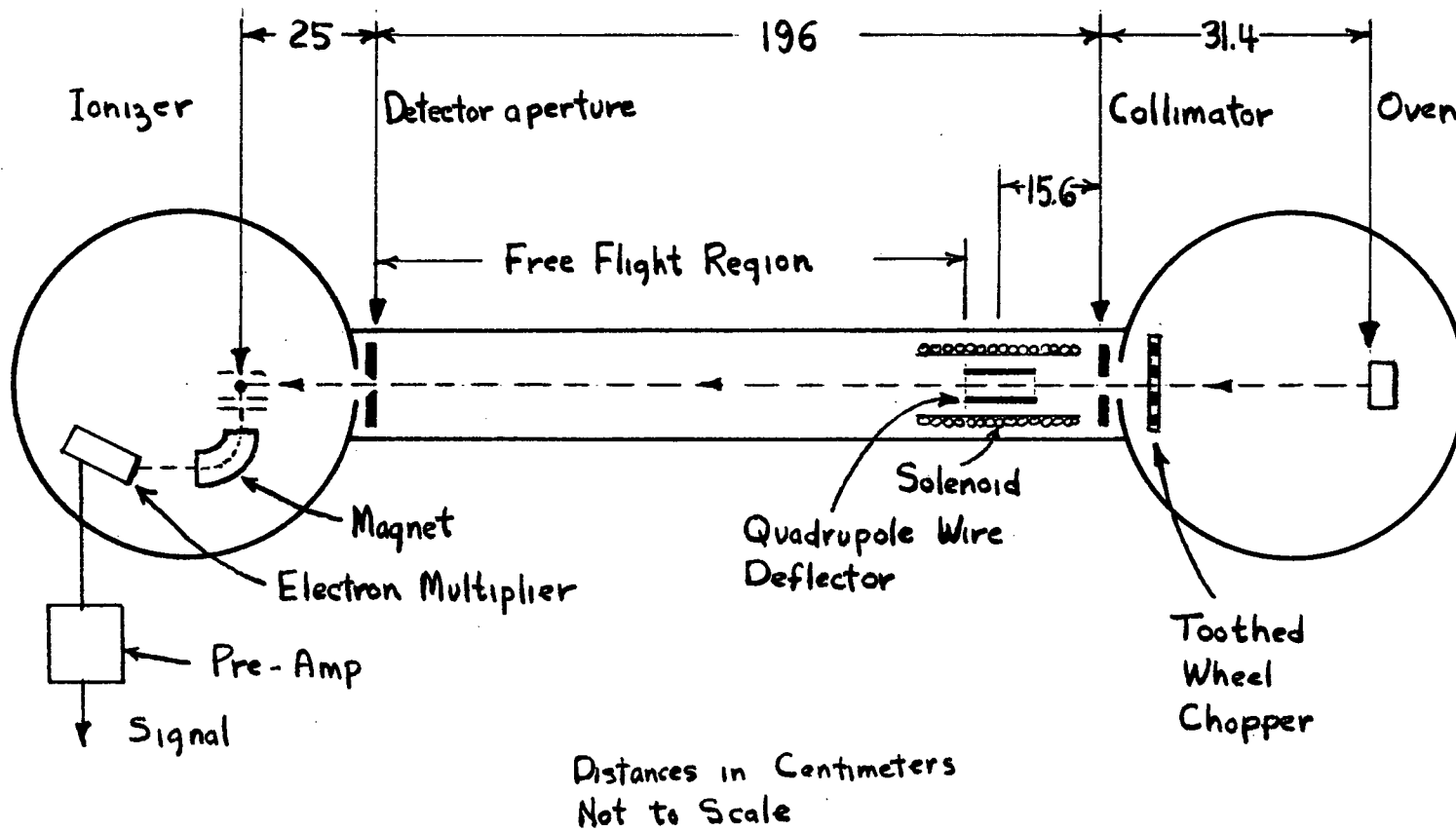


Figure 3-1. Schematic diagram of the overall system (not to scale).

about 180 cm which this provided had the advantage of increasing the size of the deflections and correspondingly reducing the tolerances necessary for the detector positioning and opening.

The detector was a tungsten hot-wire ionizer. The ions were collected on an electron multiplier after crude mass analysis. The mass spectrometer was really not necessary but was used because it was an integral part of the ionizer which was already on hand. The detector opening was rectangular and was formed by four knife-edged jaws which were each positioned by a micrometer. The hot wire was 0.018 cm in diameter and was placed 25 cm from the detector opening.

The beam was chopped at 30 c.p.s. with a toothed wheel driven by a synchronous motor. The output of the electron multiplier was amplified with a narrow-band 30 c.p.s. preamplifier, with a gain of 100, and then fed into a commercial lock-in amplifier (Princeton Applied Research Model JB4).

With the K oven at about 300°C a beam collimated with the 0.005 cm diameter hole gave a maximum output current of  $10^{-9}$  A from the electron multiplier. With an estimated gain of  $10^5$  for the multiplier, this meant that the incident K beam corresponded, after ionization, to an ion current of about  $10^{-14}$  A (neglecting losses in the mass spectrometer). Commercial tungsten wire, even the so-called undoped kind, contains large amounts of K impurity and an initial trial showed that the noise from the wire would swamp any expected resonance signal with observation time constants of a few seconds. Hence it was necessary to go to a potassium-free wire grown from  $W(CO)_6$ , according to the recipe described by Greene (1961). With such a wire and the maximum usable oven temperature of 300°C

we obtained a signal-to-noise ratio for the direct beam of 30 to 1 with a 3-second time constant on the lock-in amplifier.

The vacuum system was built partly of brass and partly of nonmagnetic stainless steel. Three oil diffusion pumps with liquid nitrogen cooled baffles were used, one in each of the two end chambers and one in the free-flight region. The three regions could be isolated from each other by valves. A pressure of  $3 \times 10^{-7}$  Torr was obtained, except in the oven region, where the pressure was  $8 \times 10^{-7}$  Torr.

The deflection system consisted of a solenoid and a quadrupole wire system, as illustrated in Fig. 3-2. Four push rods at each end of the solenoid allowed a three dimensional positioning of the entire assembly within the vacuum envelope.

The solenoid had overwound ends and gave a measured homogeneity of 1 part in 600 over the 10-cm center region.

The method used to match the very low resistance of the quadrupole wires to the nominal 50-ohm output of the r-f. source was to make the quadrupole wires part of a parallel resonant circuit, as shown in Fig. 3-3. The circuit used had an impedance of 120 ohms at a resonant frequency of 7.22 Mhz.

The maximum current used in the wires was 11.3 A (peak). This corresponds to a driving voltage across the circuit of 65 V r.m.s., and a total power dissipation of 35 W in the circuit. To absorb this heat, the wires were cemented with epoxy into accurately machined brass blocks, and the silvered mica capacitor was glued to a copper plate in thermal contact with the rest of the system. This assembly was all mounted in a water-cooled copper tube on which the solenoid was wound.

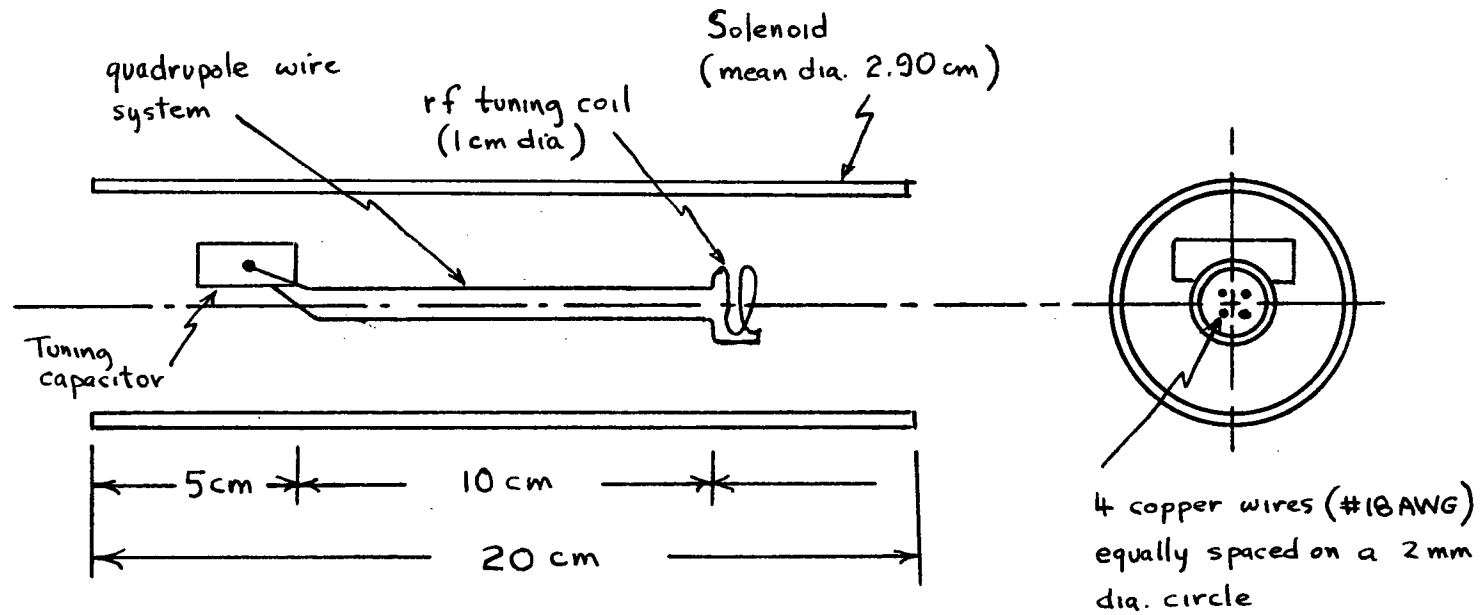


Figure 3-2. Drawing of the deflection system with construction details omitted.

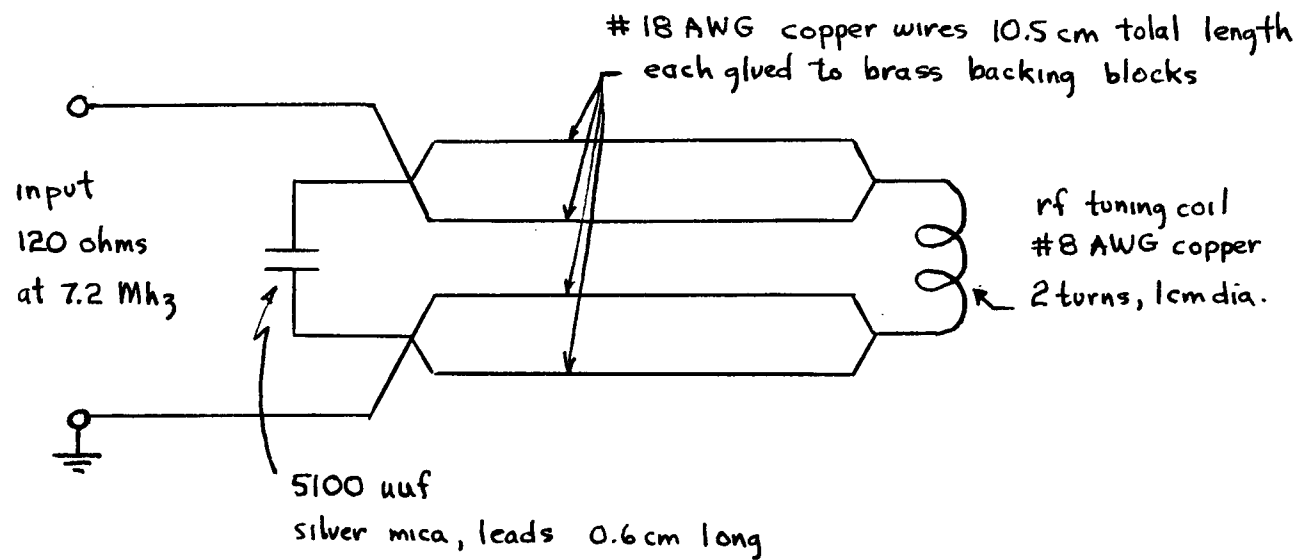


Figure 3-3. Electrical circuit of the quadrupole wires showing details of the parallel resonant circuit used.

The brass backing blocks produce image currents which act as a second quadrupole system with twice the relative spacing of the wires. These image currents reduce the field gradient due to the wires by about 25%. The maximum wire currents used (11.3 A (peak)) corresponded to a gradient of approximately 680 gauss/cm, as calculated by using equation (21), taking the image currents into account.

To facilitate the alignment of the quadrupole wires with respect to the beam, two holes 0.073 cm in diameter, one at each end of the solenoid, were fixed relatively accurately on the axis of the quadrupole system. These holes could then be located and the deflection system centered, using the beam intensity as the indicator.

A crystal controlled oscillator (Heathkit SB-400) driving a one-kilowatt linear amplifier (Heathkit SB-200) was used for the r-f. power source.

The deflection of an atom having initial velocity  $v$  parallel to the  $z$  axis is  $Cv^{-2}$ , where the constant  $C$  is obtained from equation (2-22) (at resonance, put  $\sin \theta = 1$ ) and equation (19.3) of Kusch and Hughes (1959). The average deflection is found by first showing that  $\langle v^{-2} \rangle = m/(2kT)$ , using the velocity distribution function of the beam. For our system  $T = 573^\circ\text{K}$ . For  $^{39}\text{K}$  in a small field  $B_0$ , it is appropriate to calculate the deflection of an atom in a spin state  $M_F = 1$ , since the statistical weights of the states  $M_F = 2, 1, 0, -1, -2$  are 1, 2, 2, 2, 1, respectively. In order to compare with experiment, we give here the result of 0.011 cm for the average deflection for a gradient of 430 gauss/cm.

## CHAPTER 4

### Experimental Results

The theoretical predictions which have been verified are contained in eq. (2-22). The significance of this equation is discussed immediately following it in Chapter 2.

To verify the existence of the radial force field, a large diameter beam collimated only by the 0.073-cm hole in the deflection system was produced. This beam was of essentially uniform intensity over a diameter of 0.3 cm at the detector. Since the expected most probable deflection was less than 0.03 cm, no large change would occur in the intensity profile except near the point corresponding to the origin of the radial force field. Here an increase in intensity should occur with a radius approximately equal to the average deflection, resulting in a sort of "pip" at the center of a uniform field. This is due to those atoms which are forced inwards and converge on the center area. This focusing effect is a consequence of any deflection system that produces a constant radial force field, and is identical, for example, with that obtained in a conventional quadrupole focusing experiment (Bennewitz and Paul 1954). This "pip" or focused spot was explored in considerable detail by moving the detector aperture, previously described, over the area of the pip. The aperture dimensions were set at 0.010 x 0.010 cm. The results are shown in Fig. 4-1a.

In Fig. 4-1a each curve represents a step-by-step scan of the beam

field in the vertical direction. The different curves correspond to different horizontal settings of the aperture. Each point on the curves was obtained by measuring the beam intensity first with the deflecting field off (strictly speaking, with the solenoid field off so that the quadrupole field was off resonance) and then with the deflecting field on. The percentage increase in intensity is plotted along the ordinate of the figure. From this family of curves a rough contour map of equal intensity lines may be constructed, as shown in Fig. 4-1b. Neglecting for the moment the secondary peaks in Figs. 4-1a and 4-1b, it may be noted, first, that the focusing effect is approximately cylindrically symmetric; secondly, that it occurs completely within a diameter of about 0.1 cm, with no other observable fluctuations within the 0.3-cm diameter circle, over which the whole beam extended; and thirdly, that the half width at half maximum of the focused spot for a gradient of 430 gauss/cm is about 0.025 cm, which is in agreement with the order of magnitude calculated in a previous section.

The center of the focused spot is assumed to be the position of the symmetry axis of the quadrupole wires in the plane of the detector.

The secondary peaks shown in Figs. 4-1a and 4-1b probably arise from some aberration in the focusing system. They almost certainly do not arise from any spatial resolution of the beam into its various components since the beam is broad compared to the deflecting power available.

The focusing effect was then studied on a very fine beam. With a collimator hole 0.005 cm in diameter, the undeflected beam profile is shown in Fig. 4-2.

The full width at half intensity is about 0.030 cm. The effect of turning on the quadrupole field is as shown in Fig. 4-3, the results having been obtained and plotted in exactly the same manner as those in Fig. 4-1a. One can see that the curves are roughly symmetrical about the vertical =  $-20 \times (0.001 \text{ cm})$  position and that there is a strong focusing action at vertical =  $-20 \times (0.001 \text{ cm})$  and horizontal =  $-15 \times (0.001 \text{ cm})$ . This position coincides with the center of the focused spot represented in Figs. 4-1a and 4-1b. In other words, it is the position of the symmetry axis of the quadrupole wires at the detector. Since the zeros of the axes in Fig. 4-3 correspond to the center of the undeflected beam, the quadrupole wires and the undeflected beam were aligned to about 0.02 cm in 180 cm (the free-flight length) or 1 part in  $10^4$ .

As shown in Fig. 4-3, there is a depletion of atoms at about 0.025 cm from the deflector axis (as measured in the plane of the detector). Farther out in the wings of the beam there is a positive change in intensity again, indicating that some atoms have been thrown outwards from the center of the beam. These are defocused atoms, i.e., atoms which, in the rotating frame, have effective magnetic moments in the x direction of opposite sign to those of the focused atoms. If that is so, then we have resolved the beam into two components. Apparently, our low deflecting power, coupled with the Maxwellian distribution of velocities in the beam, has precluded our observation of all five of the expected components. It should be pointed out that, because of the preliminary nature of the present experiment, no attempt has been made to achieve the ultimate in resolution or line shape.

Fig. 4-4 shows the field dependence of the resonance. The

detector position and opening were held fixed with respect to the beam, in a position that had a good signal-to-noise ratio. The strength of the quadrupole field  $B_1$ , at constant gradient, acting on the beam was varied by moving the deflection system and holding the beam fixed, in other words, by sending the beam down the deflection system at different distances from the zero axis. The field gradient was changed by changing the r-f. voltage drive across the system.

The curves were obtained by holding the frequency fixed at 7.22 Mhz and changing the solenoid field ( $B_0$ ) in discrete steps, and reading the output meter of the lock-in amplifier. The undeflected beam intensity was periodically checked to ensure that the system was not drifting.

These curves are in agreement with eq. (2-22). The resonance maximum occurs for  $B_0 = \omega_0/\gamma = 10.4$  gauss, the field for a Larmor precession frequency of 7.2 Mhz, and the line width for each curve, given by the plot of  $\sin\theta$  versus  $B_0$ , is approximately equal to  $B_1$ . No attempt has been made, however, to make a detailed theoretical fit of the observed line shape.

The double quantum resonance which appears in two of the curves of Fig. 4-4 is discussed theoretically in chapter 2. It occurs for large  $B_1$  (10 to 16 gauss) as predicted, but in this experiment a large  $B_1$  only occurs in the region of the quadrupole field where the higher-order terms of the expansion  $B_1 = G_1(xi - yj) + G_2(x^2 - y^2)i + \dots$  are becoming important. The effects of these higher-order terms have been neglected in the theory, as have been the components of  $B_1$  parallel to  $B_0$ , which occur near the ends of the wires.

The shift of the double quantum resonance towards lower fields which is apparent in the two curves is probably a Bloch-Siegert shift

(Ramsey 1963, p. 222), which results from the use of a linearly oscillating field  $B_1$  instead of a true rotating field.

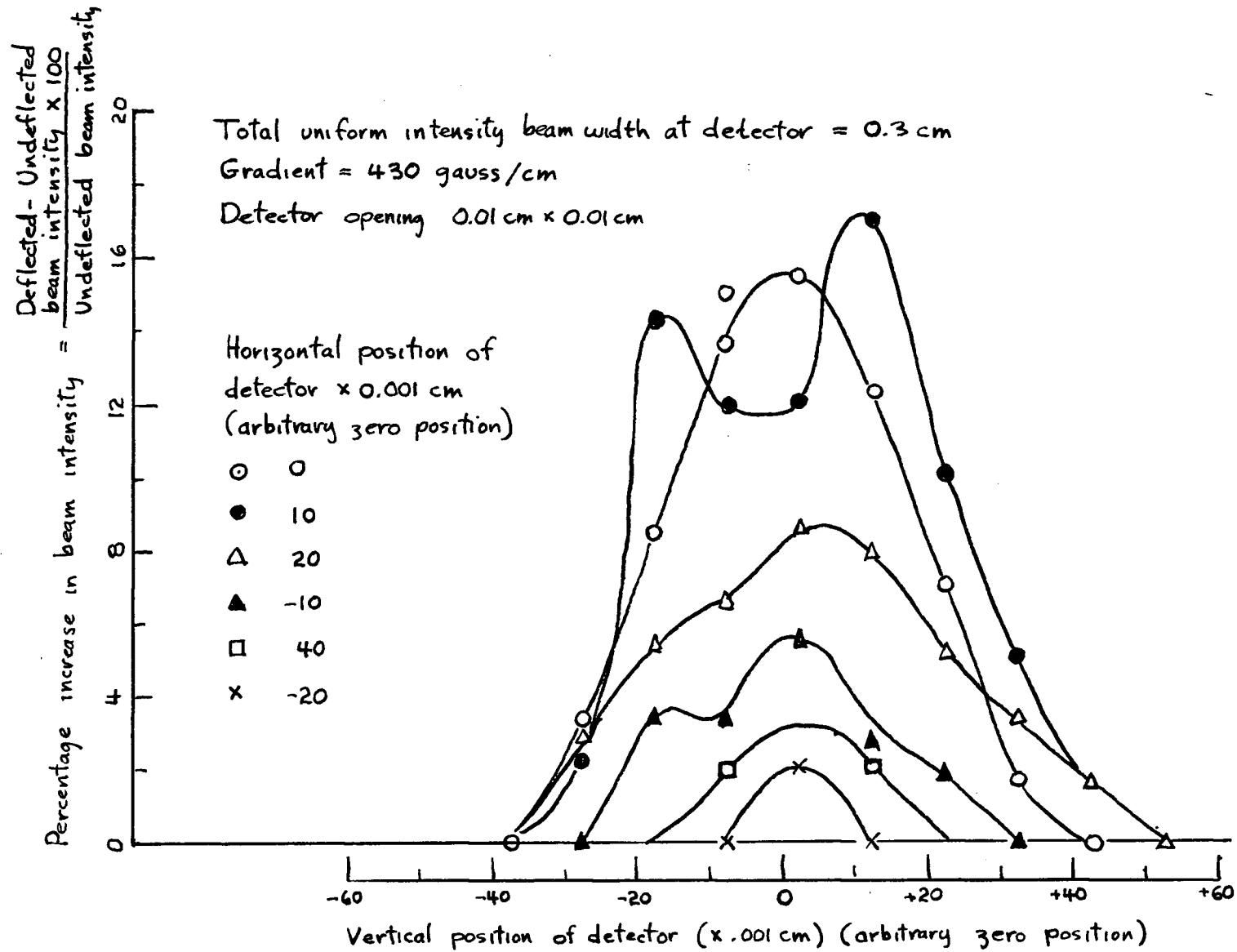


Figure 4-1a. Plot of the percentage increase in beam intensity at the detector as a function of position in the x,y plane due to the focusing effect of the deflection system in a large, uniform-intensity beam.

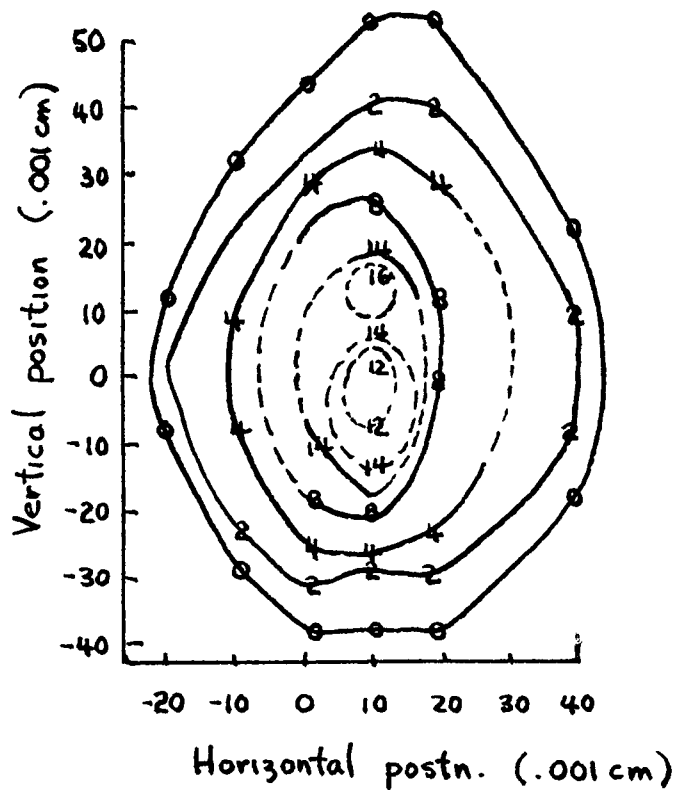


Figure 4-1b. Contour map of the focused "pip", as constructed from Fig. 4-1a. The numbers on the contours are percentage increases in beam intensity due to the rotating quadrupole field (ordinate of Fig. 4-1a). The dotted lines are interpolated contours between widely separated points.

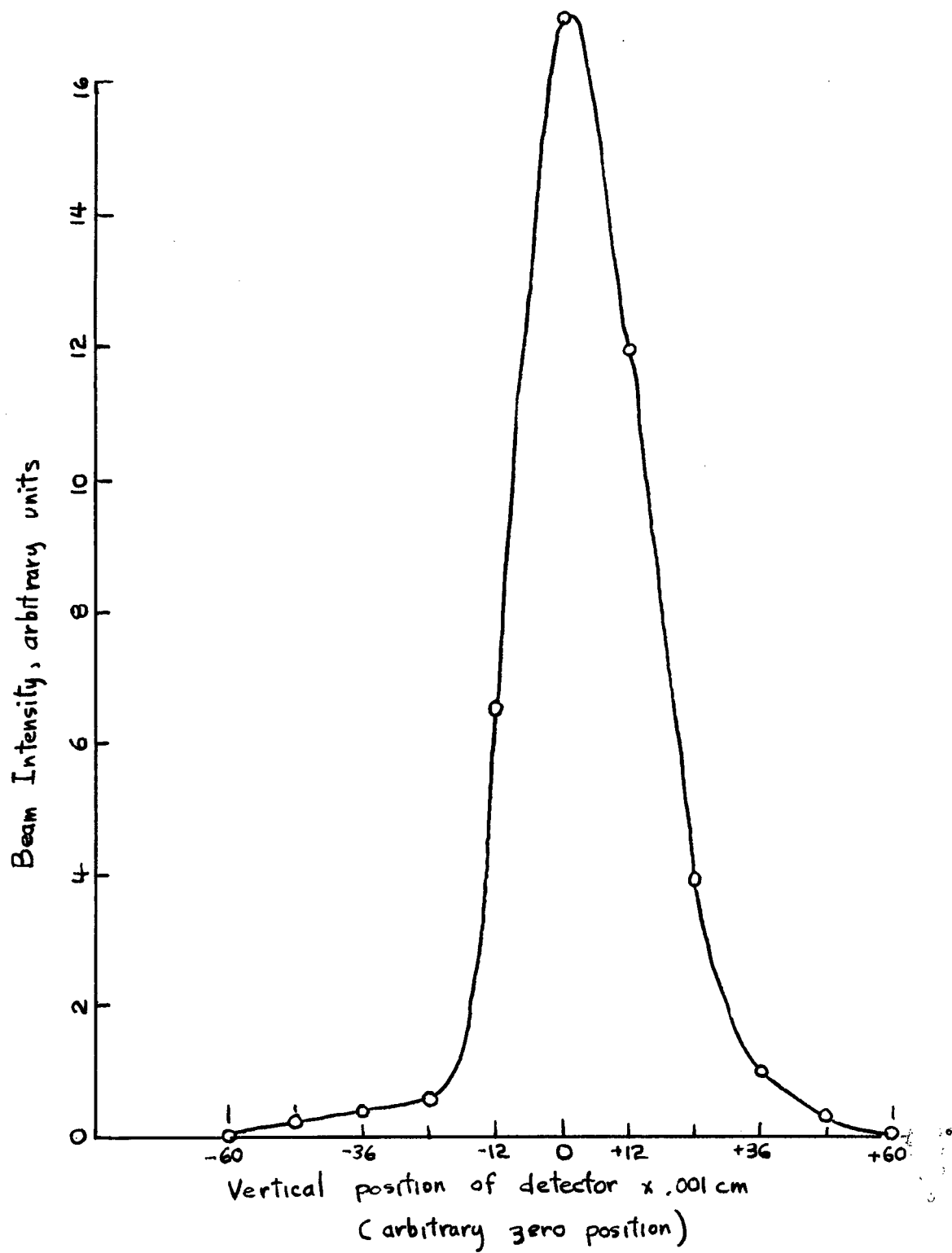


Figure 4-2. Beam intensity profile for undeflected narrow beam.

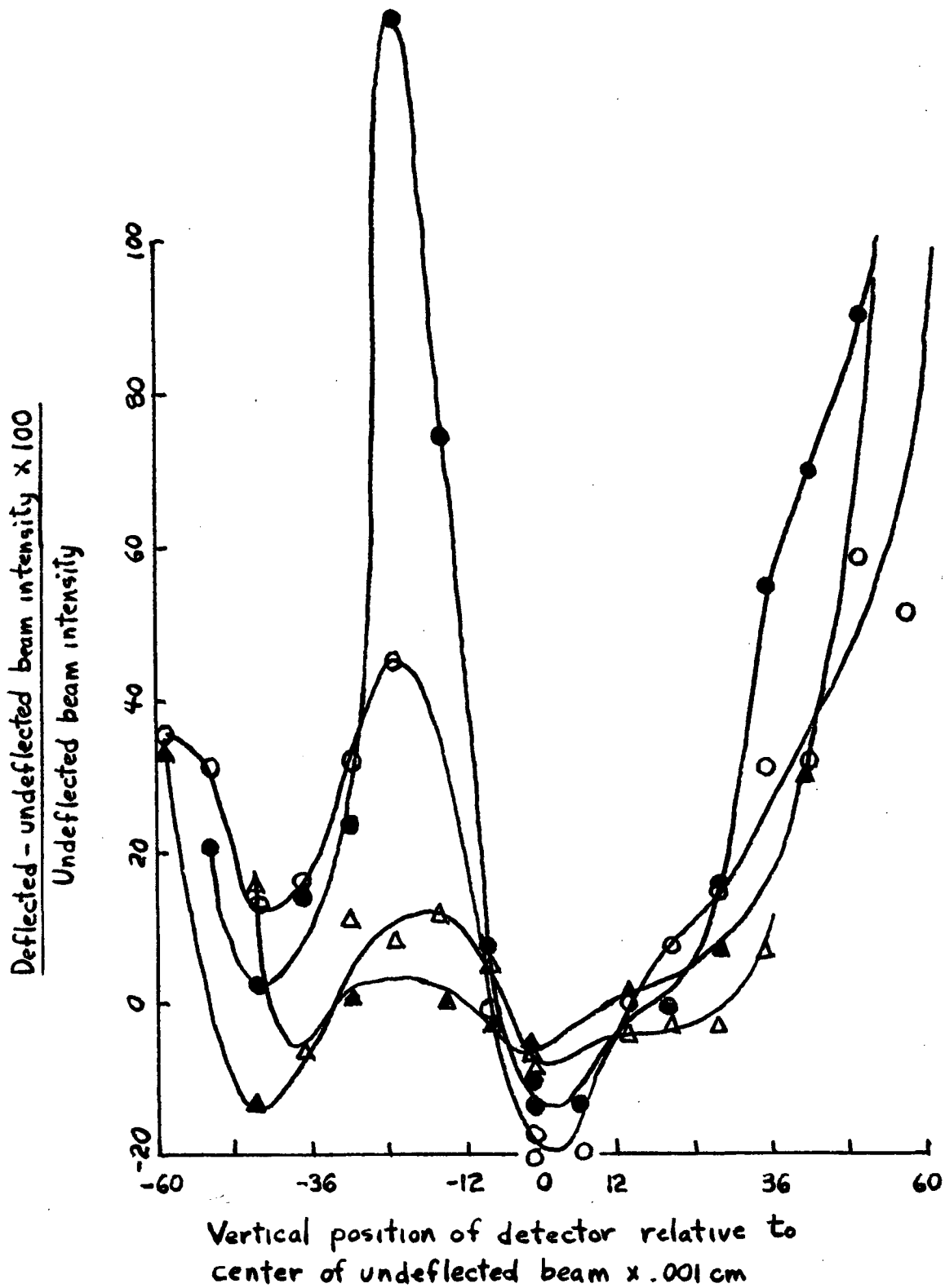


Figure 4-3. Relative change of the beam intensity pattern for a narrow beam at resonance. The undeflected beam profile is shown in Fig. 4-2.

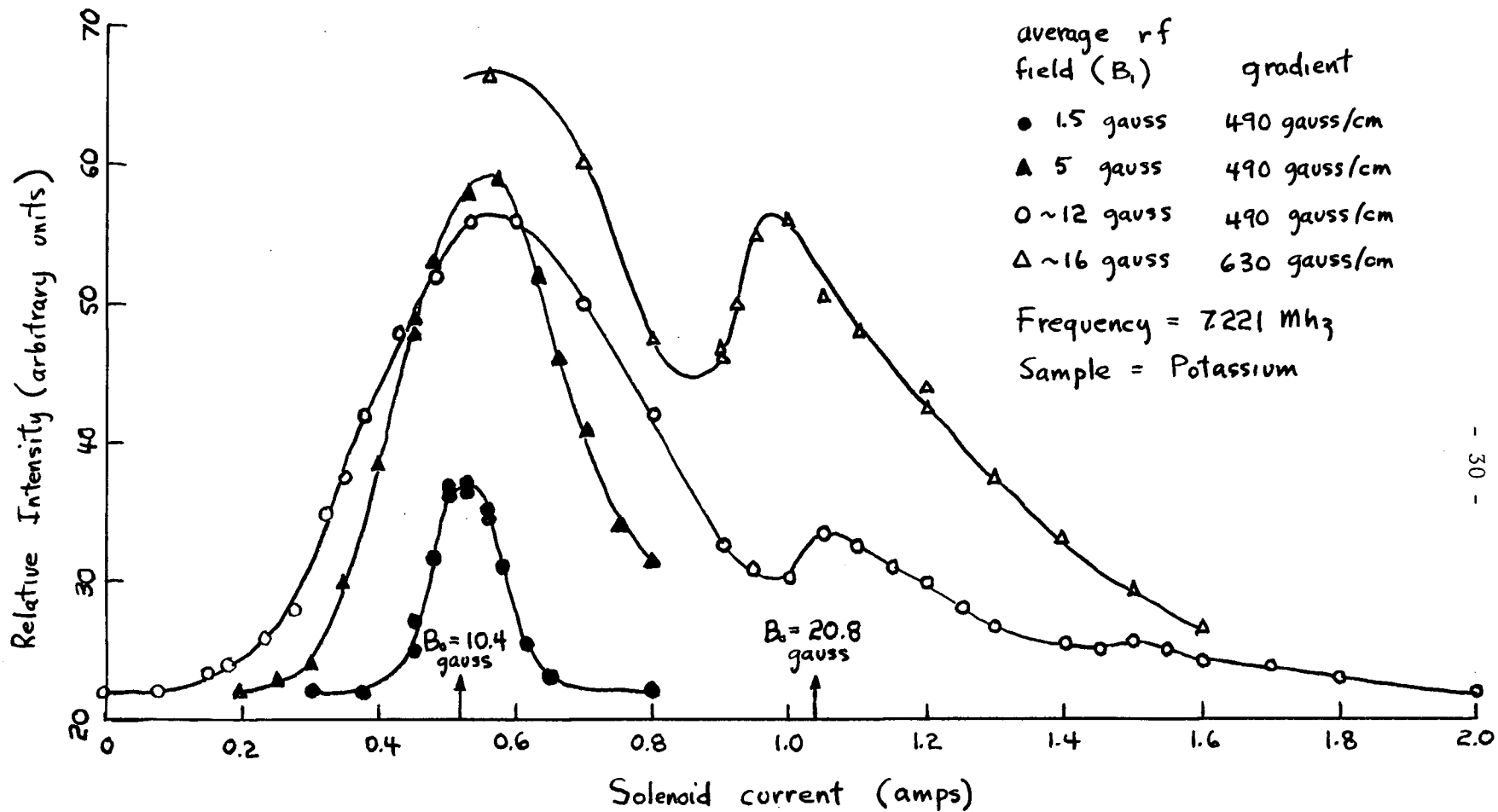


Figure 4-4. Plot of the beam intensity near the beam center as a function of the field  $B_0$  for fixed frequency and different amplitude of the rf field and its gradient.

## CHAPTER 5

### A Proposal for a Charged Particle TSG Experiment

The major obstacle to performing a conventional Stern-Gerlach experiment on charged particles is that the Lorentz force associated with a charged particle moving in a magnetic field is far larger than the Stern-Gerlach force. The spread of velocities inherent in any ionic beam would give rise to an uncertainty in the Lorentz force which would undoubtedly mask the effect of the Stern-Gerlach force.

When the neutral particle TSG experiment was proposed it seemed likely that it would be adaptable to charged particles, since it would be possible to send a charged particle beam parallel to the large homogeneous magnetic field and to observe resonant displacements in the plane perpendicular to this field due to an oscillating inhomogeneous magnetic field. Some of the difficulties associated with one special type of charged particle TSG experiment have already been discussed (Bloom and Erdman 1962; Rastall 1962; Byrne 1963).

In adapting the neutral particle TSG experiment to charged particles our preliminary thoughts were that in this geometry the amplitude of the ion beam oscillations produced by the oscillating Lorentz force would be inversely proportional to the frequency of the oscillating magnetic field, so that by using a high enough frequency these oscillations would not seriously impair the spatial resolution of the beam or the

Stern-Gerlach effect. In general terms these conclusions were correct, although at the time it was not realized that this system is one of a broad category of strong focusing systems.

Preliminary work was begun on the extension of the ac quadrupole system, which was used in the neutral particle TSG experiment, to charged particles. Much of the work at this stage went into producing an ion beam, but several prototype ac quadrupoles were also built. At the outset, it was realized that two major problems would have to be overcome to utilize the ac quadrupole for a TSG experiment with ionic beams. The first problem was to reduce the electric field produced by the voltage drop along the wires. This electric field was sufficiently strong, for the low energy beams which must be used, to produce very large oscillations in the beam. It was realized much later that this electric field could be utilized to good advantage to cancel the magnetic Lorentz force oscillations, but this did not eliminate the problem of reducing it without significantly reducing the oscillating magnetic field.

The second problem was to cool the quadrupole wires sufficiently well that very high field gradients could be produced.

Most of the work which went into the ac quadrupole was centered on these two problems; however, the auxiliary problems of generating high power RF (the designs were based on an RF power input of 4000 watts), grounding and shielding it, and matching the impedances, also took considerable time.

In the middle of this development it was realized that a much simpler system could be built using time independent currents in a helical quadrupole, such as is illustrated in Fig. 5-1a. This idea led

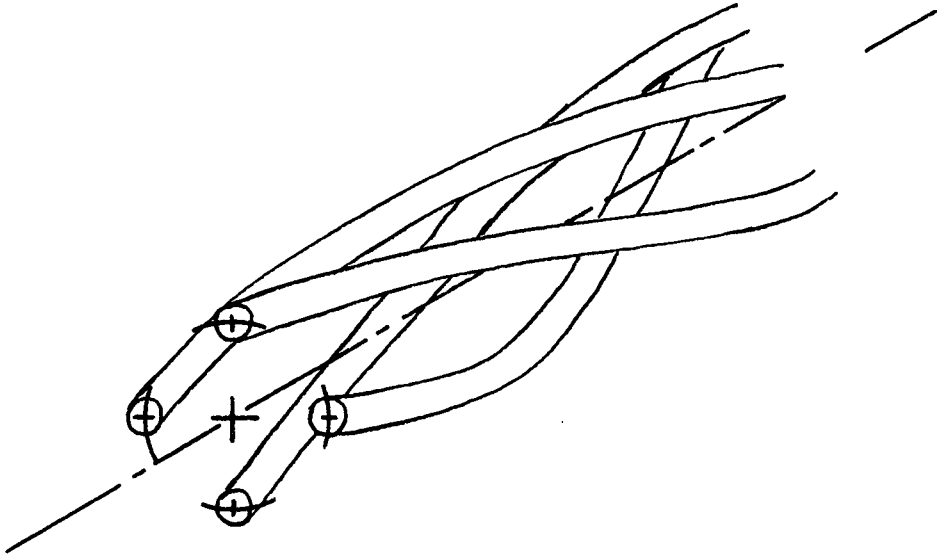


Figure 5-1a. A helical quadrupole wire system.

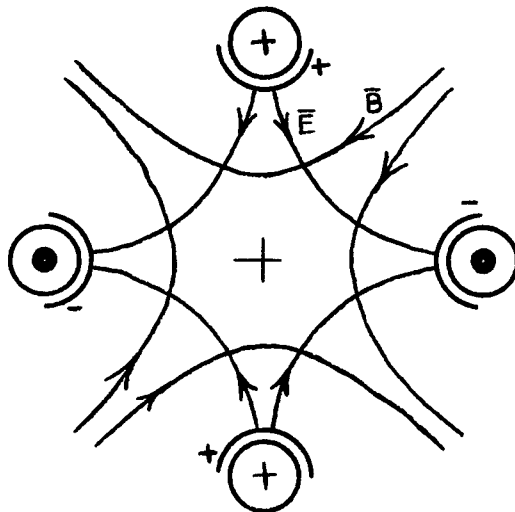


Figure 5-1b. A quadrupole wire system showing the electrodes necessary to produce an electric field orthogonal to the magnetic field.

to the extension of the TSG experiment to space varying fields as mentioned in Chapter 1, and finally we realized that we had been working all along within the general concept of strong focusing systems. Several months later we added an electric field orthogonal to the magnetic field in the quadrupole, as illustrated in Fig. 5-1b, which serves the important function of neutralizing the major portion of the Lorentz force, for a particular beam velocity.

When the dc helical quadrupole is used, rather than the ac quadrupole, the following important simplifications occur. There are no skin-depth or induced current phenomena, so that additional electrodes for control of the electric field may be inserted into the quadrupole without attenuating the magnetic field. Also, the full cross-section of the quadrupole wires carries the current so that the resistance and the power dissipated are both less than for the ac case. In fact, it should be appreciated that since the magnetic field gradient and resistance are each inversely proportional to the cross sectional area of the wires, and since the cooling capacity varies at least in proportion to the area, one can make this system as large as necessary without having the cooling capacity lag behind the power required to maintain a given field gradient. Finally, it is much easier to produce, shield and ground, and match impedances, for dc currents than high frequency ac currents.

So far, we have restricted this discussion to a helical quadrupole formed from current-carrying wires, since this is a form of construction which is simple and straight forward, and which has the important advantage that the additional electrodes which are inserted to produce the orthogonal electric field may be made concentric with the quadrupole

wires, as illustrated in Fig. 5-1b. Such a construction should give a very high degree of field orthogonality. However, a helical quadrupole field may also be produced using iron-cored magnets, as illustrated in Fig. 5-2. In this case the electrodes producing the orthogonal electric field must be placed between the iron poles, and the orthogonality achieved may not be very good. Finally, it is possible that super-conducting quadrupoles can be developed which would significantly increase the magnetic field gradients which can presently be attained.

In Chapter 2 we have given the classical theory of the transverse Stern-Gerlach experiment for a neutral particle. It is clear that the conclusions presented there regarding the Stern-Gerlach force may be carried over directly to the charged particle case, since it is not necessary to consider the Lorentz force unless one wishes to compute trajectories. That is, a neutral particle or a charged particle, if placed in the same field configuration, will experience the same Stern-Gerlach force.

In the following, we essentially repeat much of Chapter 2 for the particular case of a particle moving generally in the z direction in a time-independent helical quadrupole field.

The Stern-Gerlach force is given by:

$$\bar{F}_{SG} = (\bar{u} \cdot \bar{\nabla}) \bar{B}(\bar{r}, z) \quad (5-1)$$

or

$$F_{SGx} = (u_x \frac{\partial}{\partial x} + u_y \frac{\partial}{\partial y} + u_z \frac{\partial}{\partial z}) B_x \quad (5-2a)$$

$$F_{SGy} = (u_x \frac{\partial}{\partial x} + u_y \frac{\partial}{\partial y} + u_z \frac{\partial}{\partial z}) B_y \quad (5-2b)$$

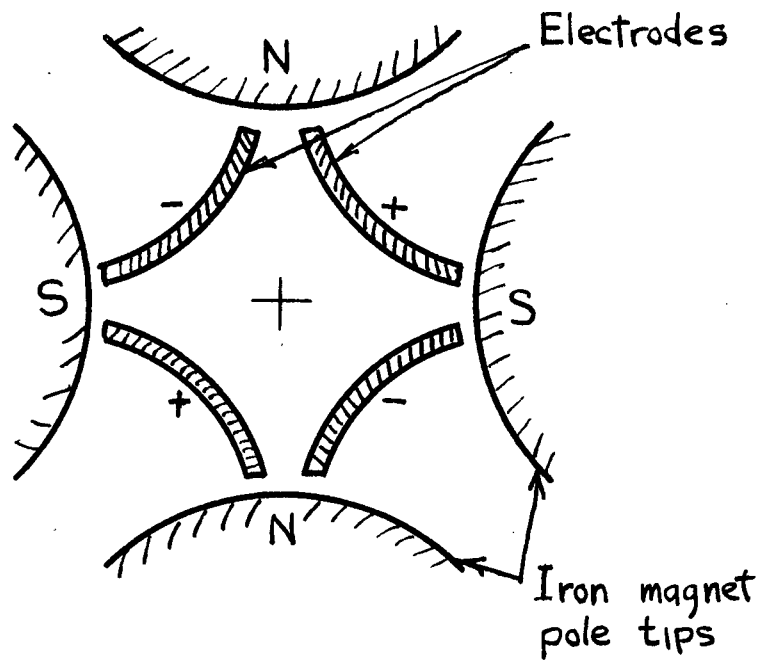


Figure 5-2. An iron core quadrupole, showing the electrodes necessary to produce an electric field orthogonal to the magnetic field.

$$F_{SGz} = (u_x \frac{\partial}{\partial x} + u_y \frac{\partial}{\partial y} + u_z \frac{\partial}{\partial z}) B_z \quad (5-2c)$$

In the helical quadrupole  $\bar{B}(\bar{r}, z)$  is given by:

$$\begin{aligned} \bar{B}(\bar{r}, z) &= B_x \hat{i} + B_y \hat{j} + B_o \hat{k} \\ B_x &= G_B (x \sin 2\underline{\omega}z - y \cos 2\underline{\omega}z) \\ B_y &= -G_B (y \sin 2\underline{\omega}z + x \cos 2\underline{\omega}z) \\ B_o &= \text{constant} \end{aligned} \quad (5-3)$$

Therefore, substituting equation (5-3) into (5-2) yields:

$$\begin{aligned} F_{SGx} &= G_B [u_x \sin 2\underline{\omega}z - u_y \cos 2\underline{\omega}z] \\ F_{SGy} &= -G_B [u_x \cos 2\underline{\omega}z + u_y \sin 2\underline{\omega}z] \\ F_{SGz} &= 0 \end{aligned} \quad (5-4)$$

If we rewrite equation (5-3) in the form:

$$\bar{B}(\bar{r}, z) = \bar{B}_1(\bar{r}) e^{i2\underline{\omega}z} + B_o \hat{k} \quad (5-5)$$

$$\bar{B}_1(\bar{r}) = G_B \bar{r} \quad (5-6)$$

then it is obvious that in a coordinate frame moving in the z direction at velocity  $v_0$ , the field  $\bar{B}(\bar{r}, z)$  will consist of a component  $\bar{B}_1(\bar{r})$  rotating with the angular velocity  $2\underline{\omega}v_0$ , and a solenoid field  $B_0$ .

We now define a coordinate frame  $\tilde{x}, \tilde{y}$  which is centered on the particle and which rotates in time at the angular frequency  $\omega$  about the z axis, such that the angular velocity of the component  $\bar{B}_1(\bar{r})$  about the z axis in the frame  $\tilde{x}, \tilde{y}$  is zero.

Since in general the particle may have an angular frequency  $\omega_L$  in time about the z axis (arising from the Lorentz forces, for example) we have the result that;

$$\omega = 2\underline{\omega}v_0 - \omega_L \quad (5-7)$$

where

$\omega_L$  = angular frequency in time of the particle about the z axis

In the coordinate frame  $\tilde{x}, \tilde{y}$ ,  $\bar{J}$  precesses about the effective field at an angular frequency

$$\omega_e = [(\Delta\omega)^2 + \omega_1^2]^{1/2} \quad (5-8)$$

where

$$\Delta\omega = \omega - \omega_0, \quad \omega_0 = -\gamma B_0 \quad (5-9)$$

$$\omega_1 = -\gamma B_1(\bar{r}) \quad (5-10)$$

The effective field is oriented at an angle  $\theta$  with respect to the z axis (as illustrated in Fig. 5-3a) where:

$$\tan \theta = - \frac{\omega_1}{\Delta\omega} \quad (5-11)$$

If, as in Chapter 2, we take  $J_z$  as the component of  $\vec{J}$  along the effective field at  $t = z = 0$ , and then calculate the time-average of the Stern-Gerlach force, it is clear that only the components of  $J_z$  will yield a cumulative force, since only  $J_z$  is synchronous with the field  $\vec{B}_1(\vec{r})$  (This is shown explicitly in Chapter 2).

Noting from Fig. 5-3b, that;

$$u_x = \gamma \hbar J_z \sin\theta \frac{B_x}{|B_1(\vec{r})|} + \text{terms oscillating at } \omega_e \quad (5-12a)$$

$$u_y = \gamma \hbar J_z \sin\theta \frac{B_y}{|B_1(\vec{r})|} + \text{terms oscillating at } \omega_e \quad (5-12b)$$

we can substitute equation (5-12) into (5-4) to yield, for times large compared to  $\frac{1}{\omega_e}$  :

$$\langle F_{SGx} \rangle = \gamma \hbar J_z \sin\theta |G_B| \frac{x}{r}$$

$$\langle F_{SGy} \rangle = \gamma \hbar J_z \sin\theta |G_B| \frac{y}{r}$$

This may be written

$$\langle \vec{F}_{SG} \rangle = \gamma \hbar J_z \sin\theta |G_B| \frac{\vec{r}}{r} \quad (5-13)$$

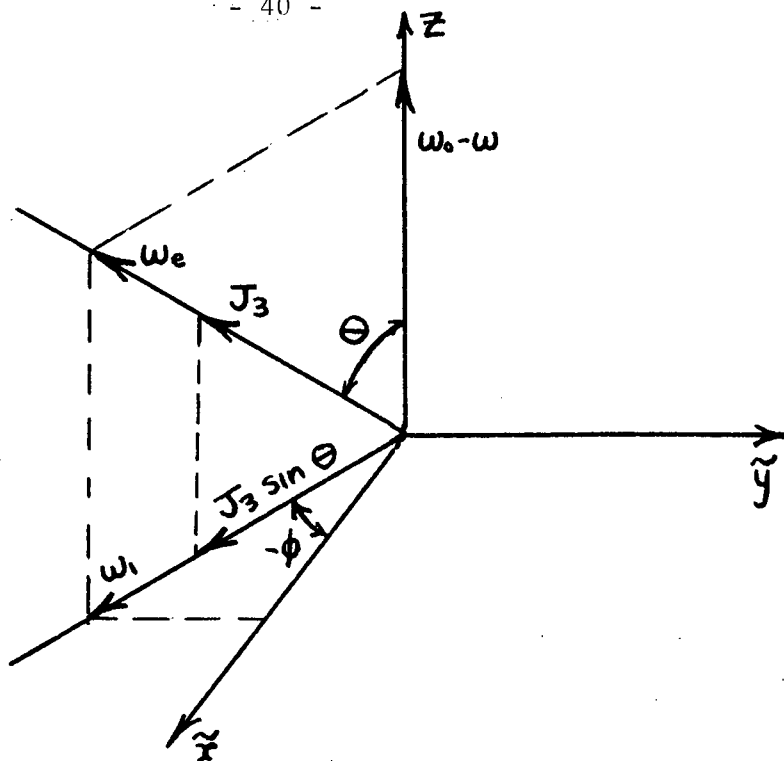


Figure 5-3a. Illustration of the frequency vectors in the rotating coordinate system  $(\tilde{x}, \tilde{y}, z)$ .  $\vec{B}_1(\tilde{r})$  is in the  $\tilde{x}, \tilde{y}$  plane and makes an angle  $-\phi$  with respect to the  $\tilde{x}$  axis.  $J_3$  is the component of  $\vec{J}$  along the effective field.

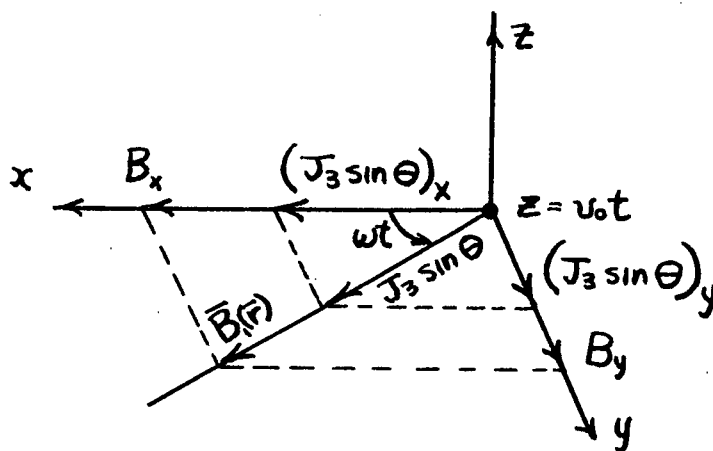


Figure 5-3b. An illustration of the vector  $J_3 \sin \theta$  in the  $(x, y, z)$  coordinate system at the time  $t$ .

with

$$\sin\theta = \frac{\omega_1}{[(\Delta\omega)^2 + \omega_1^2]^{1/2}} \quad (5-14)$$

Therefore the time averaged Stern-Gerlach force is radial, with a magnitude that depends on the  $\sin \theta$  factor noted above. This result is essentially the same as equation (2-22) in Chapter 2, except for a factor of 2 which enters because the linear oscillating field of the Chapter 2 system is decomposed into two rotating components which have 1/2 the magnitude of the original field.

We have discussed the detection of the neutral particle Transverse Stern-Gerlach effect in Chapters 3 and 4, and indicate in this Chapter that other detection techniques may be more suitable for the charged particle case. We can suggest four methods of detection as follows;

1) Resonant Deflection Method

The method used for the neutral particle case may also be used for charged particles. This method involves a resonance in the Stern-Gerlach force via the  $\sin \theta$  factor (see equation 5-14), and the detection of a consequent change in the intensity distribution of the beam. The resonance in the case of the helical quadrupole field could be produced by fixing  $v_0$ , thus fixing the apparent angular frequency of the helical quadrupole field in the rest frame of the particles, and then tuning the precession of the magnetic moment to this frequency using the longitudinal magnetic field  $B_0$ . As we shall see later, the width of the resonance is anticipated to be very large. The fact that the longitudinal field also produces a direct effect on the beam intensity distribution makes

the resonant deflection method much more difficult than for the neutral particle case.

## 2) Computational Method

The computational method involves a detailed comparison of the experimental beam intensity distribution as a function of the various experimental parameters with that computed from the equations of motion for the charged particles. It would be necessary to pick out those features of the intensity distribution which are associated with the small Stern-Gerlach force.

## 3) Comparison Method

In this method the intensity distribution of beams of similar ions having different magnetic moments would be compared and the effects characteristic of the Stern-Gerlach force exhibited. For example,  $^4\text{He}^+$  ions in the ground state would have two magnetic states corresponding to magnetic moments of approximately  $\pm\mu_e$ , where  $\mu_e$  is the magnetic moment of the electron. On the other hand,  $^3\text{He}^+$  would have 3 values for the projection of the magnetic moment along the external magnetic field in low magnetic fields because of the effect of the nucleus of spin 1/2. The magnetic moments of these states would be approximately  $\mu_e$ , 0, and  $-\mu_e$ , with probabilities, 1/4, 1/2, and 1/4, respectively.

## 4) The Rabi Magnetic Resonance Method

The Rabi method (Ramsey 1963) consists of sending the ions through a system composed of a "polarizer", a "depolarizer" and an "analyzer". The polarizer and analyzer for charged particle Stern-Gerlach experiments would be helical quadrupole systems which each produce a certain intensity distribution at the output given a certain distribution of intensities and

spins at the input. If the distribution of spins at each position in the beam were changed in the region between the polarizer and analyzer, the intensity distribution at the output of the analyzer would also be changed. Transitions between different spin states can be produced by a depolarizer in which the spins undergo magnetic resonance. For charged particles the depolarizer would consist of a longitudinal time independent field and a transverse rf. field, both of these magnetic fields being homogeneous. When the usual magnetic resonance conditions are satisfied, the probability of a particle undergoing a transition from one spin state to another in the depolarizer is large. When the beam passes from the polarizer through the depolarizer to the analyzer, it is necessary to satisfy conditions of "adiabatic passage" (Abragam, 1961) in order to preserve the direction of quantization of the spins when the magnetic resonance conditions in the depolarizer are not satisfied.

It would seem that of the four methods described above the Rabi method is the best one. This method differs from the other three in that a change in the intensity distribution of the beam is achieved by varying a parameter (the frequency of the rf. field in the depolarizer) which has no appreciable direct effect on the intensity distribution, but which effects the intensity only by changing the populations of the spin states.

## CHAPTER 6

### The Trajectories of an Ion with Zero Magnetic Moment in a DC Helical Quadrupole

In the following chapters we are attempting to find out whether a helical quadrupole system can be used to separate spin states in a Stern-Gerlach experiment. A basic theoretical requirement for such a study is the calculation of reasonably precise expressions for the particle trajectories. The direct approach, of finding the solutions to the equation of motion of an ion with a non-zero magnetic moment in a helical quadrupole system is complicated because the equation is non-linear. It has not, to our knowledge, been solved. We have, however, developed approximate, but useful solutions which are based on the characteristics of the average Stern-Gerlach force given by equation (5-13). In this chapter we are only considering the trajectories of ions with zero magnetic moment. For this case the equation of motion may be solved exactly in the axial region, and we have done this in appendix B.

In Chapter 7 we have developed solutions for a charged particle with non-zero magnetic moment which are valid in the limit that the Lorentz force is comparable to the Stern-Gerlach force. In this limit it is a valid approximation to decouple the radial motion from the

tangential motion. The radial equation of motion which results is linear and is solved in Chapter 7.

In Chapter 8 we have developed approximate solutions based on the similarity between the radial nature of the average Stern-Gerlach force given by equation (5-13) and a force of the form  $\Phi r$ , where  $\Phi$  is a constant. We show that the coefficient  $\Phi$  may be chosen to represent the cumulative effect of the Stern-Gerlach force over a range of  $z$  which must be specified. The substitution of the force  $\Phi r$  for the average Stern-Gerlach force reduces the equation of motion to a linear equation, and the solutions to this equation, evaluated at the end point of the arbitrary interval over which  $\Phi$  represents the cumulative effect of the Stern-Gerlach force, yields for each interval a point of the trajectory.

In the rest of this chapter we are only considering the motion caused by the Lorentz force with the solenoid field absent, since an understanding of this motion is very helpful before considering the additional effect of the Stern-Gerlach force. We show that this motion has a very simple character in the two extreme regions of operation. For very weak forces the motion is almost planar with a sinusoidal amplitude. For strong forces a magnitude of the Lorentz force is defined beyond which the motion is divergent. This may be called the point of instability, since the beam "blows up" quite rapidly beyond this point. At this point the trajectories are closely approximated by diverging spirals, with the radius growing linearly with distance along the optic axis, and the spiral pitch synchronous with the helical winding.

Between the two extremes, the trajectories are bounded and periodic

with four characteristic frequencies, which reduce to two in the helical frame of reference defined in appendix B. The motion is rather like a corkscrew twisted about the optic axis in this region.

In appendix B, we give the derivation of the equation of motion for a helical quadrupole which includes both magnetic and electric field gradients ( $G_B$  and  $G_E$ ) and a solenoid field ( $B_0$ ). As we have mentioned, a radial force term ( $\Phi$ ) is also included, but for the rest of this chapter we are considering only the case for  $\Phi = 0$ .

Except for the inclusion of  $\Phi$  and  $B_0$ , these equations are discussed quite extensively in the literature. G. Salardi et al. (1968) studied the device as a lens to collect and focus charged particles. K.J. Le Couteur (1967) studied particle guiding in helical multipole fields and the quadrupole in particular. He also considers the higher order terms which are important in the off-axial region, and shows that the device can be bent into a circle and still confine a beam. L.C. Teng (1959) studied the device in the axial region. A.M. Strashkevich et al. (1968) shows that at relativistic velocities it is possible to make the device somewhat achromatic by adding the equivalent of the term  $G_E$  described in appendix B. N.I. Trotsyuk (1969) shows that the device can be used to focus atoms and molecules under certain conditions.

Note that the electric and magnetic fields are orthogonal to one another, and as usual under this condition, the respective forces are colinear. For this reason the gradient terms appear in a single parameter

$\Theta$  :

$$\Theta = \frac{q}{mv_0} (G_E + v_0 G_B) \quad (6-1)$$

In most of the literature this point is not explicitly noted, since the concern is usually only with the magnetic field, because of its strong focusing properties for energetic particles. For our purposes this is an important point because by choosing  $G_E$  to cancel the term  $v_0 G_B$  we can make  $\Phi$  arbitrarily small without sacrificing the magnetic field gradient, which of course produces the Stern-Gerlach effect.

The solutions in appendix B are strictly valid only for small displacements from the optic (z) axis. Pearce (1969) has shown by numerical integration that for displacements less than  $L/20$ , where  $L$  is the helical step length, the equations are valid. When the displacements are greater than  $L/20$ , the axial magnetic field becomes appreciable, non-linear terms appear in the equations of motion, and the system becomes more strongly focusing.

If, in appendix B, we put  $B_0 = 0$ , the term  $W$  reduces to  $\omega$ , and if, in addition,  $\Phi = 0$ , we can write the trajectories, equations (b-22), as:

$$\begin{aligned} \underline{x} = & x_0 \cos \omega_2 z + \frac{\omega}{\omega_1} y_0 \sin \omega_1 z + \frac{\omega \dot{y}_0}{\Phi} [\cos \omega_2 z - \cos \omega_1 z] \\ & + \frac{\omega \dot{x}_0}{\Phi} \left[ \frac{\omega}{\omega_1} \sin \omega_1 z - \frac{\omega_2}{\omega} \sin \omega_2 z \right] \end{aligned} \quad (6-2a)$$

$$\begin{aligned} \underline{y} = & y_0 \cos \omega_1 z - \frac{\omega}{\omega_2} x_0 \sin \omega_2 z + \frac{\omega \dot{x}_0}{\Phi} [\cos \omega_1 z - \cos \omega_2 z] \\ & + \frac{\omega \dot{y}_0}{\Phi} \left[ \frac{\omega_1}{\omega} \sin \omega_1 z - \frac{\omega}{\omega_2} \sin \omega_2 z \right] \end{aligned} \quad (6-2b)$$

where

$$\underline{\omega}_1^2 = \underline{\omega}^2 + \Theta$$

$$\underline{\omega}_2^2 = \underline{\omega}^2 - \Theta$$

$$\underline{\omega} = \frac{2\pi}{L} \quad (6-2c)$$

If  $\Theta$  is small, we can rewrite these equations by expanding  $\underline{\omega}_1$  and  $\underline{\omega}_2$

$$\left. \begin{aligned} \underline{\omega}_1 &\approx \underline{\omega} + 1/2 \Theta/\underline{\omega} \\ \underline{\omega}_2 &\approx \underline{\omega} - 1/2 \Theta/\underline{\omega} \end{aligned} \right\} \Theta/\underline{\omega}^2 \ll 1 \quad (6-3)$$

Then applying simple trigonometric transformations, equation (6-2) takes the form:

$$\begin{aligned} \underline{x} = & x_0 \cos \underline{\omega}_2 z + y_0 \sin \underline{\omega}_1 z + \frac{2\underline{\omega} \dot{y}_0}{\Theta} \sin \underline{\omega} z \sin \frac{\Theta z}{2\underline{\omega}} \\ & + \frac{2\underline{\omega} \dot{x}_0}{\Theta} \cos \underline{\omega} z \sin \frac{\Theta z}{2\underline{\omega}} \end{aligned} \quad (6-4a)$$

$$\begin{aligned} \underline{y} = & y_0 \cos \underline{\omega} z - x_0 \sin \underline{\omega}_2 z - \frac{2\underline{\omega} \dot{x}_0}{\Theta} \sin \underline{\omega} z \sin \frac{\Theta z}{2\underline{\omega}} \\ & + \frac{2\underline{\omega} \dot{y}_0}{\Theta} \cos \underline{\omega} z \sin \frac{\Theta z}{2\underline{\omega}} \end{aligned} \quad (6-4b)$$

for  $\Theta/\underline{\omega}^2 \ll 1$

Transforming to the laboratory frame;

$$\begin{aligned} x &= \underline{x} \cos \underline{\omega} z - \underline{y} \sin \underline{\omega} z \\ y &= \underline{y} \cos \underline{\omega} z + \underline{x} \sin \underline{\omega} z \end{aligned} \quad (6-5)$$

$$x \approx x_0 \cos \frac{\Theta z}{2\underline{\omega}} + y_0 \sin \frac{\Theta z}{2\underline{\omega}} + \frac{2\underline{\omega} \dot{x}_0}{\Theta} \sin \frac{\Theta z}{2\underline{\omega}} \quad (6-6)$$

$$y \approx y_0 \cos \frac{\Theta z}{2\underline{\omega}} + x_0 \sin \frac{\Theta z}{2\underline{\omega}} + \frac{2\underline{\omega} \dot{y}_0}{\Theta} \sin \frac{\Theta z}{2\underline{\omega}}$$

If  $x_0, y_0$  are small, i.e.;

$$|r_0| \ll \left| \frac{2\underline{\omega} \dot{r}_0}{\Theta} \right| \quad (6-7)$$

where

$$|\dot{r}_0| = \sqrt{\dot{x}_0^2 + \dot{y}_0^2}$$

then this motion is nearly planar, and we can describe it by the radius  $r$ ; (Note 1)

$$r \approx \frac{2\underline{\omega} \dot{r}_0}{\Theta} \sin \frac{\Theta z}{2\underline{\omega}} + r_0 \quad (6-8)$$

Note that taking the limit as  $\Theta \rightarrow 0$  in equation (6-6), one gets simple free flight, as expected:

---

Note 1:  $r$  as used here is strictly a one dimensional coordinate rather than  $|\vec{r}|$ , since both positive and negative values are allowed.

$$\begin{aligned}x &= x_0 + \dot{x}_0 z \\y &= y_0 + \dot{y}_0 z\end{aligned}\tag{6-9}$$

We can make the following observations. The trajectories are bounded provided  $\Theta < \underline{\omega}^2$ . For very small  $\Theta$ , the motion is modified from simple free flight to a long wavelength sinusoidal motion, with a half period given by:

$$z_f = \frac{2\pi\omega}{\Theta}\tag{6-10}$$

As  $\Theta$  becomes larger, the motion becomes more complicated with two characteristic frequencies, or modes,  $\underline{\omega}_1$  and  $\underline{\omega}_2$ . In this region one must be careful about the relative importance of the axial ( $r_0 = 0$ ) and off-axial particles when making generalizations. Generally, when discussing the focusing properties of these systems, only the axial particles are considered. This involves the implicit assumption that:

$$|r_0| \ll \left| \frac{\omega \dot{r}_0}{\Theta} \right|\tag{6-11}$$

In many beam handling experiments this is a good assumption, but in this experiment we are considering beams with

$$\begin{aligned}r_0 &\approx 10^{-4} \text{ m} \\ \dot{r}_0 &\approx 10^{-3}\end{aligned}$$

From equation (6-11), this means that we are only justified in

generalizing to axial particles if

$$\frac{\omega}{\Theta} \gg 10^{-1} \text{ m} \quad (6-12)$$

We introduce the useful dimensionless parameter "a":

$$a = \frac{\Theta}{\omega^2} \quad (6-13)$$

Then the condition of equation (6-12) for a typical step length  $L = 2 \times 10^{-2}$  m, becomes;

$$a \ll \frac{10^{-1}}{3} \quad (6-14)$$

As will later be shown, this corresponds to a rather small value of  $\Theta$ .

Finally, we consider what happens when  $\Theta = \omega^2$ , i.e.,  $a = 1$ . Taking the limit in equation (6-2), as  $\Theta \rightarrow \omega^2$ , we get;

$$\begin{aligned} \underline{x} &= x_0 + y_0 \frac{\sin \sqrt{2} \omega z}{\sqrt{2}} + \dot{x}_0 \frac{\sin \sqrt{2} \omega z}{\sqrt{2} \omega} + \frac{\dot{y}_0}{\omega} [1 - \cos \sqrt{2} \omega z] \\ \underline{y} &= -\omega x_0 z + y_0 \cos \sqrt{2} \omega z + \frac{\dot{x}_0}{\omega} [\cos \sqrt{2} \omega z - 1] \\ &\quad + \dot{y}_0 \left[ \frac{\sqrt{2} \sin \sqrt{2} \omega z}{\omega} - z \right] \end{aligned} \quad (6-15)$$

for  $a = 1$

Comparing terms, we note that the dominant term becomes;

$$\begin{aligned}
 x &\approx 0 \left[ r_0 + \frac{\dot{r}_0}{\omega} \right] \\
 y &\approx -(\omega x_0 + \dot{y}_0)z + 0 \left[ r_0 + \frac{\dot{r}_0}{\omega} \right]
 \end{aligned}
 \tag{6-16}$$

for

$$|(\omega x_0 + \dot{y}_0)z| \gg 0 \left[ r_0 + \frac{\dot{r}_0}{\omega} \right]
 \tag{6-17}$$

For the values quoted earlier, i.e.

$$\begin{aligned}
 r_0 &\approx 10^{-4} \text{ m} \\
 \dot{r}_0 &\approx 10^{-3} \\
 L &\approx 2 \times 10^{-2} \text{ m}
 \end{aligned}
 \tag{6-18}$$

Condition (6-17) becomes

$$z \gg 3 \times 10^{-3} \text{ m}
 \tag{6-19}$$

Under these conditions it can be seen that the motion is very soon a simple spiral in the laboratory frame, with the spiral synchronous with the helix and the radius growing linearly with (z).

## CHAPTER 7

### The Trajectories of an Ion with Non-Zero Magnetic Moment in a DC Helical Quadrupole for Weak Lorentz Forces

In this chapter an approximate equation of motion is developed for the radial motion of an ion with non-zero magnetic moment in a dc helical quadrupole system which is valid when the Lorentz force is comparable to, or weaker than, the Stern-Gerlach force. In the limit that the Lorentz force is zero ( $\Theta \rightarrow 0$ ), the expressions yield the exact trajectories of a particle experiencing the average Stern-Gerlach force given by equation (5-13).

In order for  $\Theta$  to be small while maintaining a large Stern-Gerlach force, orthogonal magnetic and electric fields must be utilized as shown in Fig. 5-1b. In this way the Lorentz force;

$$F = q(\bar{E} + \bar{v} \times \bar{B})$$

can be made arbitrarily small for a particular velocity, while maintaining a large magnetic field gradient. From a practical point of view it is probably not desirable to reduce the Lorentz force much below a few percent of its value for the magnetic field alone, since this would require an extremely monochromatic beam and also a very high mechanical tolerance in the apparatus.

In Chapter 6 it was shown that the trajectories in a helical quadrupole in the absence of the Stern-Gerlach force are nearly planar for small  $\Theta$  and near axial particles. Under these conditions the radial dependence of the trajectories is given by equation (6-8);

(Note 1)

$$r \approx \frac{2\omega \dot{r}_0}{\Theta} \sin \frac{\Theta z}{2\omega} + r_0 \left\{ \begin{array}{l} |r_0| \ll \left| \frac{2\omega \dot{r}_0}{\Theta} \right| \\ \frac{\Theta}{\omega^2} \ll 1 \end{array} \right. \quad (7-1)$$

where

$$r(z=0) = r_0$$

$$\frac{dr}{dz}(z=0) = \dot{r}_0$$

This equation is the solution to the equation of motion;

$$F_H = m v_0^2 \frac{d^2 r}{dz^2} \quad (7-2)$$

where;

$$F_H = -m v_0^2 \left( \frac{\Theta}{2\omega} \right)^2 (r - r_0) \quad (7-3)$$

In the region in which equation (7-1) is valid, we can approximate the Lorentz force in the helical quadrupole by  $F_H$  (equation 7-3). If the average Stern-Gerlach force (equation 5-13) is added, a one dimensional equation of motion is obtained which yields the desired

---

Note 1:  $r$  as used here is strictly a one dimensional coordinate rather than  $|r|$ , since both positive and negative values are allowed.

radial dependence of the trajectories in this region:

$$\frac{d^2 r}{dz^2} + \left(\frac{\oplus}{2\omega}\right)^2 r = \ominus \frac{u_3 |G_B|}{2E} + \left(\frac{\oplus}{2\omega}\right)^2 r_0 \quad (7-4)$$

where

$$u_3 = \gamma \hbar J_3 \sin \theta, \text{ (Note 2)} \quad (7-5)$$

$$\ominus = 1(\text{sign } r), \text{ (Note 3)}$$

The solution to equation (7-4) is expressed in terms of the initial displacement  $r_0$  and the initial radial velocity  $\dot{r}_0$  as follows;

$$r = r_0 + \left(\frac{2\omega}{\oplus}\right)^2 \ominus \frac{u_3 |G_B|}{2E} \left[1 - \cos \frac{\oplus z}{2\omega}\right] + \frac{2\omega \dot{r}_0}{\oplus} \sin \frac{\oplus z}{2\omega} \quad (7-6)$$

It should be kept in mind that these solutions are valid approximations only for;

---

Note 2: In Chapter 5 we have shown that the Stern-Gerlach force will be radially inwards or outwards depending on the orientation of the magnetic moment with respect to the effective magnetic field in the system. The radial sense of this force will not change if the adiabatic condition is not violated. However, in this one dimensional formulation the adiabatic condition can be violated in the axial region since the effective field goes to zero as the particle crosses the axis. Thus, associated with  $J_3$  is a probability that it may change in this region if the adiabatic condition is violated.

Note 3: The factor  $\ominus$  must be inserted because in this one dimensional representation the sign of the Stern-Gerlach force depends on the sign of  $r$ .

$$|r_o| \ll \left| \frac{2\omega \dot{r}_o}{\Theta} \right|$$

(7-7)

$$\frac{\Theta}{\omega^2} \ll 1$$

Note that in the limit of  $\Theta \rightarrow 0$ , we obtain the exact trajectories for the average Stern-Gerlach force alone:

$$r = r_o + \dot{r}_o z + \frac{\Theta u_3 |G_B|}{4E} z^2; \quad \Theta = 0 \quad (7-8)$$

This would apply to a neutral particle in a magnetic helical quadrupole, or to a charged particle when the Lorentz force cancelation is complete for orthogonal electric and magnetic fields.

A focal length is defined by;

$$r(z_f) = r_o \quad (7-9)$$

From equation (7-6);

$$\tan \frac{\Theta z_f}{4\omega} = - \frac{E \dot{r}_o \Theta}{\omega u_3 |G_B|} \quad \left| r_o \right| \ll \left| \frac{2\omega \dot{r}_o}{\Theta} \right|$$

$$\frac{\Theta}{\omega} \ll 1 \quad (7-10)$$

Also note from equation (7-6) that all particles are refocused for:

$$\frac{\Theta z}{2\omega} = 2n\pi; \quad n = 1, 2, 3, \dots \quad (7-11)$$

Since this focal point is independent of  $u_3$ , no Stern-Gerlach effect

would be observed.

From equation (7-8) the focal length for  $\Theta = 0$  is;

$$z_f = - \frac{4Er_o}{u_3 |G_B|} ; \quad \Theta = 0 \quad (7-12)$$

This focal length is only defined for  $u_3 < 0$ . Differentiating equation (7-10) yields the change of focal length ( $\Delta z_f$ ) for a change in  $u_3$ ;

$$\Delta z_f = \left( \frac{4Er_o}{u_3 |G_B|} \right) \frac{\Delta u_3}{1 + \left( \frac{Er_o \Theta}{\omega u_3 |G_B|} \right)^2} \left\{ \begin{array}{l} |r_o| \ll \left| \frac{2\omega r_o}{\Theta} \right| \\ \frac{\Theta}{\omega} \ll 1 \end{array} \right. \quad (7-13)$$

Or, expanding about  $u_3 = 0$ ;

$$\Delta z_f = \frac{\omega^2 |G_B| \Delta u_3}{Er_o \Theta^2} \quad (7-14)$$

From equation (7-6) the maximum excursion,  $r_{max}$ , occurs for  $z = z_m$ , where;

$$z_m = \frac{2\omega}{\Theta} \tan^{-1} \left( - \frac{r_o E \Theta}{\omega u_3 |G_B|} \right) \left\{ \begin{array}{l} |r_o| \ll \left| \frac{2\omega r_o}{\Theta} \right| \\ \frac{\Theta}{\omega} \ll 1 \end{array} \right. \quad (7-15)$$

From equation (7-6), if  $u_3 = 0$  the focal length is;

$$z_{f_0} = \frac{2\pi\omega}{\Theta} \left\{ \begin{array}{l} u_3 = 0 \\ |r_o| \ll \left| \frac{2\omega r_o}{\Theta} \right| \\ \frac{\Theta}{\omega} \ll 1 \end{array} \right. \quad (7-16)$$

From equation (7-6), if  $u_3 = 0$  the focal length is;

$$z_{f_0} = \frac{2\pi\omega}{\oplus} \begin{cases} u_3 = 0 \\ |r_0| \ll \left| \frac{2\omega \dot{r}_0}{\oplus} \right| \\ \frac{\oplus}{\omega^2} \ll 1 \end{cases} \quad (7-16)$$

Then equation (7-14) can be written:

$$\frac{\Delta z_f}{z_{f_0}} = \frac{|G_B|L \Delta u_3}{E \dot{r}_0 a 4\pi^2} \quad (7-17)$$

Differentiating equation (7-6) yields the change in radius for a change in  $u_3$ :

$$\frac{\Delta r}{r(u_3=0)} = \frac{|G_B|L \Delta u_3}{2\pi a E \dot{r}_0} \tan \frac{\oplus z}{4\omega} \quad (7-18)$$

From equations (7-17) and (7-18) it can be seen that the relative effect on the trajectories for a change in  $u_3$  scales approximately as;

$$\frac{|G_B|L}{aE}$$

In Chapter 9 these parameters are discussed from the experimental point of view, considering such things as the power requirements and cooling capacities needed to produce a given value of  $G_B$ , and the energy range and collimation range in which a beam might be produced.

This justifies, to some extent, the values chosen for the trajectories in Fig. 7-1, but, of course, only a successful experiment is the final justification. Clearly, one desires large  $|G_B|L$ , but small  $aE$ .

Chromatic aberration is present in these systems. Both the parameters "E" and "a" change if the energy changes.

We have;

$$a = \frac{qL^2}{8\pi^2 E} \left( G_E + \sqrt{\frac{2E}{m}} G_B \right) \quad (7-19)$$

Differentiating, this becomes;

$$\frac{\Delta a}{a} = \frac{\Delta E}{E} \left[ \frac{qL^2}{16\pi^2 E} \sqrt{\frac{2E}{m}} \frac{G_B}{a} - 1 \right] \quad (7-20)$$

If the term in the brackets is zero, the chromatic effect of "a" vanishes. This is the condition for minimum chromatic aberration in the system.

It is useful to solve for the product  $L\sqrt{\frac{2E}{m}}$  from equation (7-20) with  $\frac{\Delta a}{a} = 0$ , in the following form;

$$L\sqrt{\frac{2E}{m}} = \frac{16\pi^2}{(L/a)(G_B/E)q} \quad (7-21)$$

This represents the condition for minimum chromatic aberration for given  $(L/a)$  and  $(G_B/E)$ .

Note that equation (7-6) may be written in terms of the ratios  $(L/a)$  and  $(|G_B|/E)$ , i.e.;

$$\mathbf{r} = \mathbf{r}_0 + (L/a)^2 \frac{u_3}{2\pi^2} (|G_B|/E) [1 - \cos(a/L)\pi z] + (L/a) \frac{\dot{\mathbf{r}}_0}{\pi} \sin(a/L)\pi z \quad (7-22)$$

Figures 7-1 to 7-4 are plots of the trajectories obtained from equation (7-6) for various values of  $(L/a)$  and  $(|G_B|/E)$ . Each figure shows six trajectories, obtained from the three initial conditions  $r_0 = 0$ ,  $\dot{r}_0 = 10^{-5}$ ,  $10^{-4}$ ,  $10^{-3}$ , and two values of the magnetic moment  $u_3 = +u_0$ , and  $-u_0$ .

The condition for minimum chromatic aberration (equation 7-21) is in order, for figures 7-1 to 7-4;

$$L \sqrt{\frac{2E}{m}} = 23.7; 15.8; 7.9; 1.6.$$

This will illustrate that it is very difficult to satisfy the condition for minimum chromatic aberration, especially if the product  $\left(\frac{LG_B}{aE}\right)$  is large, which is the case when the Stern-Gerlach effect is large. For example, in Fig. 7-1, if we make  $L = 2 \times 10^{-2}$  m, then a  $\text{He}^+$  beam would require an energy of about .02 eV to satisfy this condition. It is still harder to satisfy the condition for the other figures, although particles of larger mass than  $\text{He}^+$  would help.

As an example of the chromatic effect in these examples, consider Fig. 7-2. From equation (7-20) we obtain:

$$\frac{\Delta a}{a} \approx 11.5 \frac{\Delta E}{E} \quad (7-23)$$

In this case the dominant chromatic aberration occurs for the "a" terms.

For a  $\text{He}^+$  beam, "thermal" energies correspond to  $E \approx 7.4 \times 10^{-2}$  eV (300°C); for a 2 eV beam this gives;

$$\frac{\Delta E}{E} \sim 5\%$$

Putting this into equation (7-23) we have for the parameters used in Fig. 7-2;

$$\frac{\Delta a}{a} \sim 50\%$$

This points out the fact that the chromatic effects due to a thermal spread in the beam energy will cause large trajectory modifications. In this case they are as large as those caused by changing "a" by 50%.

Obviously, the chromatic effects must be carefully considered in a detailed design. Some velocity selection might prove useful, but it seems more likely that it would not be necessary in many cases since such a large Stern-Gerlach effect can be obtained.

Figures 7-5 and 7-6 illustrate a simple system of stops which could be placed at the exit of the Stern-Gerlach polarizer region to obtain beams polarized in either of the two senses shown schematically in the diagrams. Obviously, other systems of stops can be devised, depending on the degree of polarization which is required. The conditions depicted in Fig. 7-5, for example, which involve a hollow converging ion beam would give 100% polarization for both polarization senses, whereas removing the restriction of having a hollow beam produces 100% polarization for one sense of polarization but only partial polarization for the other.

An inherent advantage which these systems possess is that the ion beam is guided by the combined Lorentz and Stern-Gerlach forces at all

times. This means that perturbing forces which are bound to be present are not necessarily serious, since a small beam displacement from the optic axis will be compensated for by an additional focusing force. By extending the strong focusing Lorentz force beyond the polarizing region on both ends one can also pre-focus and post-focus the beam. If velocity selection was required this could be accomplished in a section of the helical quadrupole prior to the polarizing region by using the velocity dependence of the focal points.

In Chapter 9 the experimental problems of achieving a high magnetic field gradient  $G_B$ , and a low beam energy  $E$ , are considered. From Fig. 9-3, if we assume  $E = 2$  eV, it seems very easy to produce a value  $G_B/E = 500$  gauss/cm/eV for apertures of a few mm and step length  $L = 2$  cm. It is much harder to produce  $G_B/E = 5000$  gauss/cm/eV, but it should be possible if the aperture is as small as possible and a long step length is used. Pulsed operation is very sensible for producing high field gradients since it lessens the fundamental restriction imposed by the limited cooling capacity of the system. Any value of  $L/a$  may be produced within the range of "a" ( $0 < a < 1$ ). Of course, it is necessary to have very good orthogonality between the electric and magnetic fields if very small values of "a" are used.

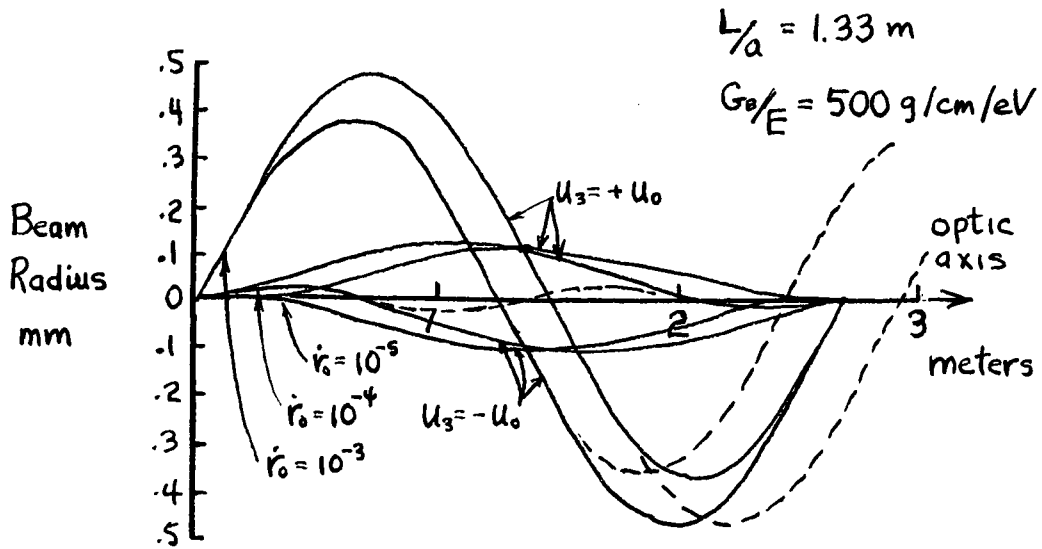


Figure 7-1. A plot of trajectories from equation (7-6). The dotted trajectories are those obtained when the adiabatic condition is satisfied as the particle crosses the axis. The solid trajectories are those obtained when the sign of  $J_3$  changes as the particle crosses the axis.

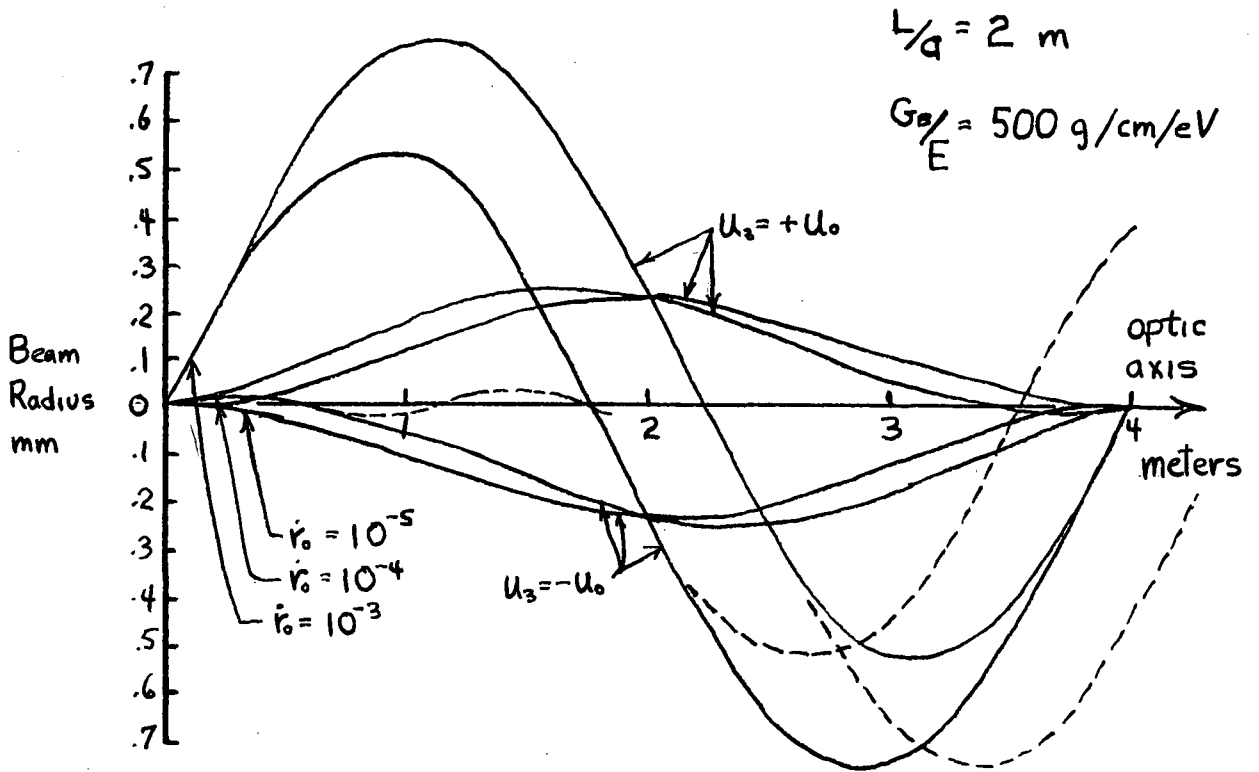


Figure 7-2. Trajectories similar to those of Fig. 7-1.

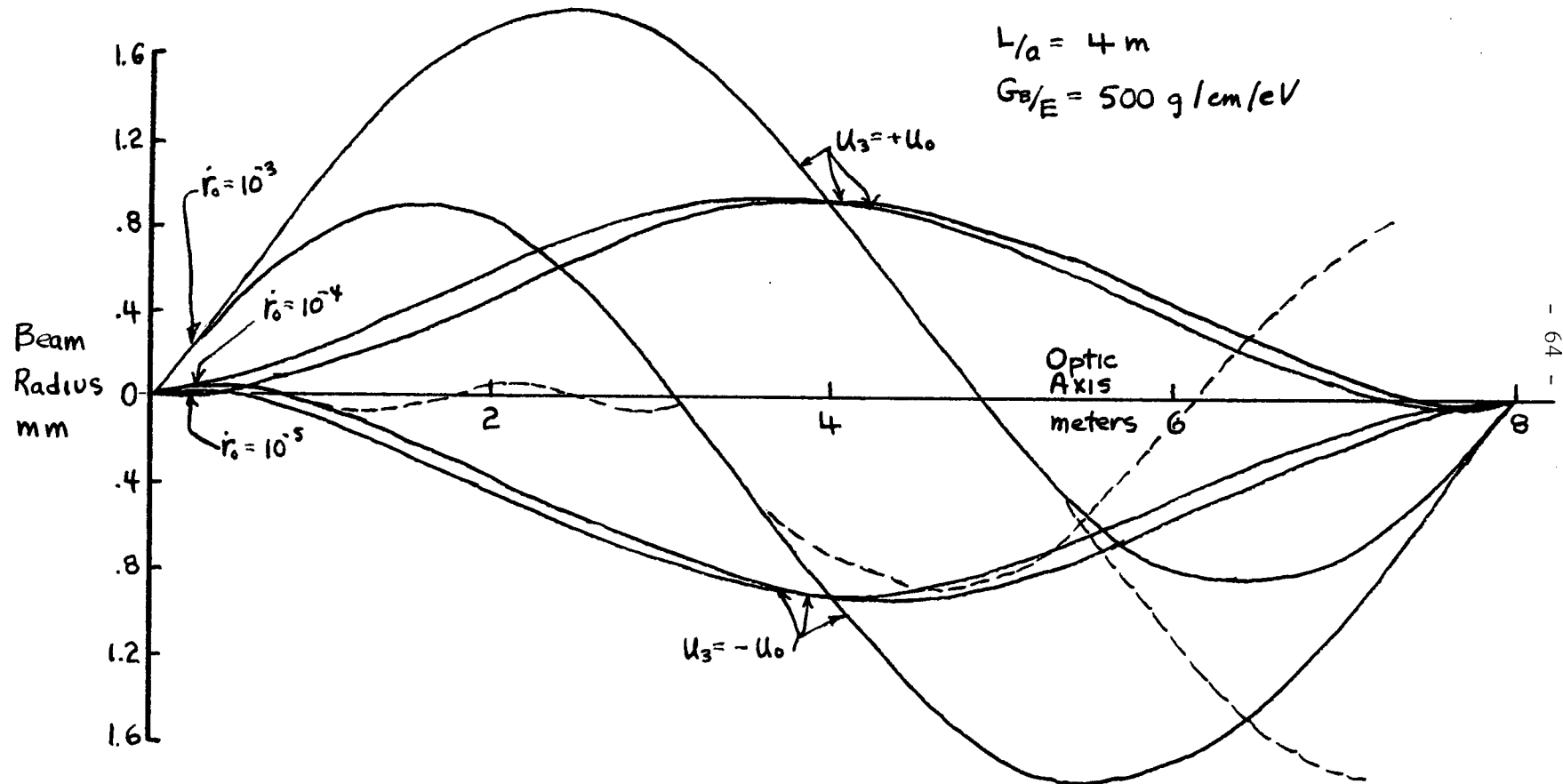


Figure 7-3. Trajectories similar to those of Fig. 7-1.

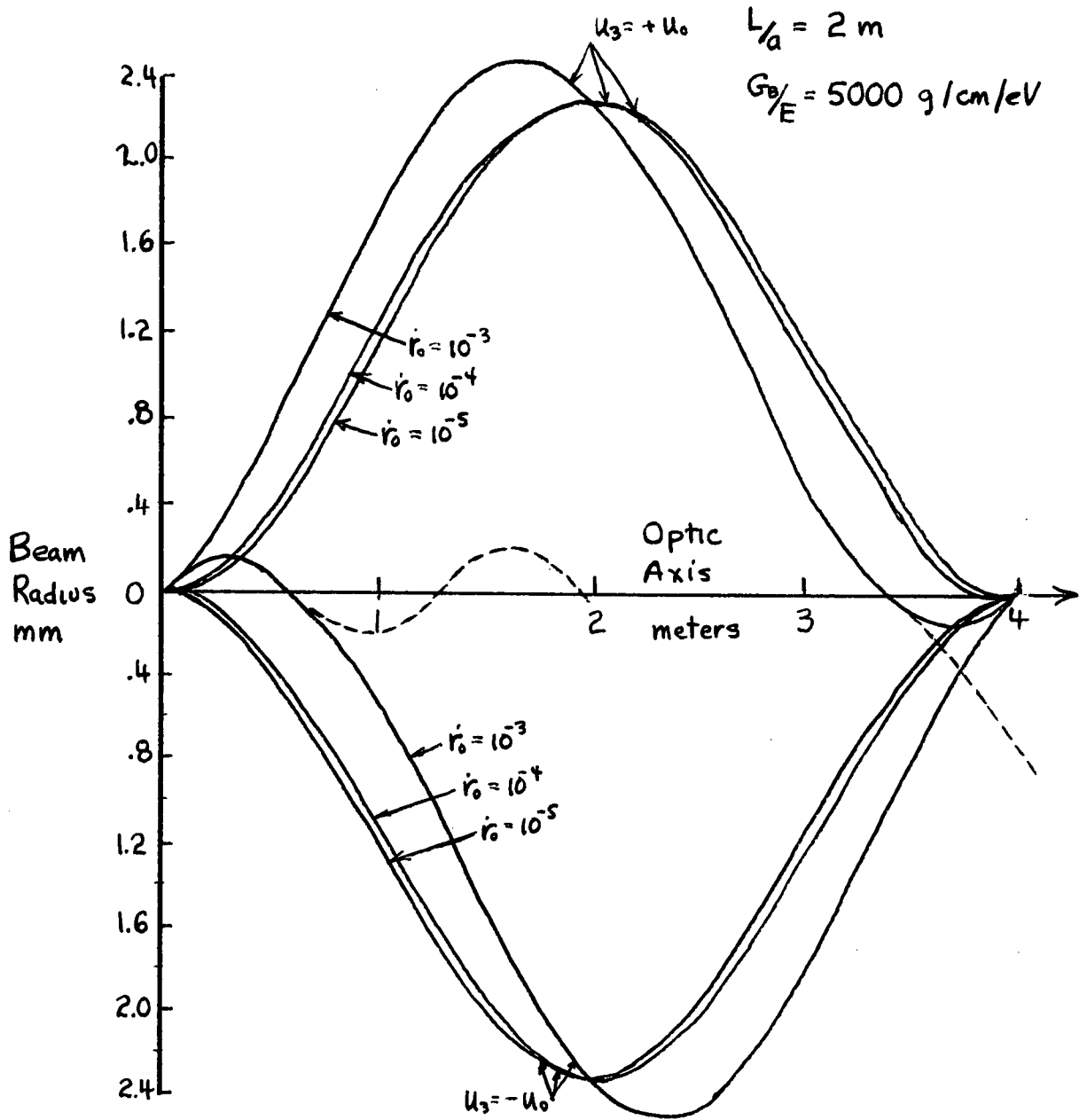


Figure 7-4. Trajectories similar to those of Fig. 7-1.

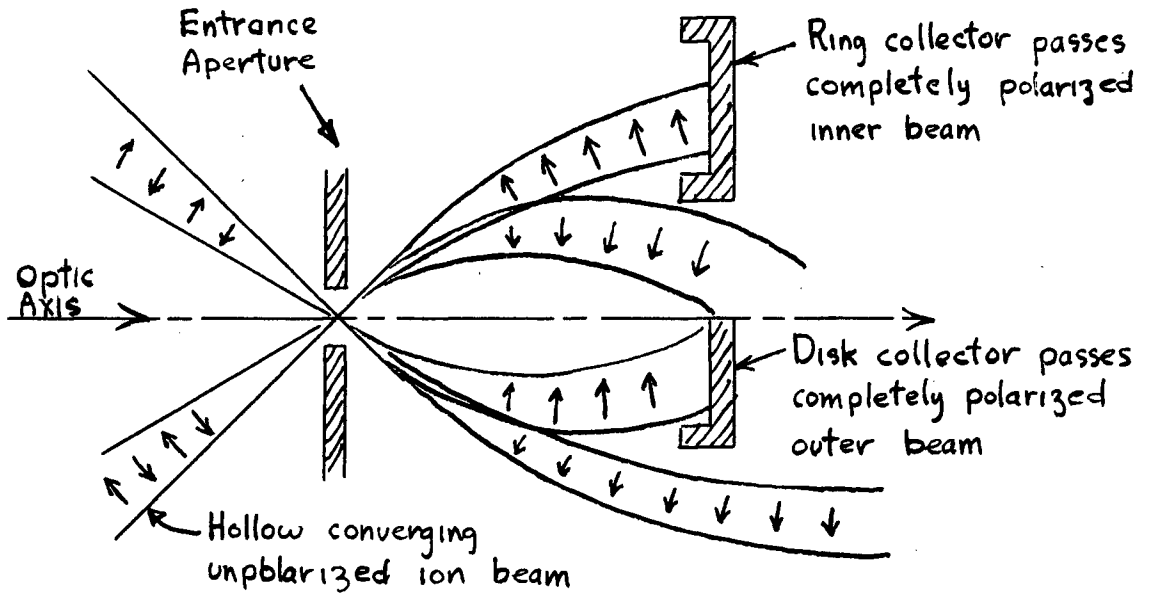


Figure 7-5. An illustration of a system of stops which would give 100% polarization of the emerging beam.

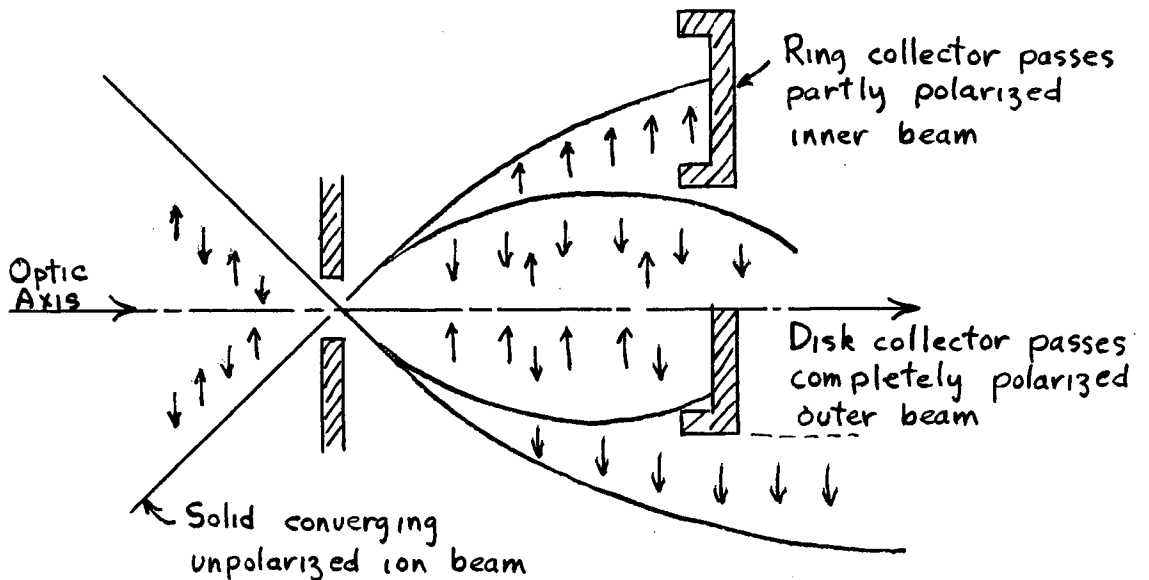


Figure 7-6. A somewhat simpler system to that illustrated in Fig. 7-5 which would give partial polarization of the inner beam.

## CHAPTER 8

### The Influence of the Solenoid Field on the Trajectories, and the Stern-Gerlach Effect for Large Lorentz Forces in a DC Helical Quadrupole

In this chapter we wish to compare the influence of the solenoid field  $B_0$  on the trajectories to that of the Stern-Gerlach force, to determine, for one thing, if it is possible to utilize the resonant nature of the  $\sin \theta$  term in the average Stern-Gerlach force (Equation 5-13). We also wish to estimate the Stern-Gerlach effect when the Lorentz force is large compared with the Stern-Gerlach force in the dc helical quadrupole system. Our conclusions are rather negative. It is doubtful that the resonant effect of the  $\sin \theta$  term can be detected by simply sweeping the field  $B_0$  on and off the resonance condition ( $\sin \theta = 1$ ) because the trajectories are modified too much by the resulting change in the Lorentz force. It is also doubtful that the Stern-Gerlach effect is usable when large Lorentz forces are present in the dc helical quadrupole. We show in this chapter that the Stern-Gerlach effect is generally small, for this case, and that to detect it would require a prohibitively stable and mechanically accurate apparatus, and a very monochromatic beam. In the light of Chapter 7, it appears that the key to a successful experiment is the near cancellation of the Lorentz force using orthogonal magnetic and electric fields.

For very small values of "r" the Stern-Gerlach force will dominate the motion, since the Lorentz force goes to zero on the optic axis, but it should be remembered that the Stern-Gerlach force is at all times very small. In equations (8-16), (8-17), and (8-18) we have expressions for the radius  $r^*$  which marks the transition between the region of space in which the Lorentz force deominates and that in which the Stern-Gerlach force dominates. If the Stern-Gerlach force dominates, the Stern-Gerlach effect will be large, but as we will show, the radius  $r^*$  usually is extremely small. Outside of the radius  $r^*$ , in the Lorentz force dominant region we have made a simple approximation to the equation of motion for a non-zero magnetic moment to estimate the minimum Stern-Gerlach effect.

Although the average Stern-Gerlach force is of a very simple form, being radial and of constant magnitude, a non-linear equation results when it is incorporated into the equation of motion.

From equation (5-13) we have;

$$\langle \bar{F}_{SG} \rangle = (\gamma \hbar J_3 \sin \theta |G_B|) \frac{\bar{r}}{r} \quad (8-1)$$

we define;

$$\xi = \gamma \hbar J_3 \sin \theta |G_B| \quad (8-2)$$

Following the development of the equation of motion in appendix B, the resulting equations when  $\langle \bar{F}_{SG} \rangle$  is included are

$$\begin{aligned} \ddot{x} - 2W\dot{y} - (W^2 + \textcircled{H} - \frac{1}{4}(\frac{q^B_0}{mv_0})^2 + \frac{\xi}{mv_0} \frac{1}{2r})x &= 0 \\ \ddot{y} + 2W\dot{x} - (W^2 - \textcircled{H} - \frac{1}{4}(\frac{q^B_0}{mv_0})^2 + \frac{\xi}{mv_0} \frac{1}{2r})y &= 0 \end{aligned} \tag{8-3}$$

The presence of the  $\xi/r$  term makes these equations non-linear.

The basis of most of this chapter is the simple approximation of replacing  $1/r$  by  $1/\langle r \rangle$ , where  $\langle r \rangle$  is a constant, representing a radius averaged over the length of the trajectory of the particle. This replacement reduces the equations (8-3) to the linear equations (b-13) by making the identification:

$$\Phi = \xi/\langle r \rangle \tag{8-4}$$

If we put  $\langle r \rangle = r_{\max}$ , this amounts to replacing the Stern-Gerlach force by a force everywhere smaller, and will certainly give a minimum for the Stern-Gerlach effect.

We cannot justify this approximation any further. It seems very reasonable, and since the results are not very encouraging we are not inclined to carry the analysis any further at this time, since an experiment based on the alternative presented in Chapter 7 appears to be very promising. Nevertheless, this kind of analysis should be quite helpful in conjunction with computer calculations of the trajectories. We believe that a computer used alone may not give as much insight as approximate solutions such as these.

It is helpful to do some preliminary analysis of the equations (b-13) which we will use as the basis for our approximate solutions.

These include the term  $\phi$ , and can be solved exactly. If both the roots  $R_1'$  and  $R_2'$  are real, the trajectories are bounded, and the solutions are as given in equation (b-22). Note that the term  $\phi$  can change the focal length, the maximum excursion, or cause a rotation about the optic axis.

If one or both of the roots become complex, the trajectories are no longer bounded, since divergent terms appear in the solutions.

Fig. 8-1 indicates the regions where the roots  $R_1'$  and  $R_2'$  are real or complex. The light regions indicate that both are real, and correspond to bounded solutions, and the shaded regions indicate that one or both are complex, corresponding to divergent solutions.

This figure is derived in the following way.

The roots may be written, from appendix B:

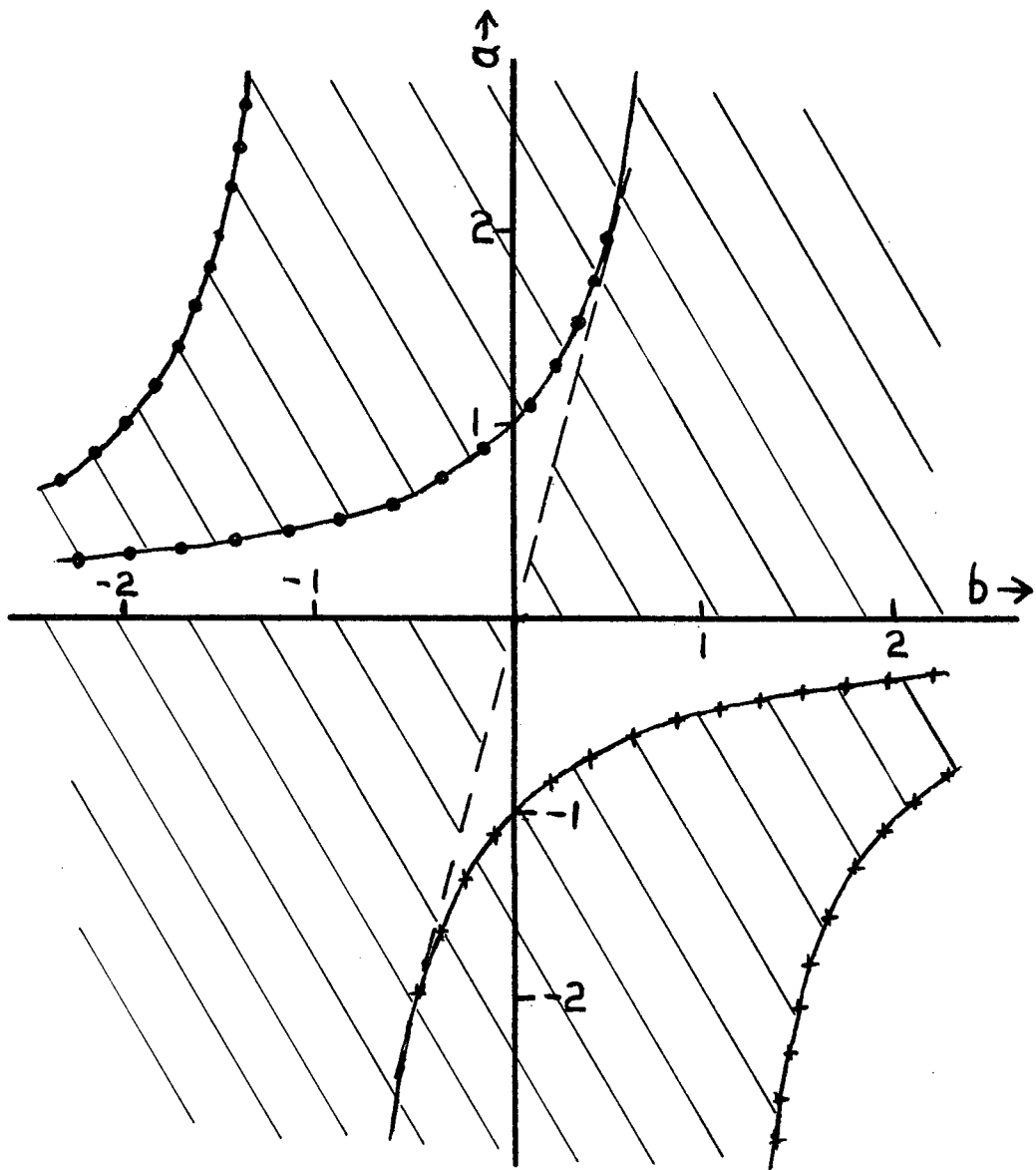
$$\begin{aligned}
 R_1' &= W \left( 1 - \frac{f}{W^2} - \sqrt{\frac{\oplus^2}{W^4} - \frac{4f}{W^2}} \right)^{1/2} \\
 R_2' &= W \left( 1 - \frac{f}{W^2} + \sqrt{\frac{\oplus^2}{W^4} - \frac{4f}{W^2}} \right)^{1/2}
 \end{aligned}
 \tag{8-5}$$

or;

$$\begin{aligned}
 R_1' &= W \left( 1 - ab - a \sqrt{1 - 4b/a} \right)^{1/2} \\
 R_2' &= W \left( 1 - ab + a \sqrt{1 - 4b/a} \right)^{1/2}
 \end{aligned}
 \tag{8-6}$$

where;

$$a = \frac{\oplus}{W^2} = \frac{q(G_E + v_o G_B)}{W^2 m v_o^2}
 \tag{8-7}$$



$$a = \frac{q}{w^2 m v_0^2} (G_E + v_0 G_B)$$

$$b = \frac{1}{G_E + v_0 G_B} \left( \frac{\Phi}{q} - \frac{q B_0^2}{4m} \right)$$

●●●●  $R_1' = 0$

++++  $R_2' = 0$

-----  $a = 4b$

Figure 8-1. A chart of the regions where the roots  $R_1'$  and  $R_2'$  are real or complex. The light regions indicate that both are real, and the shaded regions indicate that one or both are complex.

$$b = f / \Phi \quad (8-8)$$

$$= \frac{1}{(G_E + v_O G_B)} \left[ \Phi / q - \frac{q B_O^2}{4m} \right] \quad (8-9)$$

The inside radical is imaginary for;

$$\begin{aligned} 0 < a < 4b \\ -4b < a < 0 \end{aligned} \quad (8-10)$$

The line,

$$a = 4b \quad (8-11)$$

marks this boundary in Fig. 8-1.

The entire root may be zero. Putting equations (8-6) equal to zero yields;

$$\begin{aligned} R_1' = 0 \quad \text{for} \quad a = \frac{1}{1-b} \quad b \leq 1/2 \\ a = \frac{-1}{1+b} \quad b \leq -1/2 \end{aligned} \quad (8-12)$$

$$\begin{aligned} R_2' = 0 \quad \text{for} \quad a = \frac{1}{1-b} \quad b \geq 1/2 \\ a = \frac{-1}{1+b} \quad b \geq -1/2 \end{aligned} \quad (8-13)$$

These lines are drawn in Fig. 8-1.

The symmetries in this system can be utilized. They show, for example, that the lower half of Fig. 8-1 is redundant.

The transformation;

$$\begin{aligned}
 \underline{x} &\rightarrow \underline{y} \\
 \underline{y} &\rightarrow \underline{x} \\
 W &\rightarrow -W \\
 \oplus &\rightarrow -\oplus
 \end{aligned}
 \tag{8-14}$$

leaves the equations of motion (equation b-13) invariant. This is also true, of course, for the solutions.

Since the interchanging of the x and y axis corresponds to a rotation of  $\pi/2$  about the optic axis, or a translation of  $L/4$  along the optic axis; the transformations  $W \rightarrow -W$  and  $\oplus \rightarrow -\oplus$  are equivalent to one another, except for a rotation or translation.

Also, a helical field has the property that the transformations  $v_o \rightarrow -v_o$  and  $\underline{\omega} \rightarrow -\underline{\omega}$  are equivalent, except for possible rotations about, or translations along, the optic axis.

Since the roots  $R_1'$  and  $R_2'$  do not change for any of these transformations, the solutions can differ only in the initial conditions which they represent. For a beam with cylindrical symmetry no change would be noticed for the above transformations, since all initial conditions are represented. Thus the lower half of Fig. 8-1 is redundant since it represents one of the above transformations.

Referring to Fig. 8-1, a line defined by

$$|a| = \text{constant}$$

crosses three boundaries between the bounded and unbounded solution regions, provided  $|a| < 2$ . At each boundary, where a root or radical is zero, we can solve for  $\phi$  from equation (8-9), (8-11), (8-12) and

(8-13). This value of  $\Phi$  defines a radial force which is the transition between a region in which the radial Lorentz force dominates and a region in which the  $\Phi$  force dominates. Since these relations are independent of  $z$ , we can equate:

$$\Phi^* = \xi/r^* \quad (8-15)$$

where the asterisk denotes that a root or radical is zero. This relation defines a radius, which marks the transition in space between the region in which the Lorentz force dominates and that in which the Stern-Gerlach force dominates. This means that near the zero of the roots, the Stern-Gerlach force can precipitate or delay the onset of the divergent behavior within this radius.

Using equation (8-15) to define  $r^*$ , and solving for  $\Phi^*$  from equations (8-9), (8-11), (8-12), and (8-13) we obtain;

$$r_1^* = \frac{2\xi}{E(a^2W^2 + (\frac{qB_o}{mv_o})^2)} \quad (8-16)$$

for the line  $a = 4b$  in Fig. 8-1, and;

$$r_2^* = \frac{\xi}{2E\left((1-\frac{1}{a})aW^2 + 1/4(\frac{qB_o}{mv_o})^2\right)} \quad (8-17)$$

for the line  $a = \frac{1}{1-b}$  in Fig. 8-1, and;

$$r_3^* = \frac{\xi}{2E\left(-\left(1 + \frac{1}{a}\right)aW^2 + 1/4(\frac{qB_o}{mv_o})^2\right)} \quad (8-18)$$

for the line  $a = \frac{-1}{a+b}$  in Fig. 8-1.

### The Solenoid Field $B_o$

The influence of the solenoid field  $B_o$  on the Stern-Gerlach effect can be estimated from the equations in appendix B.  $B_o$  appears in the roots of the equation of motion in the terms, (equations b-14 and b-16);

$$W = \underline{\omega} + \frac{qB_o}{2mv_o} \quad (8-19)$$

$$f = \frac{\Phi}{mv_o^2} - 1/4 \left( \frac{qB_o}{mv_o} \right)^2 \quad (8-20)$$

In terms of the dimensionless parameters "a" and "b" of Fig. 8-1, these are;

$$a = \Theta / W^2 = \frac{q(G_E + v_o G_B)}{W^2 mv_o^2} \quad (8-21)$$

$$b = f / \Theta = \frac{1}{(G_E + v_o G_B)} \left[ \Phi / q - \frac{qB_o^2}{4m} \right] \quad (8-22)$$

Clearly,  $B_o$  becomes the dominant term in equation (8-22) when;

$$\left| \frac{qB_o^2}{4m} \right| > \left| \Phi / q \right| \quad (8-23)$$

and, in equation (8-19),  $B_o$  is the dominant term for

$$\left| \frac{qB_o}{2mv_o} \right| > \underline{\omega} \quad (8-24)$$

The Stern-Gerlach force can be approximated by replacing  $\phi$  with  $\xi/\langle r \rangle$ , where  $\langle r \rangle$  is approximately the aperture size of the apparatus, as outlined at the beginning of this chapter.

For a beam of particles described by;

$$\begin{aligned} & \text{He}^+ \text{ ions} \\ & E = 2\text{eV} \\ & \gamma \hbar J_3 = u_0 \text{ (Bohr magneton)} \\ & L = 2 \times 10^{-2} \text{ m} \\ & \sin\theta = 1 \end{aligned} \tag{8-25}$$

and putting

$$\langle r \rangle = 10^{-4} \text{ m}$$

equation (8-23) becomes;

$$B_0^2 > 9.6 \times 10^{-8} |G_B| \text{ (MKS)} \tag{8.26}$$

or, for  $G_B = 100$  gauss/cm;

$$|B_0| > 3.1 \text{ gauss} \tag{8.27}$$

and equation (8-24) becomes;

$$|B_0| > 2600 \text{ gauss} \tag{8.28}$$

It can be seen from equation (8-27) that rather small values of  $B_0$  will dominate the Stern-Gerlach effect. This seems to preclude using a swept  $B_0$  mode for detecting the effect, as we will further illustrate.

The reason for including the solenoid field  $B_0$  is, of course, to maximize the Stern-Gerlach effect via the term  $\sin \theta$  (eqn. 5-14). To illustrate, we can calculate  $B_0$  to maximize  $\sin \theta$ , and also determine

the resonance width, for the case with;

$$\begin{aligned}
 L &= 2 \times 10^{-2} \text{ cm} \\
 G_B &= 1000 \text{ g/cm} \\
 E &= 2 \text{ eV} \\
 \text{He}^+ &= \text{beam ion} \\
 \gamma \hbar J_3 &= u_0 \\
 r_{\text{max}} &= 6 \times 10^{-4} \text{ m} \\
 \omega_L &\ll 2\omega_0
 \end{aligned}
 \tag{8-29}$$

These values could apply, for example, to the trajectories drawn in Figs. 7-1 to 7-3.

Putting  $\Delta\omega = 0$  to maximize  $\sin \theta$ , yields, from equations (5-7) and (5-9);

$$B_0 = -\frac{1}{2.8} \text{ gauss} \tag{8.30}$$

The half-width at half-maximum of  $\sin \theta$  is;

$$(\Delta\omega)_{1/2} = \pm\sqrt{3}\omega_1 \tag{8-31}$$

It is, of course, determined by the maximum radius of the particle trajectory, and for the example cited,  $r_{\text{max}} = 6 \times 10^{-4} \text{ m}$ ; we have;

$$\begin{aligned}
 B_1(\bar{r})_{\text{max}} &= G_B r_{\text{max}} && \text{(eqn. 5-6)} \\
 &= 60 \text{ gauss} && \tag{8.32}
 \end{aligned}$$

Therefore the half-width is;

$$\frac{(\Delta\omega)_{1/2}}{\gamma} \sim 100 \text{ gauss} \quad (8-33)$$

Comparing equations (8-30) and (8-33), we can conclude that the resonance is essentially centered about  $B_0 = 0$ , and that this broad resonance would be difficult to distinguish from the trajectory changes produced by the Lorentz forces for changing  $B_0$ , as noted earlier.

It is possible to design the apparatus to enhance the resonance effect in order to simplify detection. This could involve choosing an ion with a smaller  $\gamma$ , increasing  $\omega$ , increasing  $E$ , decreasing  $r_{\max}$ , or decreasing  $G_B$ . These steps all seem to reduce the overall effect, so the compromise which must be made, sacrificing the size of the signal in order to sharpen the resonance, must be decided entirely in terms of signal to noise with whatever detection scheme is proposed.

We have treated the case for small  $\Phi$  in Chapter 7, now we consider the remaining range of  $\Phi$  using the approximation outlined in the introduction to this chapter. The easiest way to do this is to put  $G_E = B_0 = 0$ . This does not leave out much information for the practical reason that the magnetic field gradient  $G_B$  alone is sufficient to make  $\Phi$  large. The only reason for introducing  $G_E$  is to reduce  $\Phi$ , to minimize the effects of a large  $\Phi$  on the Stern-Gerlach effect. The effect of  $B_0$  has been considered separately in this chapter by noting when it becomes the dominant term in the expressions  $f$  and  $W$ .

#### The simple magnetic helical quadrupole

$$B_0 = G_E = 0$$

The term "b" has a simple interpretation for this case. From equation (8-9) we have;

$$b = \frac{\Phi}{qG_B v_o} \quad B_o = G_E = 0 \quad (8-34)$$

This is just the ratio of the radial force term ( $\Phi r$ ) to the Lorentz force ( $qG_B v_o r$ ). If  $\Phi$  represents the Stern-Gerlach force, then one would expect "b" to be rather small.

If we take, as typical values, the experimental parameters of equations (8-25), and put  $\Phi = \xi / \langle r \rangle$ , then;

$$b \sim 6 \times 10^{-5} \quad (8-35)$$

The region of interest is clearly close to  $b = 0$  in Fig. 8-1.

Some simple estimates of the effects on the trajectories due to different values of "b" can be made.

Differentiating equation (8-6) we get, for constant "a";

$$\Delta R_1' = \frac{W^2 \Delta b}{2R_1'} \left( \frac{2}{\sqrt{1-4b/a}} - a \right)$$

$$\Delta R_2' = - \frac{W^2 \Delta b}{2R_2'} \left( \frac{2}{\sqrt{1-4b/a}} + a \right) \quad (8-36)$$

If we consider only changes about  $b = 0$ , and find the relative change by dividing through by the root  $R_1'$  or  $R_2'$ , we get;

$$\frac{\Delta R_1'}{R_1'} = \frac{\Delta b}{2} \left( \frac{2-a}{1-a} \right), \quad b = 0 \quad (8-37)$$

$$\frac{\Delta R_2'}{R_2'} = - \frac{\Delta b}{2} \left( \frac{2+a}{1+a} \right), \quad b = 0$$

Except for the regions near  $a = \pm 1$ , these terms are very small since  $\Delta b$  is very small. Using the approximation  $\phi = \xi / \langle r \rangle$ , and differentiating equation (8-34)

$$\Delta b = \left( \frac{\gamma \hbar \sin \theta}{qv_0 \langle r \rangle} \right) \Delta J_3 \frac{|G_B|}{G_B} \quad (8-38)$$

Using the parameter values of equations (8-25), and putting  $\gamma \hbar \Delta J_3 = 2u_0$ , we obtain;

$$b \sim 10^{-4} \quad (8-39)$$

From equations (8-37) and (8-39) it is obvious that the trajectory changes that this will cause will be of the order of 1 part in  $10^4$ , unless "a" is very near  $\pm 1$ .

If we suppose that the focal point changes by 1 part in  $10^4$  due to the Stern-Gerlach effect, then the most obvious difficulty in detecting it is the chromatic aberration of this system. If we take as a first approximation, that the focal length varies as (equation 6-10);

$$z_f = \frac{2\pi\omega}{\oplus} = \frac{2\pi\omega m v_0}{qG_B} \quad (8-40)$$

then the velocity of the beam and hence its energy must be constant to better than about 1 part in  $10^4$ . This result seems typical of operation in the region between very small "a" ( $a \sim 0$ ) and large "a" ( $a = \pm 1$ ). That is, a small effect is present, but to detect it requires a nearly monochromatic beam.

From equation (8-17), for  $a \approx 1/2$ ,  $\gamma \hbar J_3 = u_0$ ,  $E = 2eV$ ,  $B_0 = 0$ , we obtain;

$$r_2^* \sim 10^{-8} \text{ m}$$

Thus, only within this very small radius would we expect a large Stern-Gerlach effect for the operating region just discussed, which is consistent with our conclusion that at a radius of  $10^{-4}$  m, only a very small effect is present.

Now consider the regions very near  $a = \pm 1$ . If we put  $a = \pm 1$ , we note that for small "b", the roots given by equation (8-6) can be expanded. Consider the case for  $a = 1$  then;

$$\begin{aligned} R_1' &\approx \underline{\omega} \sqrt{b} \\ R_2' &\approx \underline{\omega} \sqrt{2-3b} \end{aligned} \tag{8-41}$$

also  $\delta \approx \underline{\omega}^2$  (from equation b-19)

$\textcircled{H} \approx \underline{\omega}^2$  (from equation b-15)

Put  $x_0 = y_0 = 0$

Then for  $b > 0$ , the roots are real, and we can simplify equation (b-22) with the above terms:

$$\begin{aligned} \underline{x} &\approx \dot{x}_0 \frac{\sin \sqrt{2} \underline{\omega} z}{\underline{\omega} \sqrt{2}} + \frac{\dot{y}_0}{\underline{\omega}} (\cos \underline{\omega} \sqrt{b} z - \cos \sqrt{2} \underline{\omega} z) \\ \underline{y} &\approx - \frac{\dot{x}_0}{\underline{\omega}} (\cos \sqrt{b} \underline{\omega} z - \cos \sqrt{2} \underline{\omega} z) + \frac{\dot{y}_0}{\underline{\omega}} (\sqrt{2} \sin \sqrt{2} \underline{\omega} z - \frac{\sin \sqrt{b} \underline{\omega} z}{\sqrt{b}}) \end{aligned} \quad (8-42)$$

with

$$4b \ll 1$$

$$a = 1$$

$$B_0 = 0$$

$$b > 0$$

Since  $\sqrt{b} \ll \sqrt{2}$ , the focal length of these equations is very near;

$$z_f \approx \frac{\pi}{\sqrt{b} \underline{\omega}} \quad (8-43)$$

If we put  $\Phi = \xi / \langle r \rangle$  to represent the Stern-Gerlach force over this focal distance, we can estimate "b" as in equation (8-35), for "typical" parameter values such as those in equation (8-25).

Taking;

$$\begin{aligned} b &\approx 10^{-4} \\ L &= 2 \times 10^{-2} \text{ m} \end{aligned} \quad (8-44)$$

we obtain from equation (8-43)

$$z_f \approx 1 \text{ meter}$$

The maximum excursion of the equation (8-42) is determined mainly by the factor:

$$r_{\max} \approx \frac{\dot{y}_0}{\sqrt{b} \underline{\omega}} \quad (8-45)$$

If we again put  $\phi = \xi / \langle r \rangle$  to represent the Stern-Gerlach force over the range of one focal length ( $z_f$ ), then  $r_{\max}$  will be somewhat greater than  $\langle r \rangle$ . A conservative estimate is to put  $r_{\max} = \langle r \rangle$ . Then we can say, from equation (8-45), that all particles entering the system within the angle given by:

$$\dot{y}_0 = \langle r \rangle \omega \sqrt{b} \quad (8-46)$$

will be focused within the distance  $z_f$  (equation 8-46). Using the values of equation (8-44).

$$\dot{y}_0 = \pi \times 10^{-4} \quad (8-47)$$

This establishes that a cone of particles with  $b > 0$  will be focused within a reasonable distance in this system. Consider now the particles with  $b < 0$ . The root  $R_1'$  in equations (8-41) is imaginary, so that the solutions (8-42) will be diverging. Computing;

$$r^2 = \underline{x}^2 + \underline{y}^2$$

we have from equation (8-42):

$$\begin{aligned} r^2 = & \left( \frac{\dot{x}_0^2}{4} + \dot{y}_0^2 \right) \frac{2 \sin^2 \sqrt{2} \omega z}{\omega^2} + \frac{\dot{r}_0^2}{\omega^2} \left( \cosh^2 \omega \sqrt{|b|} z + \cos^2 \sqrt{2} \omega z \right. \\ & - 2 \cosh \omega \sqrt{|b|} z \cos \sqrt{2} \omega z \left. \right) - \dot{x}_0 \dot{y}_0 \frac{\sqrt{2}}{\omega} \sin \sqrt{2} \omega z \left( \cosh \omega \sqrt{|b|} z \right. \\ & \left. - \cos \sqrt{2} \omega z \right) - \frac{2 \sqrt{2} \dot{y}_0^2}{\omega^2 \sqrt{|b|}} \sin \sqrt{2} \omega z \sinh \sqrt{|b|} \omega z + \frac{\dot{y}_0^2}{\omega^2 |b|} \sinh^2 \sqrt{|b|} \omega z \\ & + \frac{\dot{x}_0 \dot{y}_0}{\omega^2 \sqrt{|b|}} \sinh \sqrt{2} \sqrt{|b|} \omega z - \frac{2 \dot{x}_0 \dot{y}_0}{\omega^2 \sqrt{|b|}} \sinh \sqrt{|b|} \omega z \cos \sqrt{2} \omega z \end{aligned} \quad (8-48)$$

where  $\sqrt{|b|} \ll \sqrt{2}$

$$b < 0$$

$$a = 1$$

$$B_0 = 0$$

For small  $z$  this is oscillatory at  $\sqrt{2}\omega z$ , but as  $z$  gets larger, the oscillating terms become less important and the dominant term becomes;

$$r \approx 1/2 \frac{\dot{y}_0}{\omega \sqrt{|b|}} \sinh \sqrt{|b|} \omega z \quad (8-49)$$

If we make the conservative estimate that;

$$r = \langle r \rangle = r \text{ aperture}$$

and if we put  $\Phi = \xi/\langle r \rangle$  to represent the Stern-Gerlach force over a distance equivalent to the focal length for particles with  $b > 0$ ;

$$z_f = \frac{\pi}{\sqrt{|b|} \omega}$$

then equation (8-49) gives a conservative estimate of the minimum angle which a particle may enter the system with in order to be expelled beyond the radius of the aperture in the distance  $z_f$ .

Using the parameter values of the previous example, except that  $b = 10^{-4}$ , we obtain from equation (8-49)

$$\dot{y}_0 > 5 \times 10^{-5}$$

This is a very conservative estimate, and it indicates that most particles with  $b = -10^{-4}$  would be expelled from this system out to the radius of  $10^{-4}$  meters within a distance of one meter of flight.

This example has shown that it might be possible to operate a magnetic helical quadrupole in the  $a = 1$  region and achieve a particle separation from the Stern-Gerlach force. An obvious problem is to maintain the  $a = 1$  condition with sufficient precision. For example, noting in Fig. 8-1, that the slope of the line  $R_1' = 0$  at  $a = 1$  is 1, we can estimate that "a" must be constant to at least the order of "b", if the apparatus is to separate the  $b < 0$  particles in a diverging mode, and focus the  $b > 0$  particles. If  $b \sim 10^{-4}$ , then "a" must be constant to about 1 part in  $10^4$  or better. We have, from equation (8-21);

$$a = \frac{qG_B}{\omega^2 m v_0}$$

Thus both the gradient  $G_B$ , and the beam velocity  $v_0$  must be constant to about 1 part in  $10^4$  or better.

We can arrive at the same conclusions from equation (8-17) which for this case can be written;

$$r_2^* = \frac{\gamma \hbar J_3 \sin \theta}{q v_0 (1 - 1/a)} \frac{|G_B|}{G_B} \quad (8-50)$$

Putting  $a = 1$  yields  $r_2^* = \infty$ , which confirms the result that a large effect can be expected for the  $a = 1$  region, and indicates that at the point of instability for the Lorentz force alone ( $a = 1$ ), any

small additional radial force is sufficient to dominate the motion, in the sense that it will precipitate or delay the instability, for any  $r$ .

Equation (8-50) also yields the same stability criterion, for if we put  $r_2^* = 10^{-4}$  m, the average radius which we have considered, we can solve for "a" to obtain  $a \approx 1 + 10^{-4}$ . Thus "a" must be constant to about 1 part in  $10^4$  or better, if the Stern-Gerlach force is to dominate out to the radius of  $10^{-4}$  m.

## CHAPTER 9

### Experimental Considerations

In this chapter some general remarks are made concerning the design of helical quadrupoles and some justification is given for the choice of the parameter values used in the examples of Chapters 6 to 8.

To begin with we will determine the relations between step length, aperture size, gradient and minimum power for a helical quadrupole system. Let  $R_0$  be the radius of a helix, let  $L$  be the step length, and  $L_T$  the total length as shown in Fig. 9-1. Then the total length of the helical line is  $L_{HT}$ ;

$$L_{HT} = L_T \sqrt{1 + q^2/4} \quad (9-1)$$

$$q = \frac{4\pi R_0}{L} \quad (9-2)$$

If  $d$  is the width of a helical strip, (Fig. 9-1) then  $D$ , the width measured longitudinally is;

$$D = d \sqrt{1 + 4/q^2} \quad (9-3)$$

If four wires are to be wound then the width of each wire cannot exceed

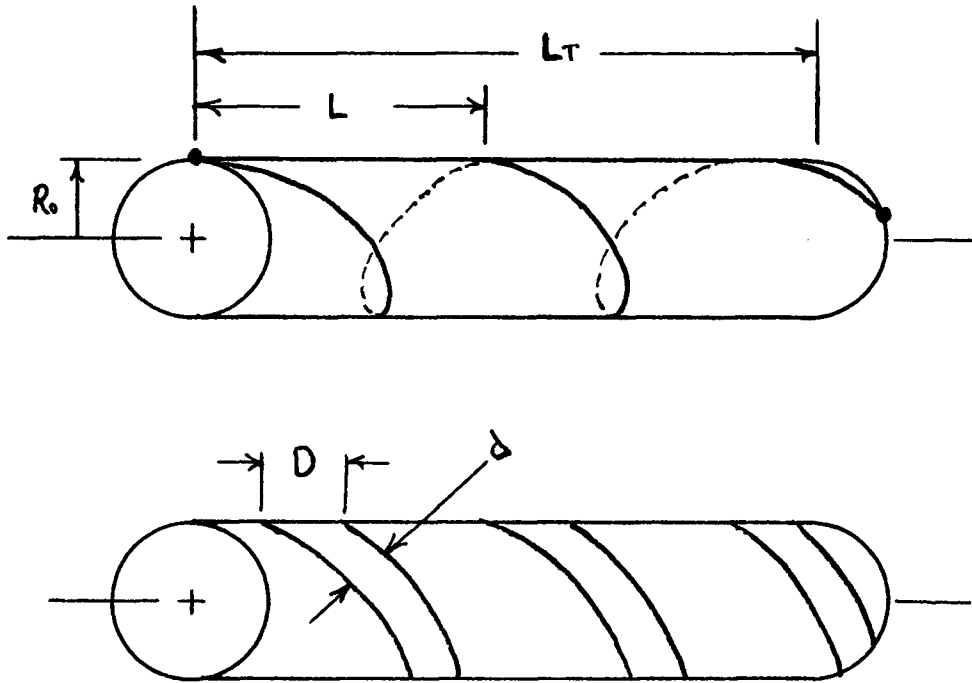


Figure 9-1. Illustration of the dimensions of a helical line and a helical strip.

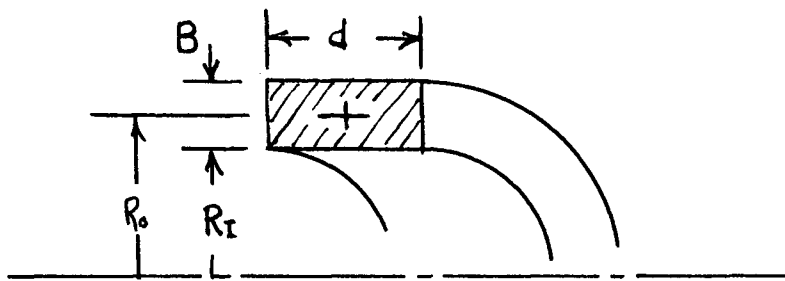


Figure 9-2. Illustration of the dimensions of a rectangular wire helical winding.

$$d \leq \frac{R_o}{2 \sqrt{1 + q^2/4}} \quad (9-4)$$

For a fixed amount of power (P), the maximum magnetic field gradient ( $G_B$ ) is obtained if the depth of the wire (B) is 2/3 the inner radius ( $R_I$ ) of the wire, for fixed wire width (d) (see Fig. 9-2), assuming rectangular wire is used. To show this we have, from appendix A;

$$G_B \propto \frac{I}{R_o^2} \propto \frac{\sqrt{P}}{R_o^2 \sqrt{R}} \quad (9-5)$$

where  $R_o$  is the radius to the center of the wire and R is the wire resistance. Assume d is constant, and  $R_I$  is constant, then;

$$G_B \propto \frac{\sqrt{B}}{(R_I + B/2)^2} \quad (9-6)$$

differentiating, we find  $\frac{dG_B}{dB}$  is a maximum for;

$$B = 2/3R_I \quad (9-7)$$

The minimum resistance occurs when B satisfies equation (9-7) and "d" satisfies the equality in equation (9-4). For a single helical winding of solid, rectangular, copper wire, this resistance is

$$R_{\min} = \frac{4(1.7 \times 10^{-8})L_T(1 + q^2/4)A}{\pi R_o^2} \quad (\text{MKS}) \quad (9-8)$$

where A is a "filling factor" to allow for insulation on the wires.

For the case of wires with a finite width "d", the factor  $\frac{\sin\phi}{\phi}$  must be included in the expression for  $G_B$ , from appendix A;

$$G_B = C(q) \frac{(8 \times 10^{-7})I}{R_o^2} \frac{\sin\phi}{\phi} \text{ (MKS)} \quad (9-9)$$

where  $\phi = \underline{\omega d}$

When the space between the wires is very small,  $\frac{\sin\phi}{\phi}$  is at its smallest value which is;

$$\frac{\sin\phi}{\phi} = .63, \phi = \pi/2 \text{ (D = L/4)} \quad (9-10)$$

From equations (9-9) and (9-10), for conditions of minimum resistance;

$$P_{\min} = \frac{(3.94 \times 10^{12})G_B^2 R_o^4 R_{\min}}{C^2(q)} \text{ (MKS)} \quad (9-11)$$

To illustrate, consider systems similar to those used as examples in Chapters 7 and 8. Typical values are;

$$L = 2 \times 10^{-2} \text{ m}, 4 \times 10^{-2} \text{ m}, 6 \times 10^{-2} \text{ m}$$

$$G_B = 1000 \text{ g/cm}$$

$$L_T = 1 \text{ m}$$

The radius  $R_o$  may chose to minimize the power, consistent with the aperture required for the beam. Fig. 9-3 is a plot of  $P_{\min}$  from equation (9-3) versus  $R_o$  for the values given above.

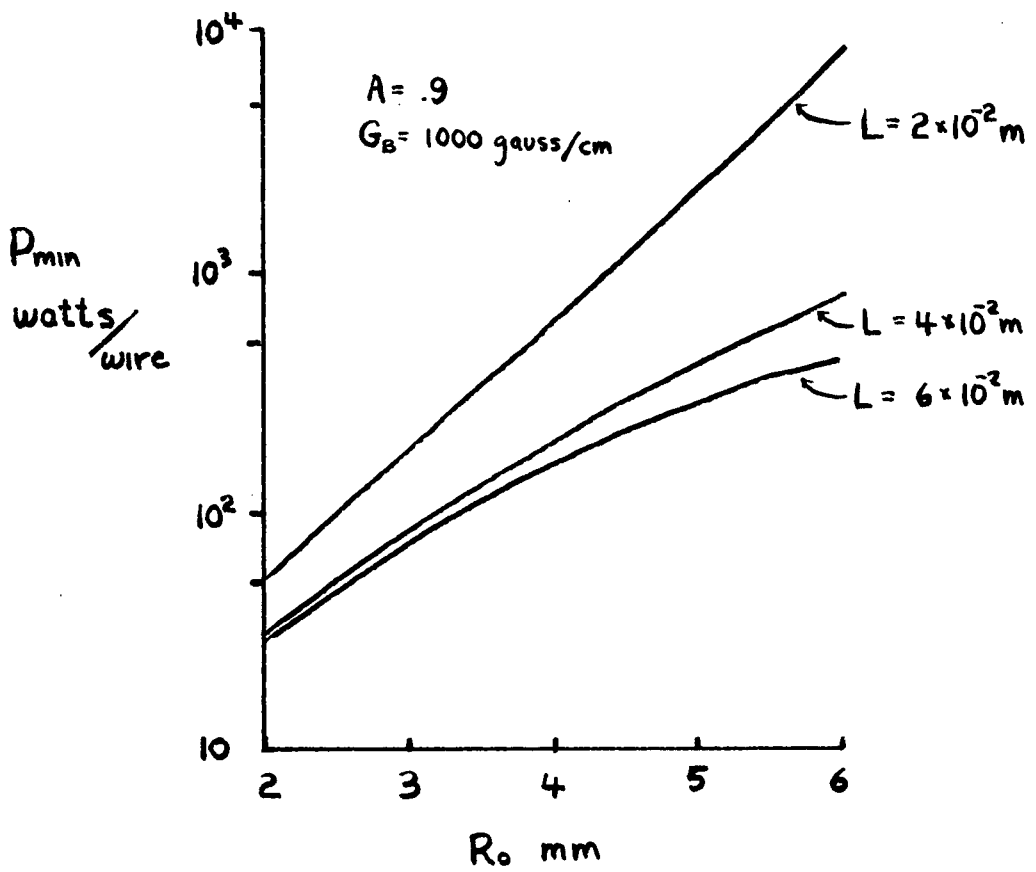


Figure 9-3. Plot of minimum power versus wire radius for a rectangular copper wire helical winding at room temperature, from equation (9-11).

Quite clearly, the relation between the aperture size, pitch length, and the power required to produce a given gradient  $G_B$  is an important consideration in design. For a given system, the maximum gradient ( $G_B$ ) will be determined by the cooling capacity. The value chosen for most of the examples in Chapters 7 and 8 was  $G_B = 1000$  gauss/cm. This is a very conservative value. It can easily be produced as illustrated in Fig. 9-3 for aperture sizes consistent with the beam size. It should be possible to increase  $G_B$  to at least  $10^4$  gauss/cm in a practical system; which would apply, for example, to the trajectories plotted in Fig. 7-4, for a 2eV beam.

Increasing the Stern-Gerlach force (i.e., by increasing  $G_B$ ) has the important additional advantage, besides increasing the Stern-Gerlach effect, that the slow ions will be less subject to stray fields and "dirt" effects, because of the focusing effect of this force.

### The Ion Beam

From the theory of Chapters 6 through 8 it is evident that the ion beam is a very important consideration in designing the apparatus. Foremost, it is necessary to have a beam which is small in cross section and well collimated, secondly, it should be as intense, pure, and monochromatic as possible, consistent with a very low energy. Obviously, a compromise must be made between these requirements.

For the purpose of giving examples in Chapters 7 and 8 we assumed a beam energy of 2eV. With care, it seems possible to achieve such a beam with the required size and collimation, and an intensity measured at least in tens of particles/sec. It should be kept in mind, however,

that the Stern-Gerlach effect is approximately proportional to  $G_B/E$  (see, for example, equation 7-23) so that reducing the beam energy is equivalent to increasing the magnetic field gradient by a like amount.

A large literature exists on ion sources, but most of this work has been to develop intense sources of fast ions, and typically the energy spread is of the order of a volt. An intense source of slow Argon ions has been reported by F. Hushfar et al. (1967). They obtain a beam intensity of  $10^{14}$  particles/cm<sup>2</sup>sec at an average energy of 2eV using a plasma source and a novel extraction system which allows both electrons and ions to be simultaneously extracted in a space charge neutralized beam. However, the energy spread appears to be large, about a volt, which is typical of most plasma sources.

Two good sources of slow ions adaptable to a wide variety of ions, are photoionization and electron bombardment sources. Of the two, photoionization can produce the most monochromatic beam. Weissler et al. (1959) using a well defined beam of ultraviolet radiation obtained from a Seya-Namioka grating monochromator could produce ions at 9 eV with an energy spread of .04 eV. However, the yield of ions is much lower than that attainable with electron bombardment.

It is useful to give a brief analysis of the electron bombardment source as a source of ions for this experiment. The rate of ion production is given approximately by the formula;

$$R = n_o \sigma(v_e) n_e v_e \frac{\text{ions}}{\text{cm}^3 \text{sec}} \quad (9-12)$$

where

- $n_o$  = number density of atoms  
 $\sigma(v_e)$  = the velocity dependent ionization  
cross section in square centimeters  
 $n_e v_e$  = the number of electrons/cm<sup>2</sup>/sec

If we consider the ionization of He to He<sup>+</sup>, with a source pressure of  $5 \times 10^{-4}$  Torr, then;

$$n_o = 1.6 \times 10^{13} \text{ atoms/cm}^3$$
$$\sigma(v_e) = 3.3 \times 10^{-17} \text{ cm}^2$$

(W.E. Lamb, Jr., and M. Skinner, 1950)

Typical electron densities are from  $1 \times 10^{16}$  electrons/cm<sup>2</sup>/sec with a "weak" source up to  $38 \times 10^{16}$  electrons/cm<sup>2</sup>/sec in a "strong" source such as that of Plumlee (1957).

If we assume  $n_e v_e = 5 \times 10^{16}$  electrons/cm<sup>2</sup>/sec, then

$$R = 2.6 \times 10^{13} \text{ ions/cm}^3/\text{sec} \quad (9-13)$$

We now omit all details of ion extraction and focusing, and simply assume that the ions all originate in a small sphere which radiates ions at the rate R into the solid angle  $4\pi$ . If we take the diameter of this sphere to be equal to the diameter of the beam, then we would expect a beam of diameter .050 cm, and a divergence  $\dot{r}_o = \frac{\Delta r}{\Delta z} = 10^{-3}$  to have an intensity of;

$$2.6 \times 10^{13} \times 4/3\pi (.025)^3 \times \frac{(2 \times 10^{-3})^2}{4\pi} \approx 540 \text{ ions/sec} \quad (9-14)$$

This performance was achieved at a beam energy of 4eV in the ion gun described in appendix C.

The rate of ion production given in equation (9-13) is typical. Lipeles (1966) reports this value in an ion source similar to that of Novick and Commins (1958). With a beam diameter of about .4 cm and a divergence of  $\dot{r}_0 = 0.6$ , he obtains a beam intensity of  $3 \times 10^{10}$  ions/sec. at a beam energy of 10 eV. He also measured the energy spread to be almost .4 eV or 4% for his beam. His beam intensity, compared with that of equation (9-14) illustrates the very large decrease in total particles/sec which one must expect when the same source is used to produce a smaller diameter and better collimated beam.

A very serious problem with slow ion beams is the rapid fall in intensity below an energy of some 10 eV. For example, the ion gun described in appendix C would produce a beam about two orders of magnitude more intense at 10 eV than at 4 eV beam energy, as illustrated in Fig. C-2. Much of this is due to the collimating effect of the lens system, which increases the effective solid angle at the ion source at higher beam energies. However, at a beam energy of 3 eV, the ion count was equal to the metastable background count, some two orders of magnitude below the intensity at 4 eV. This very rapid fall (beam cut off) is typical of these sources and is apparently due to stray fields. Our own experience was that the cleanliness of the aperture next to the ionizer exit aperture had a pronounced effect on the beam cut-off. This aperture is presumably intercepting a large flux of electrons and ions from the ionizer and could conceivably contaminate very quickly.

We have tentatively concluded that an ion beam at 2 eV

with an intensity of some tens of particles/sec can be produced with an electron bombardment source in a clean vacuum system; and with the required size and collimation for the examples given in Chapter 7. However, we believe that an apparatus could be designed to polarize a much larger and more intense beam, but this would require a major effort of engineering.

## CHAPTER 10

### Concluding Remarks

This thesis has added essentially two new ingredients for consideration to the conditions for which a charged particle generalized Stern-Gerlach experiment can be successfully performed, from those previously reported (Bloom and Erdman 1962; Rastall 1962; Byrne 1963; Bloom, Enga and Lew 1967). These new considerations are the extension of the Transverse Stern-Gerlach experiment to time independent, space varying inhomogeneous magnetic fields given by equation (1-2), and the introduction of an electric field  $\vec{E}(\vec{r})$  which is orthogonal to the magnetic field  $\vec{B}_1(\vec{r})$  (equation 1-2) in the plane transverse to the general particle motion. The development of these new considerations in Chapters 5 through 9 indicates that the experiment is considerably simplified from that previously envisaged, and that no fundamental difficulty remains to the successful execution of a charged particle Stern-Gerlach experiment.

The most fruitful application of such an experiment would probably be the precision measurement of the low-lying energy levels of a wide variety of ions and molecular ions, which are of great interest in chemistry and astrophysics. Very few methods have proven useful for such measurements. We believe that the generalized Stern-Gerlach

experiment will now allow the study of such ions in the same general way that the Stern-Gerlach experiment has been applied to the study of atoms and molecules.

Another application is the construction of a polarized ion source for use in nuclear physics. Such sources as are presently in use ionize after atomic state selection, whereas this experiment makes possible the state selection after ionization. This difference may prove to be important in future designs. A short review of polarized ion sources now in use is given by Drake (1967).

BIBLIOGRAPHY

- Abraham, A. 1961. Principles of Nuclear Magnetism (Oxford University Press, London).
- Bas, Von E.B. and Gaug, H. 1968. Z. Angew, Math Phys. (Switzerland), Vol. 18, No. 4, 557.
- Bennewitz, H.G. and Paul, W. 1954. Z. Physik 139, 489.
- Bloom, M. and Erdman, K.L. 1962. Can. J. Phys. 40, 179.
- Bloom, M., Enga, E. and Lew, H. 1967. Can. J. Phys. 45, 1481.
- Byrne, J. 1963. Can. J. Phys. 41, 1571.
- Drake, Jr., C.W. 1967. Atomic and Electron Physics, Vol. 4 pp. 226-257 (Academic Press, New York and London).
- Greene, E.F. 1961. Rev. Sci. Instr. 32, 860.
- Hanszen, K.-J. and Lauer, R. 1967. Focusing of Charged Particles, Vol. I, pp. 251-307, (Academic Press, New York and London).
- Hushfar, F., Rogers, J.W. and Webb, D. 1967. Rarefied Gas Dynamics Fifth Symposium, Vol. II, pp. 1427-1442 (Academic Press, New York).
- Kusch, P. and Hughes, V.W. 1959. Handbuch der Physik, Vol. 37 (Springer Verlag), pp. 1-172.
- Lamb, Jr. W.E. and Skinner, M. 1950. Phys. Rev. 78, 539.
- Le Couteur, K.J. 1967. Plasma Physics, Vol. 9, 457.
- Lipeles, M. 1966. Thesis, Columbia University (unpublished).
- Lippert, W. and Pohlit, W. 1952. Optik 9, 456.
- Lippert, W. and Pohlit, W. 1953. Optik 10, 447.
- Novick, R. and Commins, E.D. 1958. Phys. Rev. 111, 822.
- Pearce, R.M. 1969. University of Victoria, Private communication.

- Pierce, J.R. 1954. Theory and Design of Electron Beams, second edition. (De. Van Nostrand and Co., New Jersey).
- Plumlee, R.H. 1957. Rev. Sci. Instr. 28, 830.
- Ramsey, N.F. 1963. Molecular Beams (Oxford University Press, reprinted from first edition, 1955).
- Rastall, P. 1962. Can. J. Phys. 40, 1271.
- Salardi, G., Zanazzi, E. and Uccelli, F. 1968. Nuclear Instr. and Methods, 59, 152.
- Strashkevich, A.M. and Trotsyuk, N.I. 1968. Soviet Physics - Technical Physics, Vol. 13, no. 3, 384.
- Teng, L.C. 1959. Helical Quadrupole Magnetic Focusing Systems, ANAL-55 February.
- Trotsyuk, N.J. 1969. Soviet Physics - Technical Physics, Vol. 13, No. 7, 944.
- Watson, G.N. 1962. Theory of Bessel Functions, Second Ed. (Cambridge University Press).
- Weissler, G.L., Samson, J.A.R., Ogawa, M., and Cook, G.R. 1959. J. Opt. Soc. Am. 49, 338.
- Winter, J. 1955. Compt. Rend. Acad. Sci. 241, 375.
- Zankel, K. 1968. Nuclear Instr. and Methods 65, 322.

APPENDIX A

The Helical Quadrupole Magnetic Field

The magnetic field of a quadrupole wire system near the center of symmetry is well approximated by;

$$\bar{B}_1(\bar{r}) = -G(y + ix) \quad (a-1)$$

at the position  $\bar{r} = x + iy$ , where;

$$G = 0.8 \frac{I}{R_0^2} \text{ gauss/cm} \quad (a-2)$$

with, I = current in each wire in amperes,  $R_0$  = distance in centimeters from the center of symmetry to the center of each wire. The orientation of this field is shown in Fig. A-1. This field is similar to the field illustrated in Fig. 2-3, except that the orientation of the axes x,y with respect to the quadrupole wires is different.

If this system is twisted to form a helical quadrupole, as illustrated in Fig. 9-1, the field will rotate with z at twice the rate which the wires rotate with z, i.e., the field is represented in the axial region by a field of the form;

$$\bar{B}_1(\bar{r}, z) = -G_B(y + ix)e^{i2\omega z} \quad (a-3)$$

$$G_B = C(q)G \quad (a-4)$$

$$\omega = \frac{2\pi}{L} \quad (a-5)$$

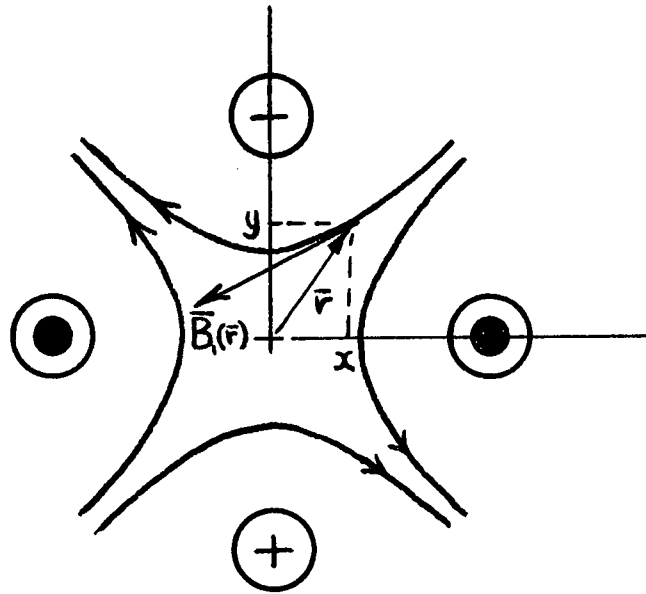


Figure A-1. Illustration of the orientation of the field  $\bar{B}_1(\bar{r}) = -G(y + ix)$  at the point  $\bar{r} = x + iy$ .

$$L = \text{helical step length} \quad (\text{a-6})$$

$$q = \frac{4\pi R_0}{L} \quad (\text{a-7})$$

The factor  $C(q)$  can be calculated from the paper of Le Couteur (1967), who solves for the general helical multipole case and the helical quadrupole in particular. He also considers the higher order terms  $O(r^3)$ , which are left out in the above relation.

We give;

$$C(q) = 1/2q^2 K_2(q) + 1/4q^3 K_1(q) \quad (\text{a-8})$$

where  $K_n$  is a modified Bessel function of the second kind.

In order to make the identification with Le Couteur we give the relation (Watson 1962, Eqn. 3, pg. 79)

$$zK'_V(z) = -vK_V(z) - zK_{V-1}(z) \quad (\text{a-9})$$

The factor  $C(q)$  is plotted in Fig. A-2.

Equation (a-3) may be written with a homogeneous solenoid field ( $B_0$ ) superimposed along the  $z$  axis.

$$\bar{B}(r, z) = B_x \hat{i} + B_y \hat{j} + B_z \hat{k} \quad (\text{a-10a})$$

$$B_x = G_B(x \sin 2\omega z - y \cos 2\omega z) \quad (\text{a-10b})$$

$$B_y = -G_B(y \sin 2\omega z + x \cos 2\omega z) \quad (\text{a-10c})$$

$$B_z = B_0 \quad (\text{a-10d})$$

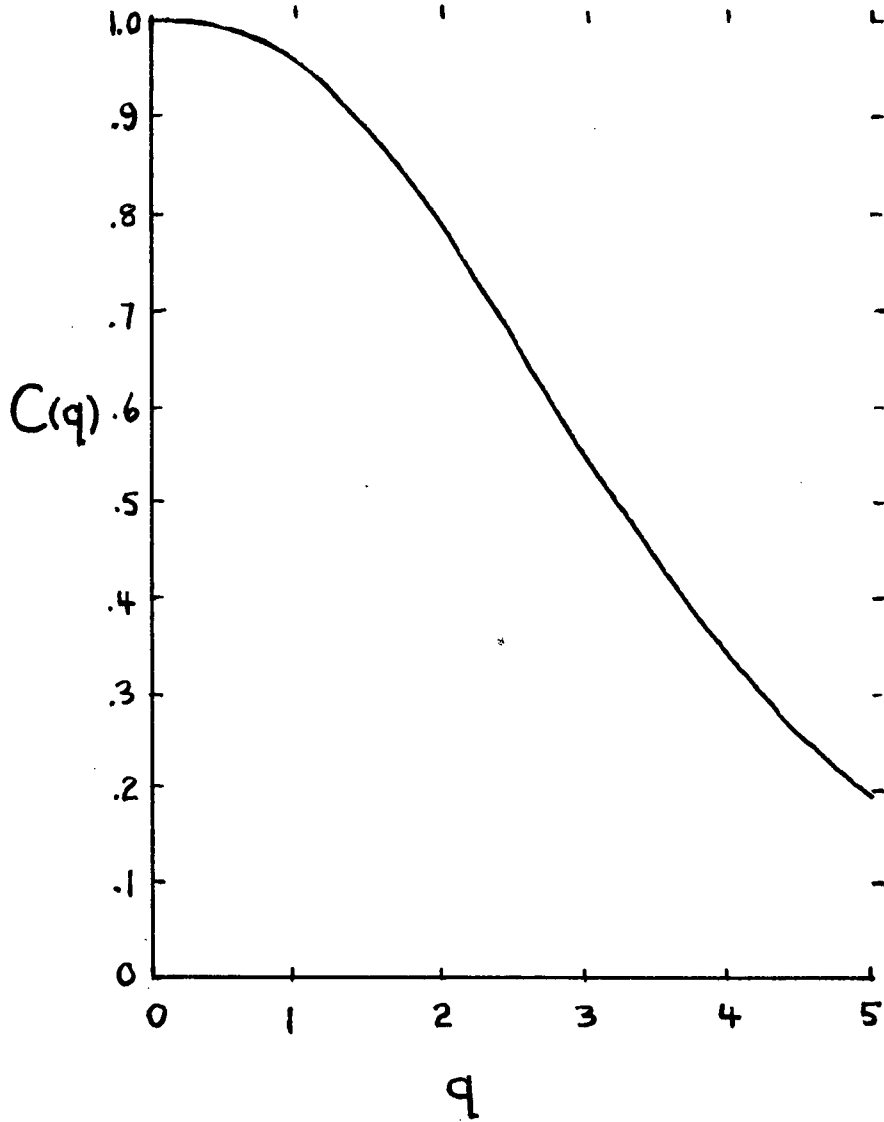


Figure A-2. Plot of the factor  $C(q)$  defined by equation (a-8).

APPENDIX B

The Derivation of the Trajectories of an Ion in a Helical Quadrupole Field Consisting of Orthogonal Electric and Magnetic Fields Superimposed on a Homogeneous Field and on which an Additional Radial Force is Introduced

From appendix A we have the magnetic field of a helical quadrupole;

$$\vec{B}(\vec{r}, z) = B_x \hat{i} + B_y \hat{j} + B_z \hat{k} \quad (\text{b-1a})$$

$$B_x = G_B (x \sin 2\omega z - y \cos 2\omega z) \quad (\text{b-1b})$$

$$B_y = -G_B (y \sin 2\omega z + x \cos 2\omega z) \quad (\text{b-1c})$$

$$B_z = B_0$$

where;

$$\omega = \frac{2\pi}{L}$$

L = helical step length

G<sub>B</sub> = magnetic gradient

The corresponding electric helical quadrupole field which is orthogonal to  $\vec{B}(\vec{r}, z)$  in the x,y plane can be found by putting;

$$\vec{E}(\vec{r}) \cdot \vec{B}(\vec{r}) = 0 \quad \text{with } B_z = 0 \quad (\text{b-2})$$

thus;

$$\vec{E}(\vec{r}) = E_x \hat{i} + E_y \hat{j} + E_z \hat{k} \quad (\text{b-3a})$$

$$E_x = G_E (y \sin 2\omega z + x \cos 2\omega z) \quad (\text{b-3b})$$

$$E_y = G_E (x \sin 2\omega z - y \cos 2\omega z) \quad (\text{b-3c})$$

$$E_z = 0 \quad (b-3d)$$

where;

$G_E$  = electric gradient

It is very useful to include in these solutions a radial force term  $\bar{F}_r$  which we define as;

$$\bar{F}_r = \phi \bar{r} \quad (b-4)$$

$\phi$  is a constant, and is left arbitrary in this derivation.

It is discussed in Chapter 8, where this additional force term is used.

The equation of motion which we wish to integrate is;

$$\frac{d^2 \bar{r}}{dt^2} = q/m(\bar{v} \times \bar{B}(\bar{r}) + \bar{E}(\bar{r})) + \frac{\bar{F}_r}{m} \quad (b-5)$$

This may be written as;

$$\frac{d^2 x}{dt^2} = q/m(E_x + v_y B_z - v_z B_y) + \frac{\phi}{m} x \quad (b-6a)$$

$$\frac{d^2 y}{dt^2} = q/m(E_y + v_z B_x - v_x B_z) + \frac{\phi}{m} y \quad (b-6b)$$

$$\frac{d^2 z}{dt^2} = q/m(v_x B_y - v_y B_x) \quad (b-6c)$$

We make the restrictions that;

$$\left| \frac{dz}{dt} \right| \gg \left| \frac{dx}{dt} \right|, \left| \frac{dy}{dt} \right| \quad (b-7a)$$

$$v_z = \frac{dz}{dt} = v_o \approx \text{constant} \quad (\text{b-7b})$$

then;

$$v_x = \frac{dx}{dt} = \frac{dx}{dz} \frac{dz}{dt} = v_o \dot{x} \quad (\text{b-8a})$$

$$v_y = \frac{dy}{dt} = v_o \dot{y} \quad (\text{b-8b})$$

where;

$$\dot{x} = \frac{dx}{dz} \quad (\text{b-8c})$$

$$\dot{y} = \frac{dy}{dz} \quad (\text{b-8d})$$

it follows that;

$$\frac{d^2x}{dt^2} = v_o^2 \ddot{x} \quad (\text{b-8e})$$

$$\frac{d^2y}{dt^2} = v_o^2 \ddot{y} \quad (\text{b-8f})$$

$$\frac{d^2z}{dt^2} \approx 0 \quad (\text{b-8g})$$

With these restrictions equation (b-6c) drops out. Substitution of equation (b-8) into (b-6) yields;

$$\ddot{x} = \frac{q}{mv_o^2} (E_x + v_y B_o - v_o B_y) + \frac{\Phi}{mv_o^2} x \quad (\text{b-9a})$$

$$\ddot{y} = \frac{q}{mv_o^2} (E_y + v_o B_x - v_x B_o) + \frac{\Phi}{mv_o^2} y \quad (\text{b-9b})$$

We wish to transform these equations to a set of axes ( $\underline{x}, \underline{y}$ ) which rotate at the rate  $\underline{\omega}z$ , i.e.,

$$\underline{x} = x \cos \underline{\omega}z + y \sin \underline{\omega}z \quad (\text{b-10a})$$

$$\underline{y} = y \cos \underline{\omega}z - x \sin \underline{\omega}z \quad (\text{b-10b})$$

differentiating with respect to  $z$ , we obtain;

$$\dot{\underline{x}} = \dot{x} \cos \underline{\omega}z + \dot{y} \sin \underline{\omega}z + \underline{\omega}y \quad (\text{b-11a})$$

$$\dot{\underline{y}} = \dot{y} \cos \underline{\omega}z - \dot{x} \sin \underline{\omega}z - \underline{\omega}x \quad (\text{b-11b})$$

and differentiating again;

$$\ddot{\underline{x}} - 2\underline{\omega}\dot{y} - \underline{\omega}^2 \underline{x} = \ddot{x} \cos \underline{\omega}z + \ddot{y} \sin \underline{\omega}z \quad (\text{b-12a})$$

$$\ddot{\underline{y}} + 2\underline{\omega}\dot{x} - \underline{\omega}^2 \underline{y} = \ddot{y} \cos \underline{\omega}z - \ddot{x} \sin \underline{\omega}z \quad (\text{b-12b})$$

Substituting for  $\ddot{x}$  and  $\ddot{y}$  from equation (b-9), equation (b-12) can be expressed after some manipulation in the following form;

$$\ddot{\underline{x}} - 2W\dot{y} - (W^2 + \Theta + f)\underline{x} = 0 \quad (\text{b-13a})$$

$$\ddot{\underline{y}} + 2W\dot{x} - (W^2 - \Theta + f)\underline{y} = 0 \quad (\text{b-13b})$$

where

$$W = \underline{\omega} + \frac{qB_0}{2mv_0} \quad (\text{b-14})$$

$$\Theta = \frac{q}{mv_0} \frac{1}{2} (G_E + v_0 G_B) \quad (\text{b-15})$$

$$f = \frac{\phi}{mv_o^2} - 1/4 \left( \frac{qB_o}{mv_o} \right)^2 \quad (b-16)$$

Equation (b-13) can be combined into a single fourth order, linear, homogeneous equation;

$$\ddot{\underline{x}} + 2(W^2 - f)\ddot{\underline{x}} + (W^2 + \Theta + f)(W^2 - \Theta + f)\underline{x} = 0 \quad (b-17)$$

Solutions of the form  $e^{Rz}$  are assumed. Four roots R are obtained;

$$R_1 = (-W^2 + f + \sqrt{\Theta^2 - 4W^2f})^{1/2} = (-W^2 + f + \delta)^{1/2} \quad (b-18a)$$

$$R_2 = (-W^2 + f - \delta)^{1/2} \quad (b-18b)$$

$$R_3 = -R_1 \quad (b-18c)$$

$$R_4 = -R_2 \quad (b-18d)$$

where;

$$\delta = \sqrt{\Theta^2 - 4W^2f} \quad (b-19)$$

The solutions can be written as;

$$\underline{x} = C_1 e^{R_1 z} + C_2 e^{R_2 z} + C_3 e^{-R_1 z} + C_4 e^{-R_2 z} \quad (b-20a)$$

$$\underline{y} = \frac{W^2 + \Theta + f - R_1^2}{-2WR_1} C_1 e^{R_1 z} + \frac{W^2 + \Theta + f - R_2^2}{-2WR_2} C_2 e^{R_2 z} \quad (b-20b)$$

$$- \frac{W^2 + \Theta + f - R_1^2}{-2WR_1} C_3 e^{-R_1 z} - \frac{W^2 + \Theta + f - R_2^2}{-2WR_2} C_4 e^{-R_2 z}$$

The constants, C, can be obtained in terms of the initial conditions. Denoting values at  $z = 0$  by subscript o, we obtain the following from equations (b-10) and (b-11);

$$\begin{aligned} \underline{x}_o &= x_o \\ \underline{y}_o &= y_o \\ \dot{\underline{x}}_o &= \dot{x}_o + \omega y_o \\ \dot{\underline{y}}_o &= \dot{y}_o - \omega x_o \end{aligned} \tag{b-21}$$

The equations (b-20), together with their first derivatives, evaluated at  $z = 0$  using the values from equations (b-21), give four equations which can be solved for the four unknown C's. For the case where the four roots are all pure imaginary so that they may be written in the form  $R = iR'$ , where the prime denotes a real number, then the solutions to equation (b-17) can be written as follows, where the constants have been solved for in terms of the initial conditions given by equation (b-21).

$$\begin{aligned} \underline{x} &= \frac{x_o}{2} [(\cos R_1' z + \cos R_2' z) + \frac{2W^2 - 2\omega W + \Theta}{\delta} (\cos R_1' z - \cos R_2' z)] + \frac{y_o}{2} [\omega (\frac{\sin R_1' z}{R_1'} \\ &+ \frac{\sin R_2' z}{R_2'}) + (\frac{2W(\omega W - W^2 + \Theta - f) - \omega \Theta}{\delta} (\frac{\sin R_2' z}{R_2'} - \frac{\sin R_1' z}{R_1'}))] + \frac{\dot{x}_o}{2} [\frac{\sin R_1' z}{R_1'} \\ &+ \frac{\sin R_2' z}{R_2'} + \frac{2W^2 - \Theta}{\delta} (\frac{\sin R_2' z}{R_2'} - \frac{\sin R_1' z}{R_1'})] + \frac{\dot{y}_o W}{\delta} [\cos R_1' z - \cos R_2' z] \end{aligned} \tag{b-22a}$$

$$\begin{aligned}
 \underline{y} = & -\frac{x_0}{2} \left[ \omega \left( \frac{\sin R_1' z}{R_1'} + \frac{\sin R_2' z}{R_2'} \right) + \left( \frac{2W(\omega W - W^2 - \Theta - f) + \omega \Theta}{\delta} \right) \left( \frac{\sin R_2' z}{R_2'} - \frac{\sin R_1' z}{R_1'} \right) \right] \\
 & + \frac{y_0}{2} \left[ \cos R_1' z + \cos R_2' z + \frac{2W^2 - 2\omega W - \Theta}{\delta} (\cos R_1' z - \cos R_2' z) \right] \\
 & - \dot{x}_0 \frac{W}{\delta} [\cos R_1' z - \cos R_2' z] \\
 & + \frac{\dot{y}_0}{2} \left[ \frac{\sin R_1' z}{R_1'} + \frac{\sin R_2' z}{R_2'} + \frac{2W^2 + \Theta}{\delta} \left( \frac{\sin R_2' z}{R_2'} - \frac{\sin R_1' z}{R_1'} \right) \right]
 \end{aligned}$$

(b-22b)

APPENDIX C

An Ion Gun Design Suitable for Producing Small Diameter, Well-Collimated,  
Ion Beams

The ion gun described in this appendix was developed specifically to produce small diameter, well-collimated ion beams using an electron bombardment ion source. The major innovation from standard designs such as given by Novick and Commins (1958) or Plumlee (1957) is the incorporation of the ring focus electron gun, which is well suited to ionizing small diameter beams because of its geometry. A diagram of the ion gun is given in Fig. C-1.

The ring focus electron gun has been used by others for various purposes but it has not, to our knowledge, been incorporated into an ion gun suitable for adaption to this experiment. Bas and Gauz (1968) have analyzed its design in some detail. Zankel (1968) has calculated electrode shapes to maintain a coaxial current flow by compensating for end effects, although our design does not include this compensation. The advantages of the ring focus design are threefold. It is a very compact, simple structure, with a cylindrical geometry which matches the beam geometry and reduces the various field asymmetries to a minimum. It utilizes an electrostatic focusing system which is self-focusing at all bombardment energies. Electrostatic focusing in the electron gun has the advantage that it does not affect the ion beam as would a magnetic focusing system. Finally, the ring focus design produces a very intense electron beam in the axial region where the ionizing events are most useful.

The major problem with the ring focus design is the magnetic field produced by the filament heater current which deflects the electrons so that they do not enter the axial region where the ionization is to occur. For our purpose this problem was overcome by using "on-off" heater current with a filament having a large thermal mass. The useful beam is produced during the "off" period, which may be a large fraction of each cycle. The detector may be gated in synchronism with the heater current to increase the signal to noise. This "on-off" cycle has the additional advantage that the magnetic field from the filament current lead-in wires does not affect the ion beam, so that these wires may be placed conveniently to simplify construction.

The lens system consists of a Pierce lens (Pierce 1954) to initially collect and focus the ions, three single aperture lens, and a three element unipotential lens (Lippert and Pohlit, 1952 and 1953), followed by a collimating aperture.

The Pierce lens was chosen because its focal length and aberration constants may be closely calculated. The Pierce lens, together with the unipotential lens, may be designed to correct to first order for chromatic aberration, and partly correct for spherical aberration. They may also be designed as a crude monochromator by making the system very chromatic.

Referring to Fig. C-1 for an explanation of the symbols, we give the following design formulae;

The ion gun will focus the beam at infinity if;

$$\frac{V}{V'} = -\frac{A}{2} \pm \sqrt{\frac{A^2}{4} - B} \quad (c-1)$$

where;

$$A = - \frac{[5(g-i_1) + 3b' + 4h]}{4[h + b' + g - i_1]} \quad (c-2)$$

$$B = - \frac{b'[5(g-i_1) + 4h]}{16h[h + b + g - i_1]} \quad (c-3)$$

$$i_1 = \frac{4d'l'}{3l'-d'} \quad (c-4)$$

The variation of the focal point ( $z_f$ ) of the unipotential lens as a function of the spread in beam energy ( $\Delta U_o$ ) is given by; (Hanszen and Lauer 1967)

$$\Delta z_f = -C_{ch}^{(\infty)} \frac{\Delta U_o}{V} \quad (c-5)$$

where  $C_{ch}^{(\infty)}$  is the chromatic aberration constant of the unipotential lens.

For achromatic operation of the ion gun we put;

$$\Delta z_f = -\Delta i_3 \quad (c-6)$$

where  $\Delta i_3$  is the variation in the image point of the lens preceding the unipotential lens as a function of the spread in beam energy. We give the formula;

$$\Delta i_3 = (b')^2 \frac{\Delta U_o}{V} \left[ \frac{i_2^2}{(h-i_2)^2} \left( \frac{i_1^2}{(1+S)f_1(g-i_1)^2} + \frac{1}{(1+S)f_2} \right) + \frac{1}{f_3} \right] \quad (c-7)$$

where;

$$f_1 = \frac{-4d'l'}{d'+l'} \quad (c-8)$$

$$f_2 = 4h \frac{(V-V')}{V'} \quad (c-9)$$

$$f_3 = - \frac{4h}{S} \quad (c-10)$$

$$S = - \frac{V'}{V} \quad (c-11)$$

$$i_2 = \frac{f_2(g-i_1)}{g-i_1-f_2} \quad (c-12)$$

The minimum chromatic aberration constant for a unipotential lens is;

$$C_{ch}^{(\infty)} = -3 \ell \quad (c-13)$$

The condition for achromatic operation, equation (c-6), and equation (c-7), yield for this particular case the unipotential lens length ( $\ell$ );

$$\ell = - \frac{(b')^2}{3} \left[ \frac{i_2^2}{(h-i_2)^2} \left( \frac{i_1^2}{(1+S)f_1(g-i_1)^2} + \frac{1}{(1+S)f_2} \right) + \frac{1}{f_3} \right] \quad (c-14)$$

In the normal operating range ( $S > 0$ ) we have  $f_2, f_3 < 0$ , while  $f_1 < 0$  for all  $S$ . Such values yield  $\ell > 0$  which indicates that achromatic operation is possible in the normal operating range if the gun dimensions are chosen to give a reasonable value of " $\ell$ ".

The ion gun which we have built has the following nominal dimensions, in inches,

$$\ell' = 0.20$$

$$d' = 0.25$$

$$g \approx 0.075$$

$$h \approx 0.160$$

$$b' = .158$$

$$d_o = .020$$

$$z_c = 1.7$$

The unipotential lens has the nominal dimensions;

$$a = 0.176$$

$$b = 0.176$$

$$d = 0.088$$

$$\ell = 0.44$$

for which;

$$z_f = 0.145$$

$$\frac{C_{ch}^{(\infty)}}{\ell} = -3$$

From equation (c-1), this ion gun should focus at infinity for;

$$V' \approx -3V$$

$$\text{or } V' \approx (1/2)V$$

In practice, it is very difficult to build the ion gun accurately enough to expect precise agreement between experiment and theory. For our gun we obtained the best results by operating the unipotential lens

somewhat below  $(V)$ , with  $V' \approx -2V$ .

Note that the condition  $V' = (1/2)V$  is an unfavourable one because the positive ions experience only a very weakly accelerating electric field on exit from the ionizer.

Fig. C-2 gives typical results for a  $\text{He}^+$  beam with a pressure in the ionizer of approximately  $5 \times 10^{-4}$  Torr (He). These results were obtained by directing the beam through a field-free region 50 cm long between the ion gun exit aperture and four knife-edge jaws which could be independently moved to explore the beam intensity. The ions were collected by an electron multiplier (Bendix, model 306). The pressure in the field free region was  $5 \times 10^{-7}$  Torr.

The ion gun was constructed of Type 304 stainless steel with alumina insulators.

### Electrodes: (potential)

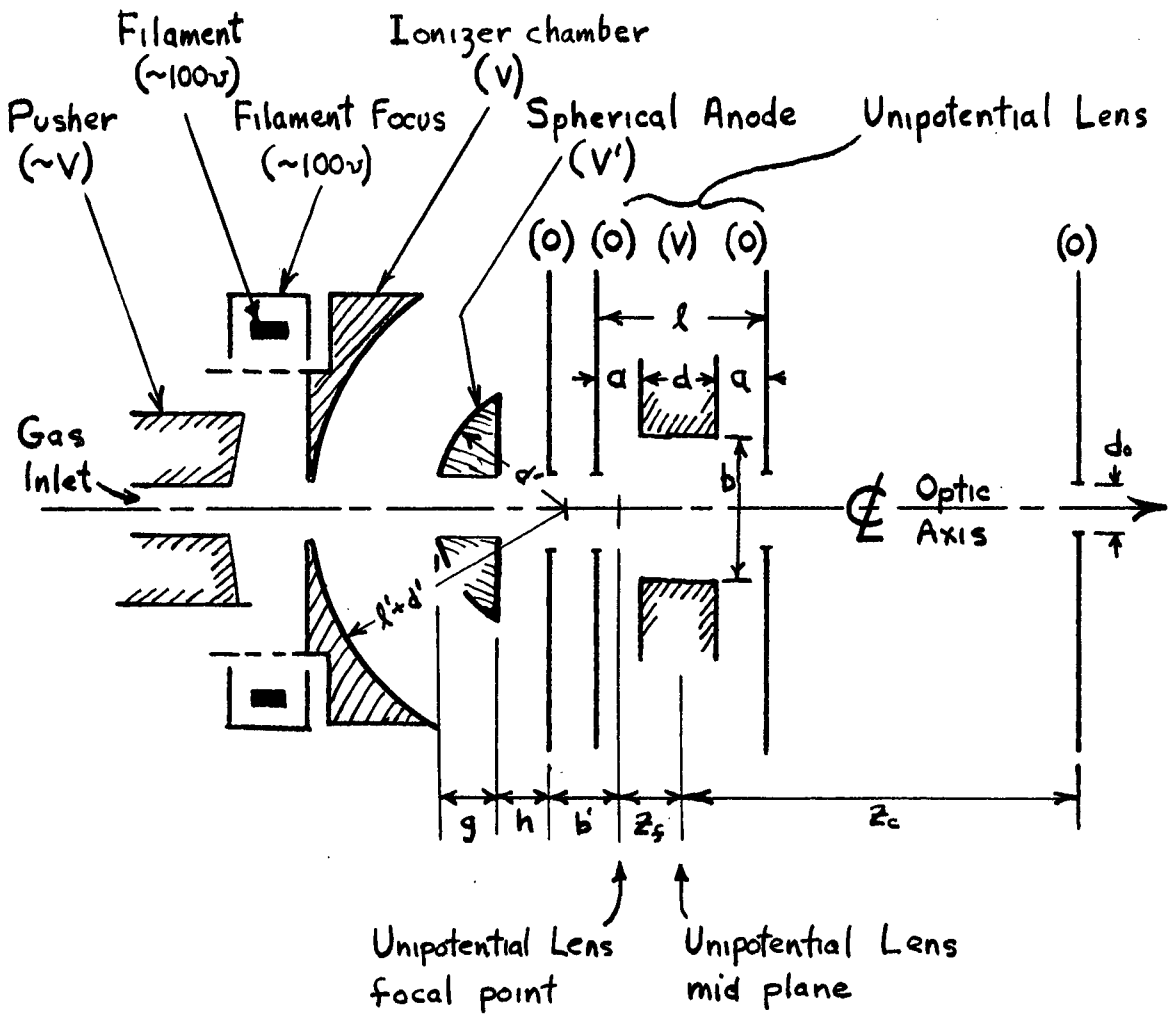


Figure C-1. Diagram of the ion gun described in appendix C.

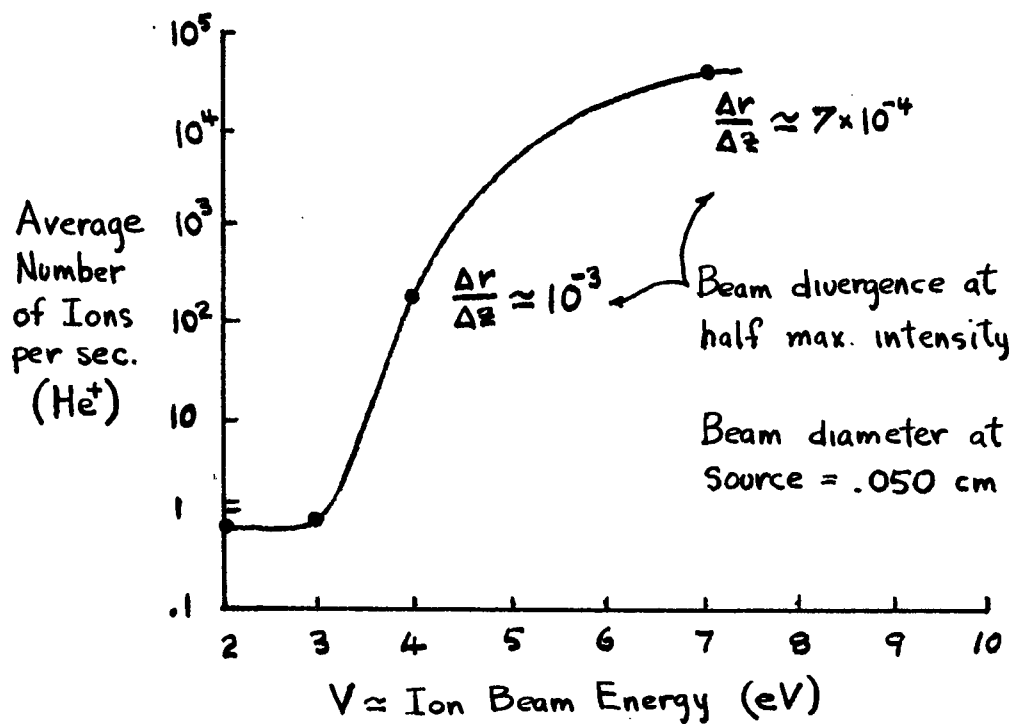


Figure C-2. Typical performance of the ion gun described in appendix C.  $V$  is the potential of the ionizing chamber.